Fluctuation Induced Cross-Field Transport in Hall Thrusters and Tokamaks

by

Michael Lane Garrett
B.A., Physics, Wesleyan University (1997)
S.M., Applied Plasma Physics, M.I.T. (2012)

Submitted to the Department of Aeronautics and Astronautics
in partial fulfillment of the requirements for the degree of
Master of Science in Aeronautics and Astronautics
at the
MASSACHUSETTS INSTITUTE OF TECHNOLOGY
September 2013

Author .....
Department of Aeronautics and Astronautics
August 22, 2013

Certified by .....
Manuel Martinez-Sanchez
Professor
Thesis Supervisor

Certified by .....
Stephen J. Wukitch
Research Scientist
Thesis Reader

Certified by .....
Felix I. Parra
Assistant Professor
Thesis Reader

Accepted by .....
Eytan H. Modiano
Professor of Aeronautics and Astronautics
Chair, Graduate Program Committee

Fluctuation Induced Cross-Field Transport in Hall Thrusters and Tokamaks

by

Michael Lane Garrett

Submitted to the Department of Aeronautics and Astronautics
on August 22, 2013, in partial fulfillment of the
requirements for the degree of
Master of Science in Aeronautics and Astronautics

Abstract

One area of fundamental plasma physics which remains poorly understood is the transport of particles across magnetic field lines at rates significantly higher than predicted by theory exclusively based on collisions. This "anomalous" transport is observed in many different classes of plasma experiment. Notably, both magnetic confinement fusion devices and Hall thrusters exhibit anomalous cross-field particle diffusion. This higher than predicted "loss" of particles has significant practical implications for both classes of experiment.

In the case of magnetic confinement fusion experiments, such as tokamaks, the Lawson criterion $nT\tau_{\mathrm{E}} \geq 10^{21}$ [keV$\cdot$ s$\cdot$ m^{-3}] dictates that the reactant particles in a fusion plasma must be confined for a sufficient time to fuse. Higher than predicted cross-field transport decreases the effectiveness of the magnetic confinement and makes fusion more difficult to achieve. For Hall thrusters, enhanced cross-field electron mobility reduces the efficiency of the thruster. As a result, more propellant and power is required to achieve the same thrust.

The goal of this thesis is to review observed and predicted fluctuation induced particle transport in Hall thrusters and tokamaks. To date, significant work has been done within both the tokamak and propulsion communities to attempt to quantify the effect of turbulent fluctuations of plasma parameters on anomalous cross-field transport. However, our understanding of the fundamental physical processes that lead to anomalously high cross-field transport remains incomplete.

These two regimes of plasma physics are very different in several important ways. The magnetic field strength and field orientation, the device size, the collisionality of different species, the ion mass, and the presence of neutrals are all areas with significant differences between tokamaks and Hall thrusters. However, there are similarities as well. For example, the edge density and temperature in a tokamak are similar to those found in Hall thrusters, both have magnetized electrons, drift waves occur in both regimes and many of the observed fluctuations are of similar scale.

Generally, research on cross-field transport within the tokamak community is isolated from work done within the thruster community. However, analysis of physics

within both regimes reveals a rich set of complex fluctuations across a broad frequency spectrum, which contribute to cross-field transport. By studying the relevant phenomena in tandem, we can reveal fundamental processes present in both regimes. Hopefully, this will lead to a global explanation for these elusive physical processes.

Thesis Supervisor: Manuel Martinez-Sanchez
Title: Professor

Thesis Reader: Stephen J. Wukitch
Title: Research Scientist

Thesis Reader: Felix I. Parra
Title: Assistant Professor

– For Natalie –

Contents

List of Figures

List of Tables

Chapter 1

Introduction

1.1 Plasma

Known colloquially as the "4$^{\text{th}}$ state of matter", the plasma state is more energetic than those of solids, liquids, or gases. Plasma is also everywhere; comprising approximately 99% of the visible universe, plasma is quite abundant. The stars, interstellar medium, lightning, auroras, and florescent lights are all examples of plasmas. Plasma is integral to processing semiconductors for the multi-billion dollar electronics industry. It is the requisite state for both nuclear fusion and high efficiency rockets. As a result, the physics of plasmas has great importance for both academic and practical reasons.

One area of fundamental plasma physics which remains poorly understood is the transport of particles across magnetic field lines at rates significantly higher than predicted by theory based on collisions. This "anomalous" transport is observed in many different classes of plasma experiment. Notably, both magnetic confinement fusion devices and Hall thrusters exhibit anomalous cross-field particle diffusion. This, higher than predicted, "loss" of particles has significant practical implications for both of these types of experiment.

In the case of magnetic confinement fusion experiments, such as tokamaks, the Lawson criterion $nT\tau_{\text{E}} \geq 10^{21}$ [keV$\cdot$ s$\cdot$ m^{-3}] dictates that the reactant ions in a fusion plasma must be confined for a sufficient time to fuse. Higher than predicted cross-field

transport decreases the effectiveness of the magnetic confinement and makes fusion more difficult to achieve. For Hall thrusters, enhanced cross-field electron mobility reduces the efficiency of the thruster. As a result, more propellant is required to achieve the same thrust.

The goal of this thesis is to review observed and predicted fluctuation induced particle, momentum and energy transport in Hall thrusters and tokamaks. To date, significant work has been done within both the tokamak and propulsion communities to attempt to quantify the effect of turbulent fluctuations of plasma parameters on anomalous cross-field transport. However, our understanding of the fundamental physical processes that lead to anomalously high cross-field transport remains incomplete.

These two regimes of plasma physics are very different in several important ways. The magnetic field strength and field orientation, the device size, the collisionality of different species, the ion mass, and the presence of neutrals are all areas with significant differences between tokamaks and Hall thrusters. However, there are similarities as well. For example, the edge density and temperature in a tokamak are similar to those found in Hall thrusters, both have magnetized electrons, drift waves occur in both regimes and many of the observed fluctuations are of similar scale.

Generally, research on cross-field transport within the tokamak community is isolated from work done within the thruster community. However, analysis of physics within both regimes reveals a rich set of complex fluctuations across a broad frequency spectrum, which contribute to cross-field transport. By studying the relevant phenomena in tandem, we can reveal fundamental processes present in both regimes. Hopefully, this will lead to a global explanation for these elusive physical processes. To begin, an overview of the nature of tokamak and Hall thruster plasmas is required.

1.1.1 Fusion energy

Nuclear fusion reactions occur when light nuclides fuse to form heavier nuclides. As a direct result of the strong nuclear force, nuclides lighter than iron (see Fig. 1-1), have masses larger than their fusion product. This mass deficit Δm, is the source of

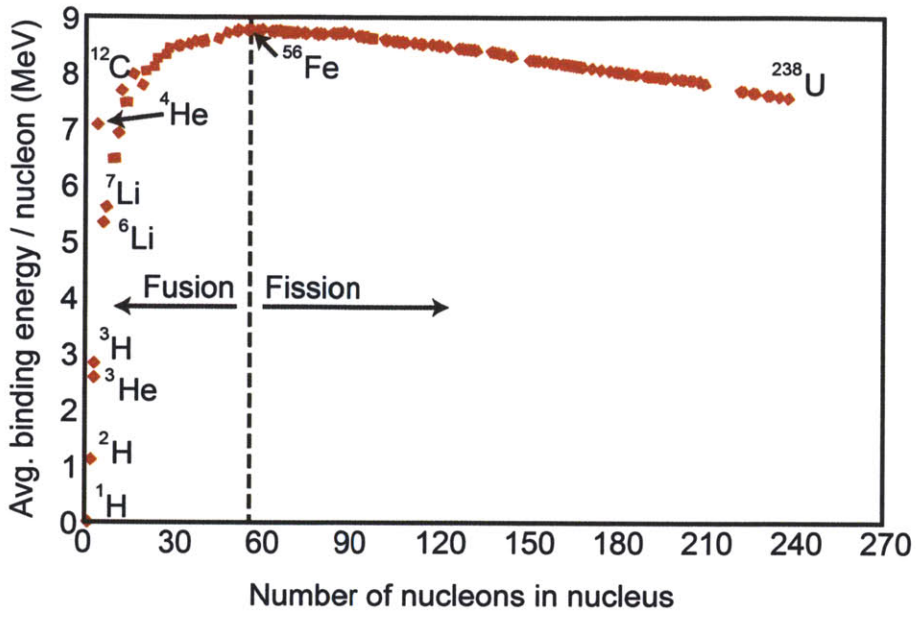

Figure 1-1: Nuclear binding energy.

fusion energy. Relativity theory describes the amount of energy released from each fusion reaction as Δmc^2, where c is the speed of light. More specifically, this *binding energy* is given by:

$$E_B = (Nm_{\mathrm{n}} + Zm_{\mathrm{p}} - m_{\mathrm{A}})\, c^2 \tag{1.1}$$

where Nm_{n} is the total mass of the neutrons, Zm_{p} is the total mass of the protons, and m_{A} is the mass of the resulting nuclear product.

The six nuclear reactions of primary interest for fusion reactors are:

- $D + D \rightarrow T(1.01MeV) + p(3.03MeV)$
- $D + D \rightarrow He^3(0.82MeV) + n(2.45MeV)$
- $D + T \rightarrow He^4(3.52MeV) + n(14.06MeV)$
- $D + He^3 \rightarrow He^4(3.67MeV) + p(14.67MeV)$
- $Li^6 + n \rightarrow T + He^4 + (4.8MeV)$
- $Li^7 + n \rightarrow T + He^4 + n - (2.5MeV)$

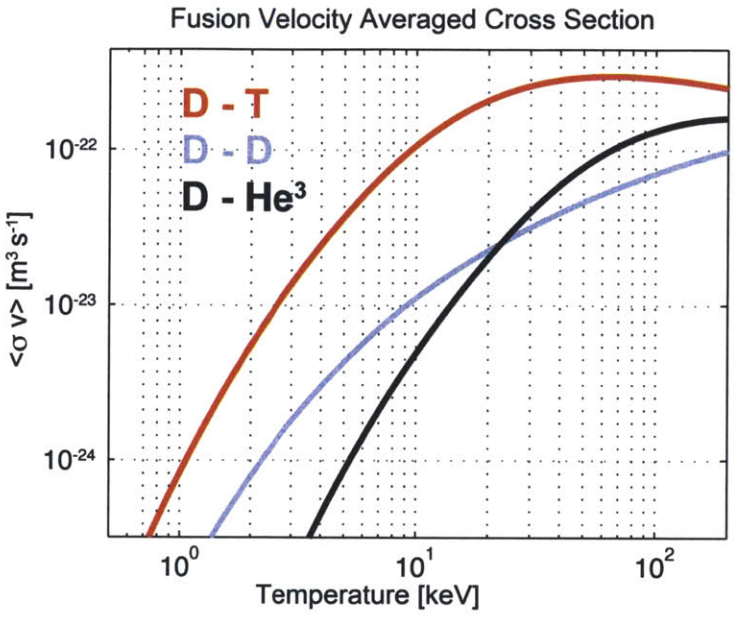

Figure 1-2: Velocity averaged cross section $\langle \sigma v \rangle$ for D-T, D-D, and D-He^3 reactions as a function of temperature.

where D is deuterium, T is tritium, He^3 is helium, and Li is lithium.

Most experiments today, including Alcator C-Mod, use deuterium plasmas. Deuterium-deuterium reactions produce two branches of products as seen above; either a triton and a proton are produced, or a helium-3 nucleus and a neutron. Note that both of these reactions release a moderate amount of energy ($\sim 4MeV$) compared with the D-T or D-He^3 reactions ($\sim 18MeV$). For the D-T reaction, 17.6 MeV are transferred into the kinetic energy of the reaction products from the nuclear strong force. As can be seen from Fig. 1-2, the reaction rate $\langle \sigma v \rangle$ for D-T is almost two orders of magnitude larger than both D-D and D-He^3, below 30 keV. As a result, for a given nuclear reaction rate, D-T reactions occur at a lower temperature than do D-D or D-He^3 reactions. This is an important consideration because the required temperatures for thermonuclear fusion are very high $\sim$ 10 keV, or about 120 million degrees Celsius. This is due to an electrostatic barrier, called the Coulomb potential barrier, surrounding each nucleus, which arises from the electrostatic charge of the protons contained therein. This mutual electrostatic repulsion of similarly charged nuclei must be overcome in order to bring the two nuclei close enough for the fusion reaction to

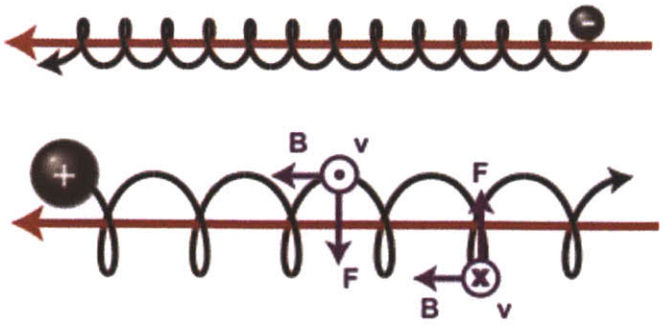

Figure 1-3: Gyro motion of charged particles in a magnetic field.

occur. This can be achieved by heating a plasma of deuterium and tritium to the requisite temperatures, thus using the thermal velocity of the particles to overcome the Coulomb barrier and initiate the fusion reaction. The volumetric reaction rate for these fusion events is given by: [36]

$$R_{ij} = n_i n_j \langle \sigma v \rangle, \tag{1.2}$$

where the velocity averaged cross section $\langle \sigma v \rangle$ is shown in Fig. 1-2, and n_i and n_j represent the particle number densities of two ion species. As its name suggests, magnetic confinement utilizes magnetic fields to confine the plasma and keep it away from the walls of the device, which are much colder than the plasma itself. This confinement allows the plasma to be heated sufficiently to achieve the temperatures and pressures required for fusion.

As the temperature of matter (and hence mean energy of individual constituent particles) increases, it transitions through states of solid, liquid and gas. As it becomes even hotter, the atoms of the material ionize, thereby dissociating the negatively charged electrons from the positively charged protons in the nucleus. When this happens to a sufficient number of atoms in a given population, the resulting *ions* begin to exhibit collective behavior as a result of the Lorentz forces they create as they move. This *ionized* collection of particles is called a plasma. Because most of the particles in a plasma have a net electric charge, fusion scientists can exploit

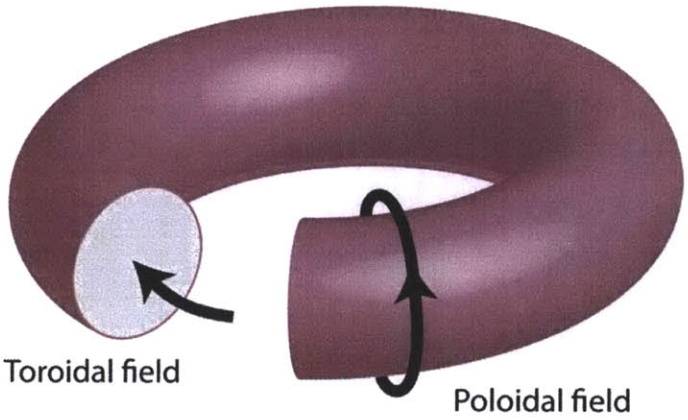

Figure 1-4: Toroidal and poloidal magnetic fields required to realize rotational transform in a tokamak.

an attribute of their motion given by the Lorentz force: $\mathbf{F} = q(\mathbf{E} + \mathbf{v} \times \mathbf{B})$. The $\mathbf{v} \times \mathbf{B}$ component of this force causes charged particles to orbit magnetic field lines as they travel along them, as shown schematically in Fig. 1-3. This gyro motion causes charged particles to trace helical trajectories along magnetic field lines. If these field lines do not intersect the walls that contain the plasma and are made to *close* on themselves, then the particles can be confined by this magnetic field.

1.1.2 Tokamaks

The choice of magnetic topology used to confine a plasma is not an obvious one. As mentioned in Sec. 1.1.1, charged particles are forced to move along magnetic field lines. Initial fusion experiments utilized cylindrical plasmas with axial magnetic fields. To prevent the particles from streaming out the ends of the device, separate magnets were used to create magnetic mirror fields at the ends. However, significant particle and energy losses can still occur along the field lines in the magnetic mirror geometry. As a result, mirror devices have typically had poor performance. The end losses, combined with poor plasma stability, limit the achievable plasma temperature and confinement time.

In the 1950s a group of Russian scientists invented a new type of magnetic confinement device called a tokamak. The word tokamak comes from the Russian acronym,

Figure 1-5: Reconstruction of the total magnetic field in Alcator C-Mod for shot 1050426022, t = .64 s. Color indicates field magnitude: Max (red) 7.8 T, Min (blue) 3.2 T.

TOKAMAK (**ТО**роидалыная **КА**мера с **МА**гнитными **К**атушками), which means toroidal chamber with magnetic coils. Here, the Russians discovered a magnetic topology, which can have a set of surfaces where there exists a non-vanishing continuous tangent vector field. In other words, the magnetic field lines on the surface of a torus can be made to wrap around continuously. In 1968, at the Kurchatov Institute in Moscow, Russian scientists achieved a record plasma temperature of ~ 1 keV, an order of magnitude higher than any of the western devices had reached at the time [37]. Today, all magnetic fusion devices are structured around a general toroidal geometry to prevent end-losses. However, as we will see in the next chapter, even in optimized experiments, particles diffuse across the magnetic field. In addition, the diffusion occurs at a rate much faster than theory based on collisionality predicts.

The torus is the desired topology; however, if a cylinder with an axial magnetic field, called a θ-pinch, is simply bent into a torus, it turns out to be unstable. As a result, a poloidal magnetic field must be combined with the toroidal field from the θ-pinch, as shown in Fig. 1-4, to form a helical magnetic field configuration known as a screw-pinch (see Fig. 1-5).

The toroidal magnetic field has a 1/R dependence and decreases from the center of the tokamak to the outside. The toroidal field also has a curvature associated with it, because it is in the shape of a torus. When a gradient exists within the magnetic field in a plasma, a so-called grad-B (∇B) drift of the electrons and ions occurs:

$$v_{\nabla B} = -\frac{mv_{\perp}^2}{2q}\frac{\nabla B \times \mathbf{B}}{B^3}, \tag{1.3}$$

which causes the ions and electrons to drift in opposite directions resulting in charge separation. When a magnetic field is present in the plasma with some finite curvature, another drift, the curvature drift occurs:

$$v_K = \frac{mv_{\parallel}^2}{qR_c}\frac{\mathbf{R}_c \times \mathbf{B}}{B^2}, \tag{1.4}$$

which also results in charge separation. These two properties, the magnetic field gradient and the magnetic field curvature, cause particles in a tokamak to drift vertically in opposite directions for different charge polarity. If the field is purely toroidal, this charge separation produces a vertical electric field, resulting in an additional drift ($\mathbf{E} \times \mathbf{B}$) of the plasma radially towards the low-field side (note that this drift is independent of charge): [36]

$$v_{\mathbf{E}\times\mathbf{B}} = \frac{\mathbf{E} \times \mathbf{B}}{B^2}. \tag{1.5}$$

To ameliorate this effect, a poloidal magnetic field is required.

The velocity of a particle in a non-uniform magnetic field changes as it moves. As the particle moves toward a higher field, its parallel velocity decreases, while its perpendicular velocity increases. In a tokamak, this *mirror* effect causes particles with low initial parallel velocities to reflect and become trapped in low-field orbits, which are shaped like bananas. If a particle has a sufficiently large parallel velocity, it avoids becoming trapped in a so-called *banana orbit* and passes through the high-field side of the tokamak, orbiting around the entire torus. These orbits are shown in Fig. 1-6.

All axisymmetric toroidal fusion devices have both poloidal and toroidal magnetic

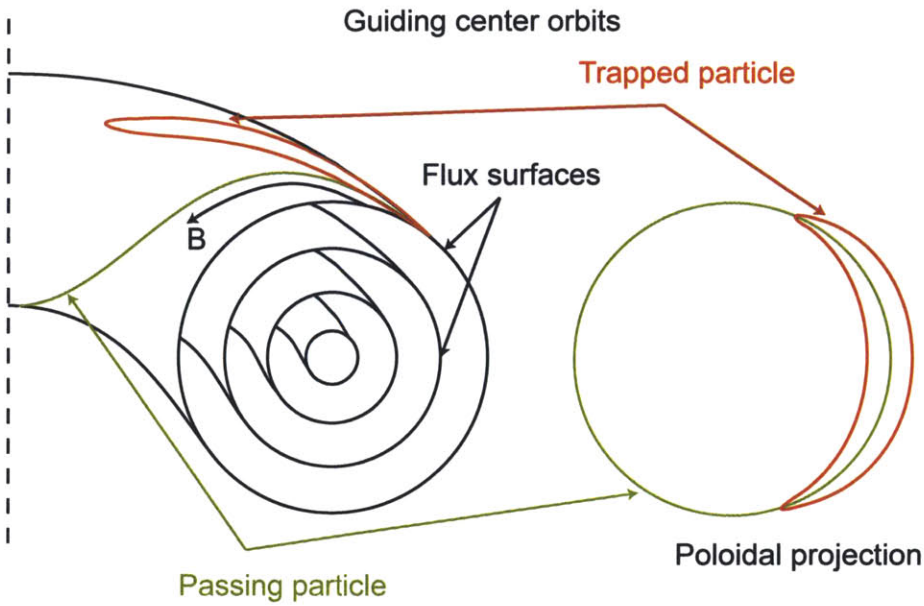

Figure 1-6: Circular cross-section tokamak flux surfaces. Passing particles transit from low-field side to high-field side, circulating around the torus. The trapped particles, lacking sufficient initial $v_{\|}$, are reflected and trace out banana-shaped orbits.

fields. On a tokamak, large toroidal field coils, which wrap around the torus in the poloidal direction, provide the toroidal magnetic field. Current running through the plasma itself must generate the poloidal field. The Spitzer plasma resistivity for a deuterium plasma is given by:

$$\eta \approx 5.2 \times 10^{-5} \frac{Z_{\text{eff}} \ln \Lambda}{T_e^{3/2}} \quad [\Omega\text{m}], \tag{1.6}$$

where T_e is the electron temperature in eV, Z_{eff} is the effective atomic number, and Λ is given by:

$$\Lambda = \frac{4}{3}\pi \left(\frac{\varepsilon_0 T_e}{e^2 n_0} \right)^{3/2} n_0. \tag{1.7}$$

Thus, the resistivity of the plasma is extremely small at fusion temperatures $\eta \sim 1 \times 10^{-9} \Omega\text{m}$. As a result, this current can be driven inductively by a large solenoid positioned in the center of the torus. Here, the plasma functions as the secondary winding of a transformer; the central solenoid functions as the primary winding. However, the central solenoid current ramp is limited to a finite amount of time.

Therefore, a fusion power plant, which must operate in steady-state, needs to drive current in the plasma through some non-inductive method. Several non-inductive current drive methods have produced promising experimental results. For a reactor, the most efficient method is likely to be coupling an asymmetric toroidal spectrum of radio frequency (RF) waves to the plasma. On Alcator C-Mod, this is accomplished using lower hybrid (LH) waves, which lose their energy to high-energy electrons in the plasma, through a process called Landau damping. However, many physics and engineering challenges must be solved for lower hybrid current drive (LHCD) before it can be successfully implemented on a reactor.

As mentioned above, a poloidal magnetic field is critical to confining a plasma in a toroidal fusion device. This is because the field lines must produce an adequate rotational transform around the torus. Rotational transform is defined as the number of poloidal transits to toroidal transits of a field line:

$$\frac{\iota}{2\pi} = \frac{d\psi}{d\Phi}, \tag{1.8}$$

where ψ is the poloidal magnetic flux and Φ is the toroidal magnetic flux. However, there is an alternative to driving a current in the plasma itself to accomplish rotational transform of the field lines. Instead, the toroidal magnetic field coils can be deformed to provide both a toroidal and poloidal magnetic field. This alternative approach is used in a class of fusion devices called stellarators. In stellarators, the current drive problem is solved. However, the resulting plasma and magnetic configuration is no longer truly axisymmetric and is extraordinarily complex.

In both the tokamak and the stellarator, plasma equilibrium and stability require complicated coil configurations and real-time control of plasma shaping. Magnetohydrodynamics (MHD), a single fluid model combining electromagnetism and fluid dynamics, is used to characterize the fundamental plasma equilibrium and stability. Magnetohydrodynamics theory has been instrumental in quantifying operational regimes useful for a fusion reactor.

The tokamak, in particular, has produced promising results in machines all over

the world. Today, a next-step fusion reactor is being constructed in Cadarache, France. The International Thermonuclear Experimental Reactor (ITER) is scheduled to have first plasma in 2021. ITER is designed to achieve a net energy gain with a physics gain factor $Q = 10$. The physics gain factor is given by:

$$Q = \frac{\frac{1}{4} n_e^2 \langle \sigma v \rangle E_\mathrm{f} \cdot V_\mathrm{p}}{P_\mathrm{h}}, \tag{1.9}$$

where the rate coefficient $\langle \sigma v \rangle$ is shown in Fig. 1-2, E_f is the fusion energy per reaction, V_p is the plasma volume, and P_h is the external heating power. Here, $Q = 1$ is the break-even operation point, $Q > 5$ is defined as a burning plasma, and $Q = \infty$ is ignition. From this definition, ITER is expected to produce a burning plasma, in which heating from the α-particles inside the plasma is double the external heating power applied to the reactor. ITER should extend our understanding of fusion plasmas into the burning plasma regime and contribute to the next large step toward actualizing commercially available fusion power, a demonstration fusion power plant (DEMO).

1.1.2.1 *ALto CAmpo TORus*

To develop the requisite physics basis and engineering capability to build ITER, the fusion community has developed a series of tokamak experiments all over the world. One of the most significant tokamaks, in terms of establishing a physics basis for ITER, is Alcator C-Mod. Alcator C-Mod is one of three National Tokamak Facilities in the United States. The characteristics of Alcator C-Mod are described in detail elsewhere [38]. Although it is a relatively small machine, (major radius, $R_0 = 0.67$ m, minor radius, $a = 0.22$ m) Alcator C-Mod is uniquely equipped to study ITER and reactor-relevant auxiliary heating methods, such as ion cyclotron range of frequencies (ICRF) and lower hybrid (LH) heating. It operates at high densities (up to $10^{21}\mathrm{m}^{-3}$) and has the highest toroidal magnetic field (up to 8 T) of any divertor tokamak. The C-Mod ICRF antennas operate at power densities of up to 10 MW/m^2, $\sim$ 50 % higher than expected ITER ICRF power densities [39]. ITER is also expected to

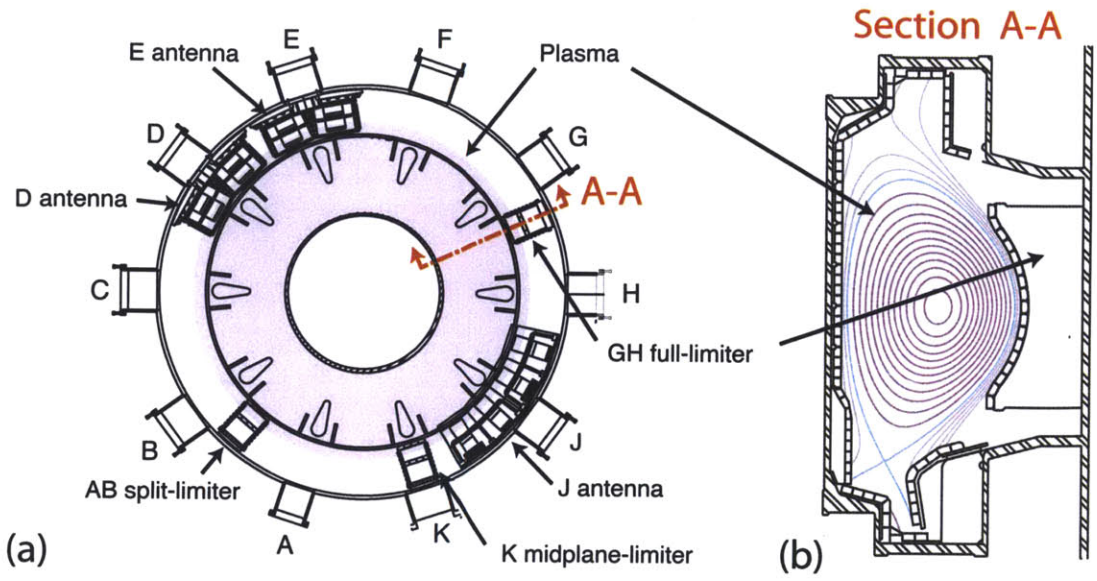

Figure 1-7: Alcator C-Mod shown in top view (a), and poloidal cross section (b).

have similar single-pass ICRF wave absorption to that of Alcator C-Mod. In addition, both experiments utilize high-Z plasma facing components (PFC) in the divertor, and contain plasmas where the scrape-off-layer (SOL) is opaque to neutrals [40]. Operational parameters for Alcator C-Mod are listed in table 1.1. A top view and poloidal cross section of the tokamak are shown in Fig. 1-7, and an image of the inside of the machine is shown in Fig. 1-8.

Table 1.1: Alcator C-Mod parameters

Major radius	R_0	$=$	0.67 m
Minor radius	a	$=$	0.22 m
Toroidal field	B_{T}	$\leq$	8 T
Plasma current	I_{p}	$\leq$	2 MA
Elongation	ϵ	$\sim$	1.7
Triangularity	δ	$\sim$	.4
Flat top duration	t	$\sim$	2 s
Inductive volt seconds	Φ	$\sim$	7 Wb
Average density	$\langle n \rangle$	$\leq$	$10^{21}\mathrm{m}^{-3}$
Central electron temperature	T_{e0}	$\leq$	5 keV

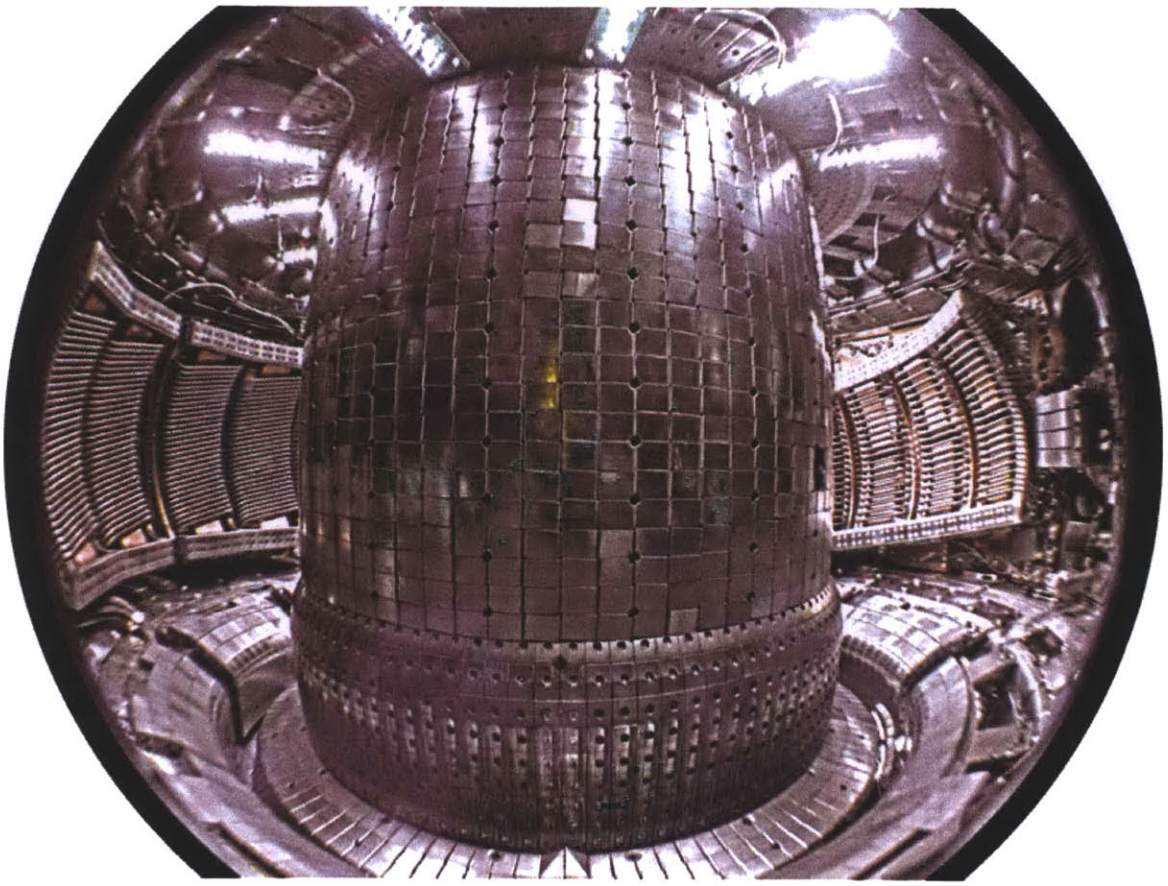

Figure 1-8: High dynamic range composite image of the inside of Alcator C-Mod taken from B-port (see Fig. 1-7). Two conventional ICRF antennas (D-port and E-port) are visible to the left of the central column. The new field-aligned antenna (J-port) is visible to the right of the central column.

Typically, Alcator C-Mod operates using a divertor, which allows a magnetic topology that prevents closed magnetic flux surfaces from intersecting the walls of the machine. However, it can also be operated with limited discharges, where closed flux surfaces intersect the walls, using either the inner wall, or poloidal limiters shown in Fig. 1-7. The structure consists of a stainless steel vacuum chamber encased in a cryostat. The inside of the machine is armored with TZM molybdenum refractory tiles, visible in Fig. 1-8. The vacuum vessel is divided into ten sections and has ten horizontal and twenty vertical ports (labeled A-K in Fig. 1-7) to provide access to the plasma for diagnostics, ICRF transmission lines and LH waveguides. Several sets of magnetic coils are used to confine and control the plasma. All of the coils are copper conductors cooled to liquid nitrogen temperatures to minimize resistive losses. There

are twenty toroidal coils (carrying a total current of 265,000 Amperes during a pulse), which wrap around the central core, producing a peak magnetic field of 22 T at the center of the device. These magnets produce extremely large self-forces (100 MN). As a result, a series of wedge plates, massive cover plates and super alloy draw bars are used to prevent the device from exploding under the loads produced during a plasma discharge. These loads are so large that the cover plates on the top and bottom of the machine, which are 3 m in diameter, 0.66 m thick, and weigh 31,000 kg each, flex over 3 mm during a pulse. In addition to the toroidal coils there are four sets of poloidal coils and a central solenoid.

A typical discharge lasts 1-2 seconds and uses approximately 500 MJ of energy. This energy is provided by a 10 m long, 200,000 kg alternator that is magnetically braked to translate rotational kinetic energy into electrical energy for the tokamak. At 1800 rpm, the alternator stores approximately 5 billion joules of energy. Approximately 20-30 discharges can be run during a single day, with 20 minutes in between. During this time the magnets have adequate time to cool down and the alternator can spin back up to its pre-discharge speed using power drawn from the Cambridge electrical grid. For each discharge, extensive data are taken for almost every machine parameter and diagnostic system. These data are stored in networked servers to be accessed by graduate students, scientists and engineers.

To review, tokamak fusion reactors (including current machines and future devices like ITER) utilize a large toroidal magnetic field, a smaller poloidal magnetic field produced by the toroidal current in the plasma. In addition, vertical field coils are used to control the radial position of the plasma, and various error field coils and shaping coils are necessary to optimize the plasma shape inside the vacuum vessel. A central solenoid is used to generate and control the plasma current. This describes a simple methodology for confining the plasma in a particular region. However, as will be shown in the next chapter, instabilities and fluctuations within the plasma increase the rate at which particles diffuse across the magnetic field far beyond what is predicted by analytical and numerical tools.

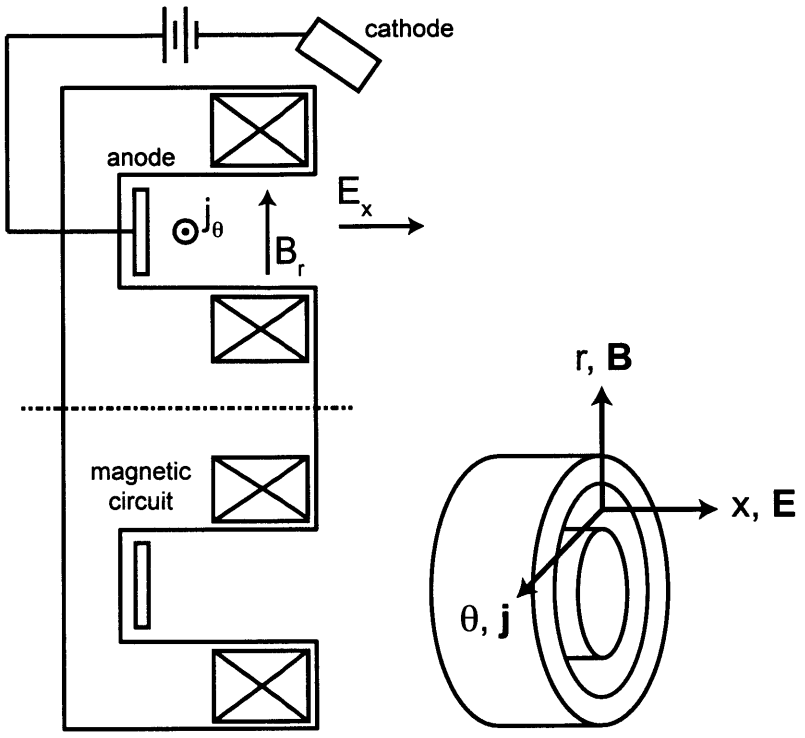

Figure 1-9: Cross section of Hall thruster topology, showing applied magnetic and electric fields and Hall current directions.

1.1.3 Hall thrusters

Hall thrusters are extremely fuel efficient plasma accelerators, used for low thrust space applications. The basic topology of a Hall thruster includes an annular ionization and acceleration channel. Propellant (typically xenon) is fed into the base of the channel, which contains an anode. A radial magnetic field is imposed to confine the electrons axially ($\rho_e \ll L_{\text{thruster}}$) while not confining the ions ($\rho_i \gg L_{\text{thruster}}$). An axial electric field forms between the anode and the confined electrons, which create a "virtual" cathode near the thruster exit. This electrostatic field accelerates the ions to an exit velocity:

$$v_i = \sqrt{\frac{2e\phi}{m_i}}, \tag{1.10}$$

where ϕ represents the potential at the ionization location in the annulus. In addition, quasineutrality in the channel dictates the absence of a space charge limit found in ion engines. This, combined with a significantly longer acceleration region, allows Hall thrusters to operate at much higher thrust densities than are physically possible in ion engines. Collisionality is low in these devices and the electrons drift azimuthally in the $E \times B$ direction, with a velocity given by:

$$v_\theta = \frac{\mathbf{E} \times \mathbf{B}}{B^2}. \tag{1.11}$$

The name "Hall thruster" comes from the mechanism that produces thrust. The electrons create an azimuthal current:

$$j_\theta = -en_\mathrm{e}\frac{\mathbf{E} \times \mathbf{B}}{B^2}. \tag{1.12}$$

as they drift (a Hall current) which, crossed with the magnetic field produces the axial thrust force ($j_\theta \times B_\mathrm{r}$). As mentioned previously, these plasma accelerators require electrons to be magnetically confined, while allowing ions to flow freely. To quantify this criteria, we first require the electron Larmor radius to be smaller than the scale length of the thruster:

$$\rho_\mathrm{e} = \frac{v_{\mathrm{e,\,th}}}{\Omega_\mathrm{e}} = \frac{m_\mathrm{e}}{eB}\sqrt{\frac{8kT_\mathrm{e}}{\pi m_\mathrm{e}}} \ll L. \tag{1.13}$$

Similarly, we also require the ion Larmor radius to be larger than the scale length of the thruster:

$$\rho_\mathrm{i} = \frac{v_{\mathrm{i,\,th}}}{\Omega_\mathrm{i}} = \frac{m_\mathrm{i}}{eB}\sqrt{\frac{2e\phi}{m_\mathrm{i}}} \gg L, \tag{1.14}$$

where ϕ represents the net accelerating voltage of the thruster. In addition, to quantify the magnetization of the electrons, we can define the Hall parameter:

$$\beta = \frac{\Omega_\mathrm{e}}{\nu_\mathrm{e}} \gg 1 \tag{1.15}$$

which, as the ratio of cyclotron frequency to total collision frequency, implies that the electron will gyrate many times around a magnetic field line before colliding with a neutral or ion.

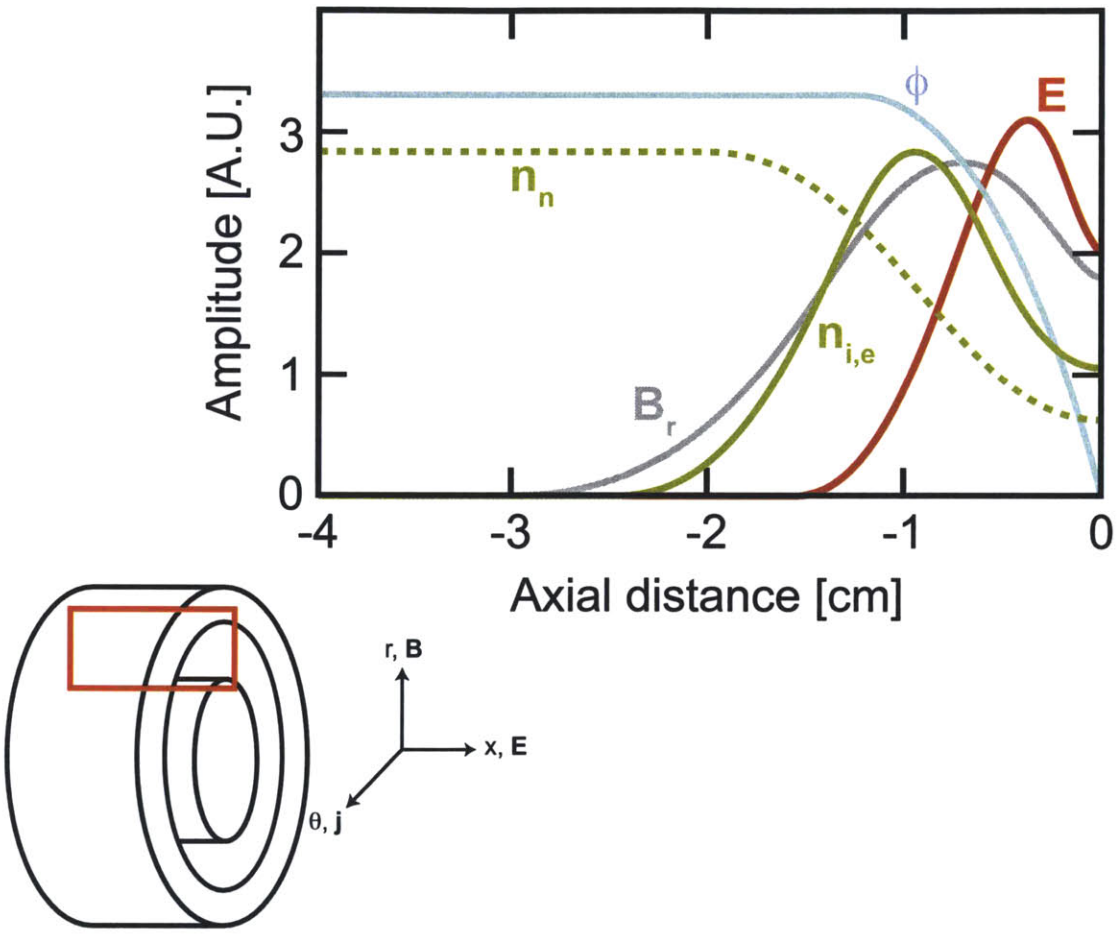

Figure 1-10: Qualitative Hall thruster plasma parameters as a function of axial distance from the exit plane: electric field E, plasma potential ϕ, radial magnetic field B_r, neutral density n_n, and plasma density $n_\mathrm{i,e}$.

As mentioned above, one salient feature of Hall thrusters is the presence of an externally applied electric field, E_x which is oriented perpendicular to the applied radial magnetic field, B_r producing an azimuthal, $E_\mathrm{x} \times B_\mathrm{r}$ drift velocity. The ions, which have a much larger $\sim m_\mathrm{i}/m_\mathrm{e}$ Larmor radius, are unmagnetized and thus accelerated by the applied electric field in the $\hat{\mathrm{x}}$ direction. The electrons are confined by the radial magnetic field. Generally, these plasma accelerators utilize an external

cathode, which both neutralizes the ion rich exhaust plume and provides electrons for the annular discharge. Figure 1-10 shows qualitative Hall thruster plasma parameters as a function of axial distance from the exit plane. Approximate peak values for the parameters shown are: typical electric field $E \sim 25$ kV/m, typical plasma potential $\phi \sim 200$ V, typical radial magnetic field $B_r \sim 0.02$ T, typical neutral density $n_n \sim 1.5 \times 10^{19}$ m^{-3}, and plasma density $n_{i,e} \sim 5 \times 10^{17}$ m^{-3}. [41]

Hall thrusters have been studied since the 1960s and were first flown on spacecraft in 1971 on the Russian Meteor spacecraft. These thrusters are very fuel efficient relative to their chemical counterparts. They are ideally suited for low thrust applications like orbit station keeping and large Δv missions where small accelerations are acceptable. In spite of the long history of research and development, some details of their operation are still not well understood. One extremely important problem is anomalous cross-field electron mobility, which can be orders of magnitude higher than classical predictions. Minimization of the axial (cross-field) electron transport toward the anode is a primary driver of Hall thruster efficiency. Similarly to tokamaks, this transport is observed to be anomalous and is enhanced by plasma turbulence. [25] Hall thruster plasmas contain numerous turbulent fluctuations occurring across a broad range of frequencies and it is generally believed that fluctuations resulting from various plasma instabilities contribute to anomalous mobility. [20]

The background, observed instabilities, simulation, results and conclusions of this thesis are discussed in the following chapters. Observations of fluctuation induced cross-field transport in tokamaks are presented in Ch. 2. Chapter 3 pertains to Hall thruster instabilities and fluctuation induced cross-field transport. Comparisons of cross-field transport characteristics are given in Ch. 4. Finally, conclusions and future work are given in Ch. 5.

Chapter 2

Tokamak Fluctuations

2.1 Physics of Instabilities

2.1.1 Background

Different types of instabilities, including low-frequency electrostatic drift waves (with frequencies lower than the ion cyclotron frequency) can cause fluctuations and enhanced transport in tokamaks. [1] These drift wave driven fluctuations manifest as microturbulence in the plasma and lead to anomalously high cross-field transport. [42, 43, 44] Microturbulence was first observed in tokamaks in 1976. Mazzucato, et al. [45] measured this microturbulence using radio frequency waves, which were scattered off of electron density fluctuations in the plasma, inside the Adiabatic Toroidal Compressor at Princeton. Today, microturbulence is universally observed in tokamak plasmas.

Traditionally, there has been no simple theoretical model of underlying physics to account for anomalous electron transport. As a result, numerous empirical scaling laws were developed over time to quantify the global confinement time, τ_E. [1] These include the Alcator scaling:

$$\tau_E \propto \bar{n}a^2, \tag{2.1}$$

which depends linearly on density and quadratically on minor radius, a. In this

scaling, as well as several below, magnetic field dependence is implicit through density. [46] For optimum temperature and fixed beta ($\beta = 2\mu_0 p/B^2$), the optimum density is proportional to the toroidal magnetic field: ($n_{\text{optimum}} \propto B_\phi$). [47] Following the Alcator scaling is the Pfeiffer-Waltz scaling:

$$\tau_{\text{E}} = 7.4 \times 10^{-22} \langle n \rangle a^{1.25} R^2, \tag{2.2}$$

which shows an almost linear dependence on minor radius, but a quadratic dependence on major radius, R. The INTOR scaling law adds a constant coefficient to the Alcator law:

$$\tau_{\text{E}} = 5 \times 10^{-19} \bar{n} a^2, \tag{2.3}$$

for ohmically heated tokamaks in low density regimes. However, for neutral beam heated experiments and other tokamaks, the INTOR model did not accurately reflect observed confinement time. Another empirical scaling, the Merezhkin scaling, showed a strong dependence on major radius, but only slight dependence on minor radius:

$$\tau_{\text{E}} = \frac{3.5 \times 10^{-21} \left(\frac{a}{R}\right)^{0.25} q\,(a)\, n R^3}{\sqrt{\langle T_{\text{e}} \rangle}}, \tag{2.4}$$

where the edge safety factor is given by:

$$q(a) = \frac{\#\text{ toroidal field line transits}}{\#\text{ poloidal field line transits}} \tag{2.5}$$

Later, a Neo-Alcator scaling law was developed that showed a linear dependence on density and minor radius, while strongly depending on major radius:

$$\tau_{\text{E}} = 1.3 \times 10^{-21} \bar{n} R^{2.04} a^{1.04}. \tag{2.6}$$

In 1984, Goldston combined a Neo-Alcator ohmic scaling with an auxiliary scaling to quantify total global energy confinement time in auxiliary heated plasmas:

$$\tau_{\mathrm{E}} = \frac{1}{\sqrt{\left(\frac{1}{\tau_{\mathrm{E}}^{\mathrm{aux}}}\right)^2 + \left(\frac{1}{\tau_{\mathrm{E}}^{\mathrm{ohm}}}\right)^2}}, \tag{2.7}$$

where the auxiliary confinement time is:

$$\tau_{\mathrm{E}}^{\mathrm{aux}} = 6.4 \times 10^{-8} I R^{1.75} a^{-0.37} \sqrt{\kappa} \sqrt{P_{\mathrm{tot}}}, \tag{2.8}$$

where I is the plasma current in amperes, P_{tot} is the total input power in watts, and κ is the plasma elongation. The ohmic confinement time is:

$$\tau_{\mathrm{E}}^{\mathrm{ohm}} = 7.1 \times 10^{-22} q \bar{n} R^{2.04} a^{1.04}. \tag{2.9}$$

Some optimism came in 1982 in the form of an enhanced confinement regime on ASDEX. This "high" confinement mode or H-mode roughly doubled the energy confinement time. However, the collective understanding of the underlying physics and relationships between different scaling laws and anomalous transport remain incomplete to this day.

2.1.2 Fluctuations

The electric and magnetic fields inside a tokamak plasma fluctuate; as these fluctuations occur, the particles' position and velocity also fluctuate. In 1985, P. Liewer characterized fluctuations in density on various tokamaks. [1] These density fluctuations are plotted against gradient scale length in Fig. 2-1 for various experiments. For low frequency oscillations, where $\omega \ll \omega_{\mathrm{ci}}$, the radial velocity of the particle fluctuates as: [1]

$$\tilde{v}_{\mathrm{r}} \approx \frac{\tilde{E}_\theta}{B} + \frac{v_\parallel \tilde{B}_{\mathrm{r}}}{B}, \tag{2.10}$$

where $\tilde{E}_\theta$ is the fluctuating poloidal electric field and $\tilde{B}_{\mathrm{r}}$ is the fluctuating radial magnetic field. However, the cross-field transport of particles and energy depends on the correlation of fluctuations of different plasma parameters, in addition to the

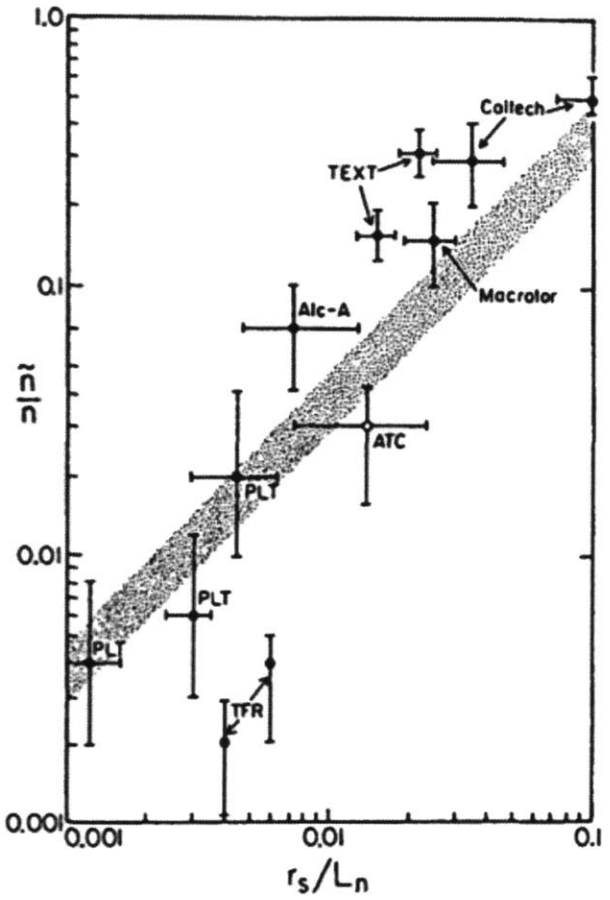

Figure 2-1: Measured fluctuation levels $\tilde{n}/n$ vs. r_s/L_n for various tokamaks. Figure from Liewer, et al. [1]

amplitude of the fluctuations themselves. Therefore, we can quantify the fluctuations of different plasma parameters by separating the time-averaged part of a parameter from a fluctuating part. For example, we can write a quantity, Q as:

$$Q = \langle Q \rangle + \tilde{Q}. \tag{2.11}$$

Now we can calculate a fluctuation induced particle flux driven by defining flux as:

$$\Gamma = nv_r = (\langle n \rangle + \tilde{n})(\langle v_r \rangle + \tilde{v_r}). \tag{2.12}$$

Taking the turbulent part, we can define a turbulent particle flux as: [1]

$$\Gamma^{turb} = \langle \tilde{n}\tilde{v}_{\mathrm{r}} \rangle = \frac{\langle \tilde{n}\tilde{E}_{\mathrm{p}} \rangle}{B} - \frac{\langle \tilde{j}_{\parallel}\tilde{B}_{\mathrm{r}} \rangle}{eB}, \tag{2.13}$$

where

$$\tilde{j}_{\parallel} = -e \int_{-\infty}^{\infty} v_{\parallel} \tilde{f}_{\mathrm{e}} dv, \tag{2.14}$$

where $\tilde{f}_{\mathrm{e}}$ is the fluctuating electron distribution function. Similarly, using Braginskii's classical conductive heat flux:

$$\vec{q} = -K_{\parallel}\nabla_{\parallel}T - K_{\perp}\nabla_{\perp}T, \tag{2.15}$$

we can describe a turbulent radial heat flux: [1]

$$q_{\mathrm{r}}^{\mathrm{turb}} = -K_{\parallel} \left\langle \left| \frac{\tilde{B}_{\mathrm{r}}}{B} \right|^2 \right\rangle \frac{d\langle T \rangle}{dr} - K_{\parallel} \left\langle \left| \frac{\tilde{B}_{\mathrm{r}}}{B} \right| \frac{d\tilde{T}}{dr} \right\rangle. \tag{2.16}$$

Tokamak fluctuations can be categorized into microscopic and macroscopic modes based upon the perpendicular wavelength of the mode. Fluctuations with perpendicular wavelengths much shorter than the minor radius, $k_{\perp}a \gg 1$, are microscopic. These "microturbulence" fluctuations also have high poloidal mode numbers: $k_{\mathrm{p}}a \gg 1$, with $k_{\mathrm{p}} = m/r$, yielding $m \gg 1$. Fluctuations with perpendicular wavelengths of order minor radius, $k_{\perp}a \sim 1$ are macroscopic MHD modes and have low poloidal mode numbers.

The microscopic fluctuations are very broadband, and occur from 10 kHz to several MHz. Very little evidence suggests any coherent modes, $\Delta\omega \ll \omega$, exist for these high-m modes. These modes exhibit a very broad spectrum for a given wavenumber; the spectral distribution, $S(\vec{k},\omega) = |\tilde{n}(\vec{k},\omega)|^2$ has a wide frequency spread for each $\vec{k}$ and $\Delta\omega \sim \omega$. Density fluctuations across a large portion of the plasma can be clearly seen in Fig. 2-2, for early measurements on Alcator A. As Liewer [1] points out, spectra with $\Delta\omega \sim \omega$ indicate a strongly turbulent regime where numerous modes of different wavenumber interact non-linearly. This interaction broadens the spectra: $\Delta\omega \cong 1/\tau_{\mathrm{auto}}$, where τ_{auto} is the autocorrelation time of the mode. In addition,

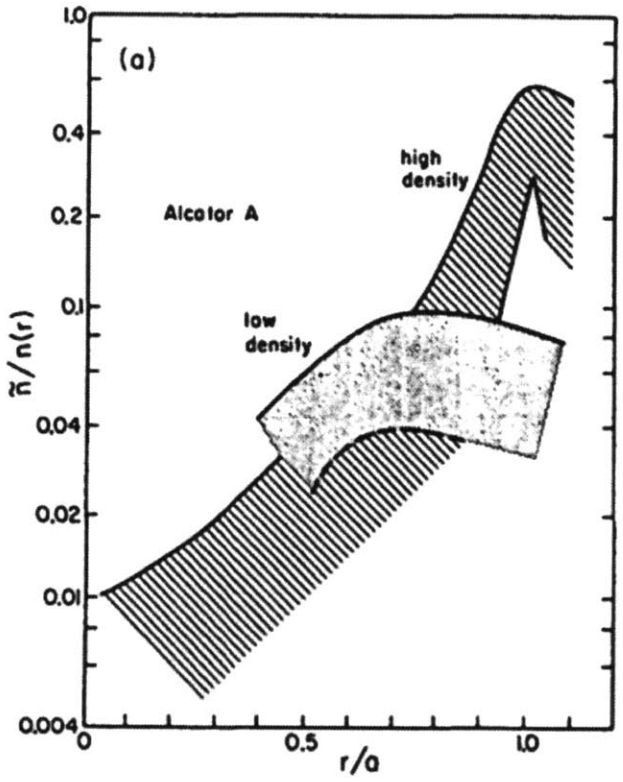

Figure 2-2: Spectrum of density fluctuations vs minor radius in the Alcator A tokamak for high and low density. Figure from Liewer, et al. [1]

most of the spectral energy is found in the region $k_\perp c_s/\Omega_i < 1$. The relative density fluctuation level $\tilde{n}/n$ increases with tokamak radius and is largest near the edge where large density gradients exist. Also, the perpendicular wavenumber of these fluctuations is much larger than the parallel wavenumber, $k_\perp \gg k_\parallel$. The cross-field magnetic fluctuations are much larger than fluctuations parallel to the magnetic field. The turbulent fluctuations are generally found to drift in the electron diamagnetic drift (EDD) direction at low densities and to drift in the ion diamagnetic drift (IDD) direction at high densities.

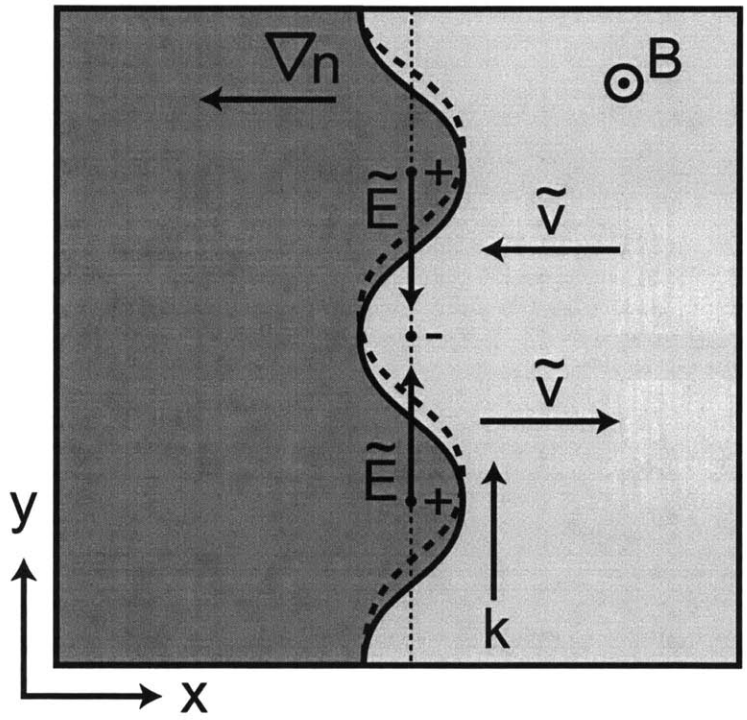

Figure 2-3: Schematic of drift wave physics mechanism for density fluctuation.

2.1.3 Drift Waves

Plasma turbulence is quite different from neutral fluid turbulence, not only because of the presence of charged particles, but because of the plethora of waves within the plasma. Drift waves are found in all magnetized plasmas, and provide a fundamental mechanism for cross-field transport of particles, momentum, and energy. Horton,

et al. [48] [49] points out that plasma turbulence is in many ways more similar to geostrophic flows on rotating planets than to neutral fluid turbulence. The drift wave is analogous to the Rossby wave in these planetary systems. [49] The local density and temperature gradients provide free energy sources for drift waves. Drift waves have a small electric field component along B, so electrons can travel along B to achieve thermodynamic equilibrium, following the Boltzmann relation: [50]

$$\frac{\tilde{n}}{n} = \frac{e\tilde{\phi}}{kT_e}. \tag{2.17}$$

For the top and bottom points in Fig. 2-3, the density is larger, $\tilde{n}$ is positive and thus $\tilde{\phi}$ is also positive. The central point has a negative $\tilde{n}$ and $\tilde{\phi}$, so a fluctuating electric field points toward the central point. $E \times B$ drifts move particles in and out as shown, changing the local density. The isobaric density front moves from the solid line shown, to the dashed line. To quantify the physics of drift waves, we can neglect gyro-motion, using guiding center equations. We can derive the electrostatic dispersion relation for drift waves, using Eq. 2.17 and the perpendicular ion velocity: [51]

$$v_{i\perp} = -\frac{\nabla\phi \times B}{B^2} - \frac{m_i}{eB^2}\frac{d}{dt}\left(\nabla_\perp \phi\right). \tag{2.18}$$

Ion momentum is given by:

$$n_0 m_i \frac{dv_{i\parallel}}{dt} = -\nabla_\parallel \left(n_0 e\phi + \gamma T_{i0} n_{i1}\right), \tag{2.19}$$

where T_{i0} is the background ion temperature, n_0 is the background density, n_{i1} is the perturbed density, and γ is the adiabatic index. Continuity is simply:

$$\frac{\partial n_{i1}}{\partial t} + \nabla \cdot (n_0 \vec{v}_i) = 0. \tag{2.20}$$

For a slab geometry, shown in Fig. 2-3, where B is in the z-direction and density varies along the x-direction, we can solve for a simple drift wave: [51]

$$\phi = \phi(x) e^{i(k_y y + k_\parallel z - \omega t)}. \tag{2.21}$$

We find the dispersion relation for these modes is given by:

$$\omega^2 \left(1 + \frac{T_e k_y^2 \rho_{Li}^2}{2T_i}\right) - \omega\omega_* - c_s^2 k_\parallel^2 = 0, \tag{2.22}$$

where ρ_{Li} is the ion Larmor radius, and the sound speed, c_s is simply:

$$c_s = \sqrt{\frac{T_e + \gamma T_i}{m_i}}, \tag{2.23}$$

and the diamagnetic drift frequency, ω_*, is given by:

$$\omega_* = -\frac{k_y T_e}{eBn_0}\frac{dn_0}{dx}. \tag{2.24}$$

The $\omega\omega_*$ term above arises from the $E \times B$ convection that convects particles along the density gradient, as illustrated qualitatively in Fig. 2-3. This term is important for only those waves, which propagate nearly perpendicular to the magnetic field. In other words, we require the condition:

$$\frac{k_\parallel}{k_y} \leq \frac{\rho_{Li}}{L_n}. \tag{2.25}$$

This condition provides the drift wave solution to the dispersion relation above:

$$\omega_{DRIFT} = \frac{\omega_*}{1 + \frac{k_y^2 \rho_{Li}^2}{2}}. \tag{2.26}$$

In a homogeneous plasma, the wave is damped by electron flow along the magnetic field. However, in an inhomogeneous plasma, the $E \times B$ convection converts some of the cross-field pressure gradient into a parallel pressure gradient, which can grow the instability. [51] As mentioned above, the local density gradient provides one free energy source for drift waves. When the gradient of the fluctuations $k_\perp \tilde{n}$ is large enough to flatten out the local density gradient, the turbulence saturates. Here the saturation level, or "mixing" level occurs at:

$$\frac{\tilde{n}}{n} \sim \frac{1}{\langle k_\perp \rangle L_\mathrm{n}}, \tag{2.27}$$

where $\langle k_\perp \rangle$ is an average perpendicular wavenumber and L_n is the gradient scale length, given by:

$$L_\mathrm{n} = \frac{1}{\left| \frac{d \ln n}{dx} \right|}. \tag{2.28}$$

In addition to density gradients, temperature gradients and other inhomogeneous plasma properties drive a non-linear interaction between drift waves. In order to assume purely electrostatic modes the plasma beta must be small:

$$\beta = \frac{n_\mathrm{e} T_\mathrm{e} + n_\mathrm{i} T_\mathrm{i}}{B^2 / 2\mu_0} \ll 1. \tag{2.29}$$

If we use this low beta limit, which is typical for Alcator C-Mod plasmas, magnetic fluctuations are ignored and the modes are electrostatic with perturbed field given by:

$$\tilde{E} = -\nabla \tilde{\phi}. \tag{2.30}$$

2.1.4 Nonlinear wave interactions

Turbulence in magnetized plasmas generally manifests through a nonlinear interaction among several distinct instabilities or waves. To describe the linearly evolving momentum of any fluid, the convective derivative $v \nabla v$, is ignored. For a nonlinear description, this term is included and provides a mechanism for nonlinear wave interactions to produce a turbulent spectrum of fluctuations. As Scott [52] points out, waves producing turbulence driven by a typical $\mathbf{E} \times \mathbf{B}$ velocity are coupled via a quadratic nonlinearity. This quadratic nonlinearity arises through three wave coupling. Here, a wave $\mathbf{k}_0$ is driven by two other waves $\mathbf{k}_1$, and $\mathbf{k}_2$, which beat together. [52] Momentum and energy are conserved, such that $\mathbf{k}_0 + \mathbf{k}_1 + \mathbf{k}_2 = 0$ and $\omega_0 + \omega_1 + \omega_2 = 0$. [19] Nonlinear analysis of these modes can be simplified for certain conditions by simply treating a single wave interacting with the background. In this

case, the effects are treated quasilinearly. The difference between a linear treatment of turbulence and a quasilinear treatment is that the waves can change the background mode in the quasilinear case. However, in typical magnetized plasma turbulence a true three way coupling manifests among all the waves present, resulting in numerous degrees of freedom in the system.

Similar to the quasilinear interactions, the nonlinear three wave interactions are independently fairly coherent. However, the large number of three wave interactions produces a very incoherent spectrum. Interactions at a given location become uncorrelated outside a timescale, called the correlation time. [52] This correlation time is shorter than the time to respond to the changing background, but longer than the eddy turnover time. Thus, these interactions lose "memory" of an initial state and slowly saturate. The state is considered saturated when the waves individually fluctuate, but collectively maintain a constant level of free energy. [52]

Once these interactions and modes within the plasma become unstable, they contribute to the turbulent anomalous transport observed in tokamak plasmas. Four of the most significant instabilities are: the electron drift mode, the Electron Temperature Gradient (ETG) mode, the Ion Temperature Gradient (ITG) mode, and the Trapped Electron Mode (TEM). These instabilities can be separated into modes, which result from either trapped or passing particles in tokamaks.

2.1.5 Passing Particle Modes

2.1.5.1 Electron Drift Mode

Following the excellent derivation by Wesson [2], the physics of the electron drift mode can be investigated, beginning with the gyro-kinetic equation:

$$v_{\parallel}\frac{\partial g}{\partial l} - i(\omega - \mathbf{k}\cdot\mathbf{v}_{\mathrm{d}})g - i\frac{e\tilde{\phi}}{m_{\mathrm{i}}}J_0(z)\left[\frac{k_\theta}{\Omega_{\mathrm{i}}}\frac{df_{\mathrm{M}}}{dr} + \omega\frac{df_{\mathrm{M}}}{dK},\right] = 0, \tag{2.31}$$

where dl is a poloidal arc length element and dr is a radial element from a flux surface, and g is a modified distribution for the ions. The equilibrium drift velocity is v_{D}, $\mathbf{k}$ is the wave vector, K is the particle energy, and f_{M} is a Maxwellian velocity

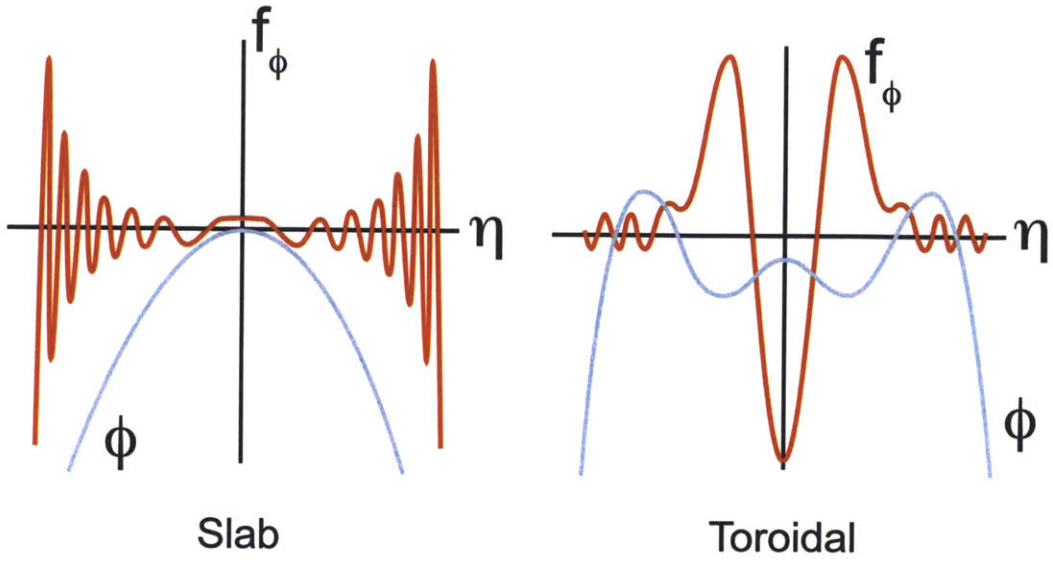

Figure 2-4: Electron drift mode potential ϕ and corresponding eigenfunction f_ϕ for the slab and toroidal modes as a function of $\eta = L_n/L_T$. (adapted from Wesson [2])

distribution. The Bessel function $J_0(z)$ is defined as:

$$J_0(z) = \frac{1}{2\pi}\int e^{-iz\cos\phi} d\phi. \tag{2.32}$$

After solving for g and expanding, we obtain the following eigenvalue equation: [2]

$$\left[\rho_i \frac{\partial^2}{\partial x^2} - \left(\frac{\epsilon_n}{k_\theta \rho_i \tau q \omega_{MD}}\right)^2 \left(\frac{\partial}{\partial\theta} + ik_\theta s x\right)^2 - \frac{2\epsilon_n}{\tau\omega_{MD}}\left(\cos\theta + \frac{i\sin\theta}{k_\theta}\frac{\partial}{\partial x}\right) - \left(\frac{\omega_{MD}-1}{\tau\omega_{MD}+(1+\eta_i)} + (k_\theta\rho_i)^2\right)\right]\tilde{\phi} = 0, \tag{2.33}$$

where ω_{MD} represents the mode frequency normalized to the electron drift frequency, k_θ is the poloidal wavenumber, $b = (k_\theta\rho_i)^2$, s is the magnetic shear, and $\epsilon_n = L_n/R$. If the curvature term is eliminated, and $dT_i/dr = 0$ is assumed, an equation describing the mode structure of the electron drift mode is obtained: [2]

$$\left[\frac{\rho_i^2}{(nq')^2}\frac{\partial^2}{\partial x^2} + \left(\frac{\epsilon_n s k_\theta}{k_\theta \rho_i \tau q}\right)^2 x^2 - \left(\frac{\omega_{MD}-1}{\tau+1} + (k_\theta\rho_i)^2\right)\right]\tilde{\phi} = 0, \tag{2.34}$$

where ω_{MD} is of order 1 (i.e. the frequency of the mode is approximately equal to the electron drift frequency). For the toroidal electron drift mode, $\tilde{\phi}$ is expanded in Fourier harmonics to obtain a modified eigenmode equation:

$$\left[\left(\frac{\sigma}{\omega_{MD}}\right)^2 \frac{\partial^2}{\partial\eta^2} + \eta^2 + \left(\frac{\alpha}{\omega_{\mathrm{MD}}}\right)[\cos(\eta-\theta_0) + s\eta\sin(\eta-\theta_0)] + \lambda(\theta_0)\right]\tilde{u} = 0, \tag{2.35}$$

where $\alpha = 2\epsilon_{\mathrm{n}}/bs^2\tau$, $\sigma = \epsilon_{\mathrm{n}}/bs\tau q$, and the eigenvalue is given by:

$$\lambda = \frac{1}{bs^2}\left(\frac{\Omega-1}{\tau\Omega+1+\eta_{\mathrm{i}}} + b\right). \tag{2.36}$$

Figure 2-4 provides a visualization of both the potential and corresponding eigenfunction for the slab ($\alpha = 0$) and the toroidal ($\alpha = 3$) modes as a function of $\eta = L_{\mathrm{n}}/L_{\mathrm{T}}$. [2]

2.1.5.2 Ion Temperature Gradient Mode

The Ion Temperature Gradient (ITG) mode, or η_{i} mode, is generally regarded as one of the primary contributors to anomalous transport in tokamak plasmas. The simplest topology to analyze the physics of ITG turbulence is the slab model. In the slab model, toroidal effects do not contribute, and the radial ion pressure gradient interacts with ion acoustic waves in the plasma. In a slab, for $\eta_{\mathrm{i}} \gg 1$ (η_{i} is the gradient scale length ratio between density and temperature, given in Eq. 2.40), the growth rate is given by:[43]

$$\gamma_{\mathrm{ITG,\ SLAB}} \sim \left(k_{\parallel}^2 c_s^2 \eta_{\mathrm{i}} \omega_{*\mathrm{i}}\right)^{1/3}, \tag{2.37}$$

where,

$$\omega_{*\mathrm{i}} = \frac{k_{\mathrm{y}} D}{L_{\mathrm{n}}}, \tag{2.38}$$

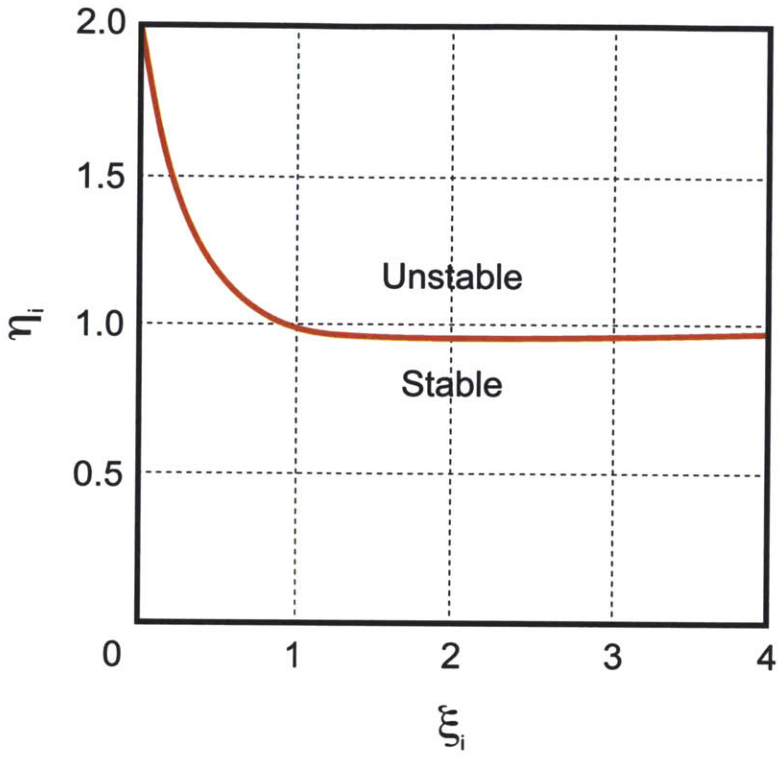

Figure 2-5: Slab ITG stability threshold.

with,

$$D = \frac{cT}{ZeB}, \tag{2.39}$$

and L_n is the density gradient scale length. We can visualize the stability criterion in terms of gradient scale lengths and Larmor radii, as shown in Fig. 2-5. The ratio of gradient scale lengths is given by:

$$\eta_i = \frac{L_n}{L_{Ti}}. \tag{2.40}$$

In addition, finite Larmor radius effects are introduced through:

$$\xi_i = \left(\frac{k_y v_{th,i}}{\Omega_i}\right)^2. \tag{2.41}$$

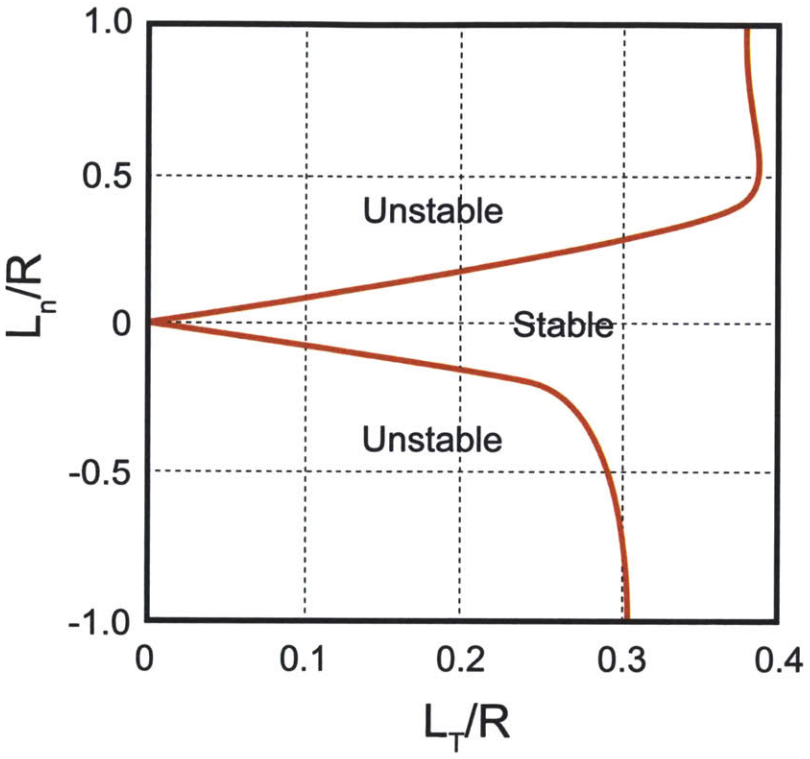

Figure 2-6: Toroidal ITG stability threshold.

In a tokamak, toroidal geometry effects become important and we obtain a growth rate of:

$$\gamma_{\text{ITG, TOK}} \sim (k_y \rho_i) \left(\frac{g_i}{L_{Ti}} \right)^{1/2}, \tag{2.42}$$

where g_i is a term representing the local curvature:

$$g_i = \frac{v_{th,i}^2}{R}, \tag{2.43}$$

and L_{Ti} is the ion temperature gradient scale length. As shown in Fig. 2-6, the toroidal ITG is unstable for strong T_i gradients and weak n_i gradients.

2.1.5.3 Electron Temperature Gradient Mode

As its name suggests, the Electron Temperature Gradient (ETG) mode, or η_e mode, is very similar to the ITG, except that it involves electrons instead of ions. The ETG mode is a contributor to electron transport in tokamaks; this mode is driven by both electron temperature gradients and magnetic field line curvature. Electron Temperature Gradient driven electron energy transport is characterized by relatively small fluctuations, which do not affect ion energy transport. In addition, the ETG mode is not generally influenced by large flows, which have been found to stabilize ITG modes. [53] For this mode, $k_\perp \rho_i \gg 1$, and the perpendicular wavelength is in between the Larmor radii of ions and electrons. [2] The linear growth rate is also very similar to the ITG:

$$\gamma_{\text{ETG, TOK}} \sim (k_y \rho_e) \left(\frac{g_e}{L_{Te}} \right)^{1/2}, \tag{2.44}$$

where $g_e = v_{Th,e}/R$. Contrasting this growth rate with that of the ITG, we see that the square root of the mass ratio (entering through g_e) increases the growth rate of this electron mode by a factor of ~ 60. There is less transport from this mode due to a higher k_y.

2.1.6 Trapped Particle Modes

2.1.6.1 Trapped Electron Mode

In a tokamak, trapped particles can establish different types of modes than passing particles. Two types of modes appear for trapped electrons, a dissipative and a collisionless Trapped Electron Mode (TEM). [54] The fraction of trapped particles goes as $\sim \sqrt{\epsilon}$ and the linear growth rate of the dissipative modes reflects this dependence, as seen here: [54]

$$\gamma_{\text{TEM, Dissipative}} \sim \frac{3\epsilon^{3/2} \omega_{*e}^2 \eta_e}{2\nu_{ei}}, \tag{2.45}$$

where $\epsilon = a/R$, and $\eta_e = L_{n_e}/L_{T_e}$. Again, the electron gradient scale lengths in density and temperature enter into the growth rate through the η_e and ω_{*e}^2 terms. The dissipative effect of collisions enters through ν_{ei}. The collisionless trapped electron mode also depends on the trapped particle fraction, but also on the density gradient scale length more so than the temperature gradient scale length. The linear growth rate for the collisionless TEM is given by:

$$\gamma_{\text{TEM, Collisionless}} \sim \frac{\omega_{*e}\sqrt{2\pi\epsilon}\eta_e R^{3/2}}{2L_n^{5/2}}\left(2R - 3L_n\right)e^{-R/L_n}. \tag{2.46}$$

These instabilities play a large role in anomalous particle and energy transport in tokamak plasmas.

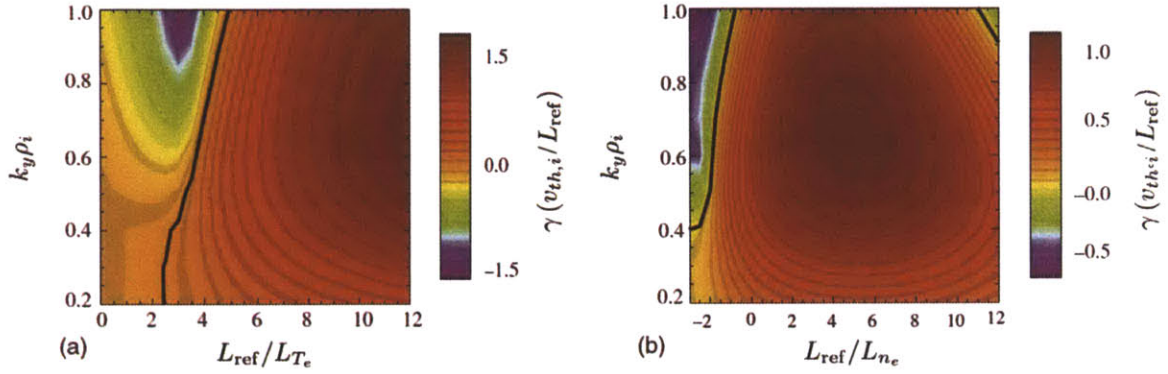

Figure 2-7: Micro Tearing Mode growth rate as a function of $k_y\rho_i$ for temperature (a) and density (b) gradient scale lengths. $\gamma = 0$ is indicated with the black line. (Dickenson, et al. [3])

2.1.7 Micro Tearing Modes

Micro Tearing Modes (MTMs) can also contribute to electron transport in tokamak geometries. Microinstabilities can cause resonant magnetic perturbations in tokamaks, if the microinstabilities have a so called "tearing" parity. These modes have been investigated in both spherical tokamak and large aspect ratio tokamak geometries and are found to be unstable in both. [3] These microtearing modes draw energy from gradients in the electron temperature [4] and are also found to be unstable inside the top of the pedestal region in tokamaks [3]. Figure 2-7 shows microtearing

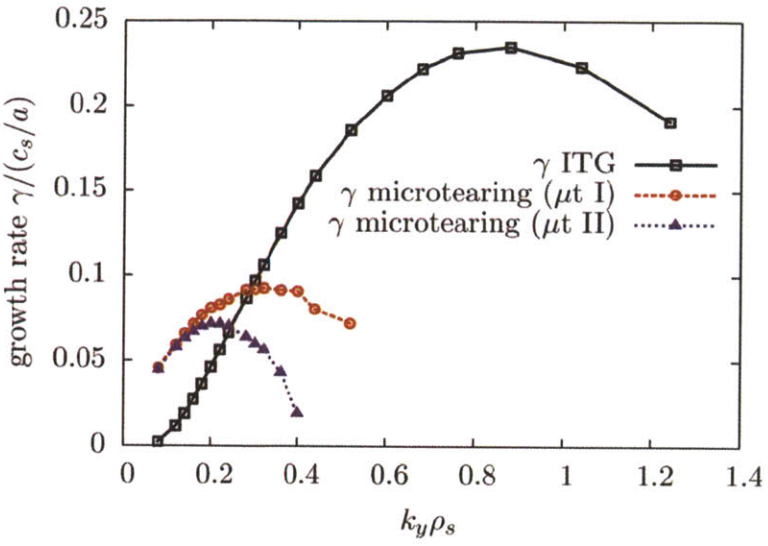

Figure 2-8: Micro Tearing Mode growth rates dominate in the low $k_y\rho_s$ region, where $\rho_t rms$ is the effective ion Larmor radius. At higher wavenumbers they exist with an ITG branch. (Doerk, et al. [4])

mode growth rate as a function of $k_y\rho_i$ for temperature (Fig. 2-7a) and density (Fig. 2-7b) gradient scale lengths. As Doerk, et al. points out, a tearing (odd) parity occurs when the parallel component of the fluctuating vector potential $\tilde{A}_{\|}$, is symmetric with respect to the tokamak midplane along a field line; then the resonant component of $\tilde{A}_{\|}$ is non-vanishing. This odd parity is important for these types of modes because unlike ballooning (even) parity modes (to which both ITGs and TEMs belong), these microtearing modes can create magnetic stochasticity via overlapping magnetic islands in the plasma. [4] As shown in Fig. 2-8, microtearing mode growth rates dominate in the low k_y region, while at higher wavenumbers they exist along with an ITG branch.

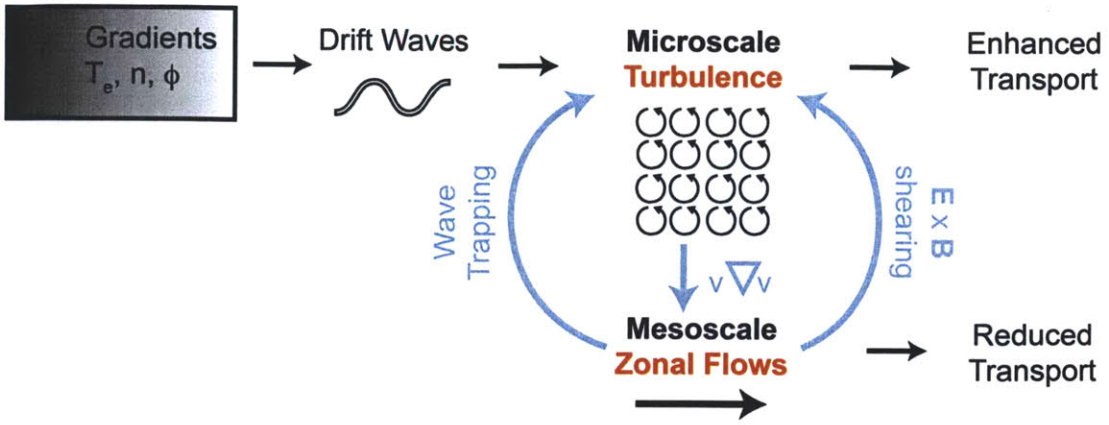

Figure 2-9: Schematic of microscale turbulence and zonal flow interaction. Zonal flows effectively reduce drift wave turbulence via $E \times B$ shearing, while drift waves also transfer energy to zonal flows via $v\nabla v$ nonlinearity. Through this mechanism, zonal flows can effectively suppress drift wave microturbulence. (Adapted from Fujisawa, et al. [5])

2.1.8 Zonal Flows

Fluctuation induced cross-field transport of both particles and energy can be ameliorated under certain plasma conditions. One such condition, for both particles and energy, is the high confinement regime (H-mode), mentioned previously that was discovered on ASDEX. Another "special" confinement regime, which enhances energy confinement while keeping particle confinement relatively constant is the I-mode, which was discovered on Alcator C-Mod. Both of these modes represent a bifurcation of the plasma confinement where the transport jumps up or down once a threshold in plasma parameters is reached. One mechanism, which is widely used to explain this bifurcation (and resulting stabilization of turbulence), is the development of quasi steady-state sheared flows within the plasma. Figure 2-10 shows the correlated structures of ITG turbulence and $\mathbf{E}\times\mathbf{B}$ zonal flow radial electric field. As seen in the figure, the turbulence is suppressed where E_r is large and vice versa. These flows are called *zonal flows*. [5] Zonal flows have zero frequency. These flows were first measured experimentally by Fujisawa, et al., on the compact helical system (CHS). [55] Zonal flows are not driven directly by free energy from gradients in plasma parameters, but instead by nonlinear drift wave interactions. [6]

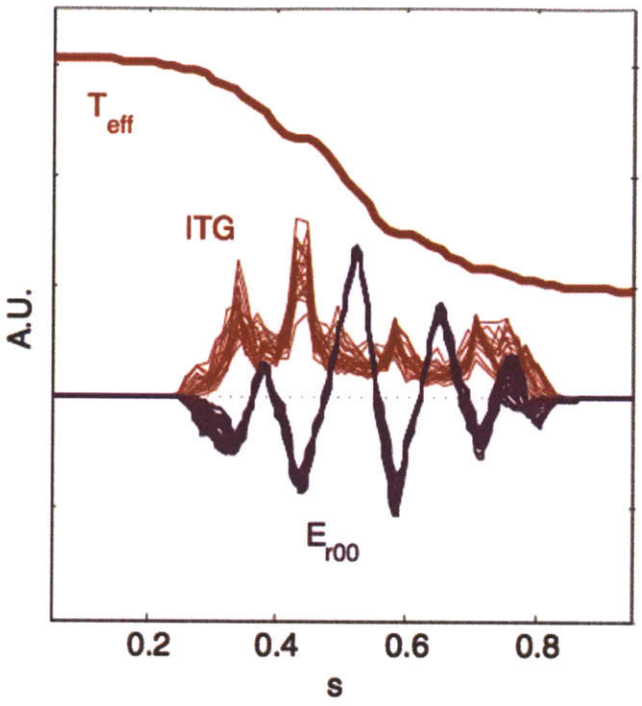

Figure 2-10: Time traces of temperature, $\mathbf{E} \times \mathbf{B}$ flow and ITG amplitude. (Diamond, et al. [6]

However, as Fujisawa, et al. [5] points out, the relationship between drift wave microturbulence and zonal flows is mutual. As shown schematically in Fig. 2-9, zonal flows effectively reduce drift wave turbulence via $\mathbf{E} \times \mathbf{B}$ shearing, while drift waves also transfer energy to zonal flows via $v\nabla v$ nonlinearity. Through this mechanism, zonal flows can effectively suppress drift wave microturbulence.

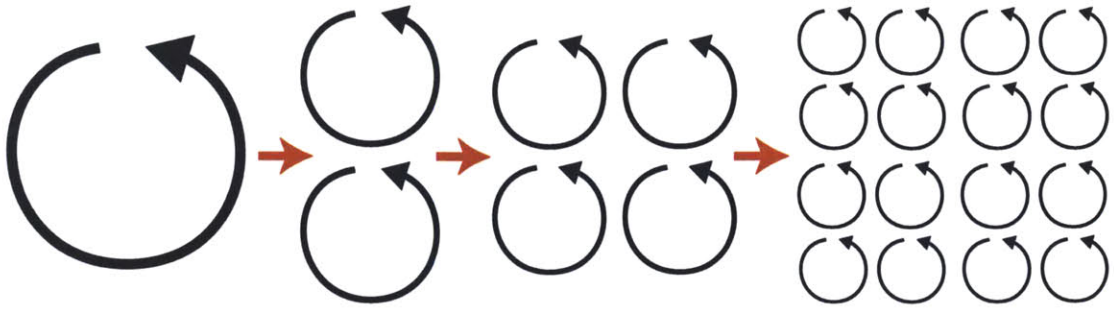

Figure 2-11: Cascade of energy from stirring, to inertial, to dissipation scales.

2.2 Observed Instabilities

2.2.1 Background

The wave number spectrum reveals much about the physical nature of turbulence. In 1941, Kolmogorov developed a theory of turbulence (K41 theory), which manifests as a cascade of energy from some initial "stirring" scale, through an inertial range of turbulence, into a dissipative sink at small scales, as shown schematically in Fig. 2-11. [56] The inertial range corresponds to an intermediate set of states where the turbulence has neither a source or sink for energy. This inertial range has been observed in fusion plasma experiments and also described for kinetic and space plasmas. [57] Kolmogorov found that the energy flux (or flow of energy at one wavenumber to another), scales as $\sim k^{-5/3}$. [56] Following this seminal work, numerous fusion experiments have measured wave number spectra that scales as $\sim k^{-5/3}$, as well as an energy cascade from stirring to dissipative scales. [7] Bale, et al., also found $\sim k^{-5/3}$ scaling in the solar wind at MHD scales and a cascade to ion scales via Alfven waves. [58], [7] In addition, Kraichnan, et al. [59] proposed a dual cascade theory for 2D neutral fluid turbulence. Fyfe, et al. [60] used this dual cascade theory to predict 2D plasma turbulence:

$$|\phi_k|^2 \sim k^{-14/3} \text{ for small } k, \tag{2.47}$$

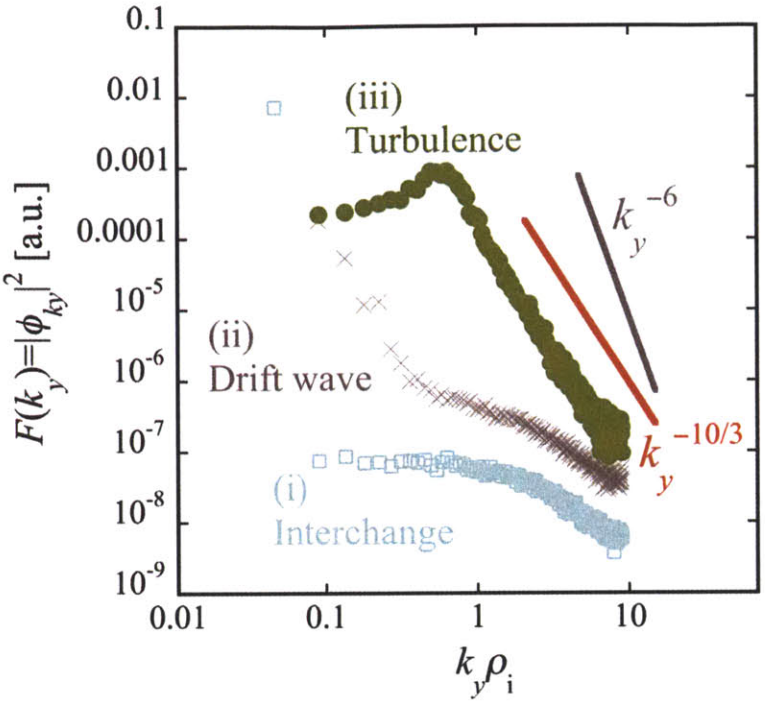

Figure 2-12: One dimensional spectra as a function of $k_y\rho_i$. Interchange mode, drift wave and turbulence are shown. (Kawamori, et al. [7])

and

$$|\phi_k|^2 \sim k^{-6} \text{ for large } k. \tag{2.48}$$

Here, ϕ_k is the potential fluctuation. For stirring sources of longer wavelengths and limited dissipation at small scales, the Hasegawa-Mima equation [61] displays this duality in energy cascade scales. [7] Cascade exponents for the the non-adiabatic component of the velocity-space ion distribution function h_i and the real-space potential ϕ have also been obtained. Schekochihin, et al., found: [62]

$$E_\phi(k_\perp) \sim k_\perp |\phi_{k_\perp}|^2 \sim k^{-10/3}, \tag{2.49}$$

and

$$E_h(k_\perp) \sim k_\perp |h_{k_\perp}|^2 \sim k^{-4/3}. \tag{2.50}$$

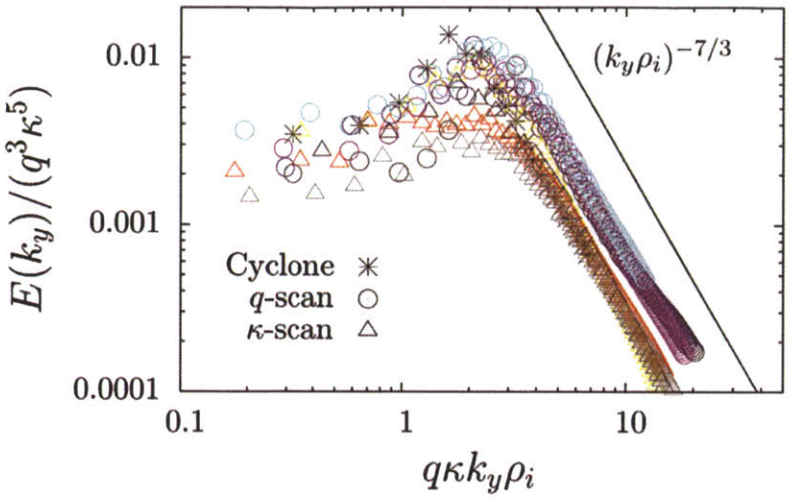

Figure 2-13: Electrostatic fluctuation spectra $E(k_y)$, for ITG turbulence. (Barnes, et al. [8])

This $k_\perp^{-10/3}$ dependence is clearly seen in Fig. 2-12 from Kawamori's measurements on MPX, using a fine scale Langmuir probe (FSLP). [7] Recently Hatch, et al. asserted that in tokamak plasmas there is actually significant turbulence dissipation at the same scales as the turbulence creation. In other words, for this turbulence, part of the "damping" occurs in the same range as the "stirring", although a cascade to smaller scales is still present. [63], [64]

Barnes, et al. establishes a 1D electrostatic fluctuation spectrum for ITB turbulence: [8]

$$E(k_y) \sim k_y \rho_i \left|\phi_k\right|^2 \sim q^{2/3} \left(\frac{R}{L_T}\right)^{8/3} (k_\perp \rho_i)^{-7/3}, \tag{2.51}$$

which is supported by numerical calculations using the gyrokinetic code GS2. Results of these runs are shown in Fig. 2-13. Note that for all cases shown, the numerical results follow the predicted values for the ITG inertial range.

On Tore Supra, high wavenumber investigations revealed a transition from low to high field. As shown in Fig. 2-14 (a), at high magnetic field the spectrum follows a power law $\sim k^{-6}$, while the spectrum follows a power law $\sim k^{-6.5}$ for low magnetic field. However, as can be seen in Fig. 2-14 (b), when Larmor radius is taken into account, the spectra agree quite well for both magnetic field strengths. Also evident

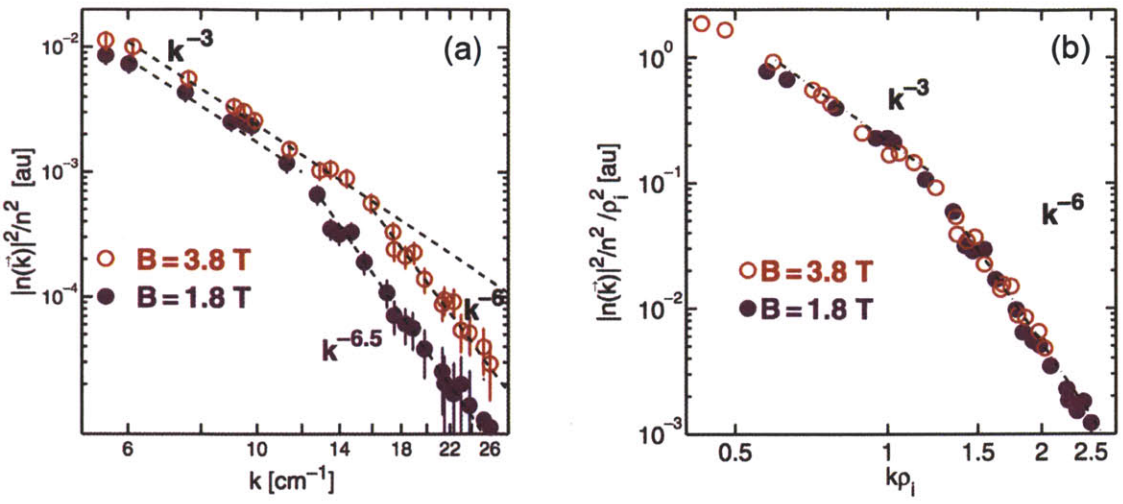

Figure 2-14: Tore Supra wavenumber spectrum of density fluctuations as a function of k are shown in (a) and wavenumber spectrum of density fluctuations divided by ρ_i^2 as a function of $k\rho_i$ are shown in (b), for two magnetic field levels. (Hennequin, et al. [9])

in Figs. 2-14 (a) and (b) is a clear transition in power law scaling at $\sim k\rho_i = 1$ from $\sim k^{-3}$ to $\sim k^{-6}$. [9]

Fluctuation induced cross-field transport is, of course, not limited to tokamaks within the regime of magnetic confinement fusion energy experiments. Stellarators and linear devices also exhibit fluctuation induced cross-field transport. Thakur, et al., found that in a cylindrical plasma device, transitions to turbulent states could be modified by augmentation of plasma boundary conditions. [10] Drift wave turbulence, along with long-wavelength zonal flows were enhanced when insulating boundaries were applied. In addition, drift wave turbulence, and long-wavelength zonal flows were suppressed when conducting boundaries were applied. Drift waves drive zonal flows via the turbulent Reynold's stress in the plasma. [10] Figure 2-15 clearly shows an extreme change in the Reynold's stress based upon the choice of insulating or conducting boundary.

Recently on the Large Helical Device (LHD), Inagaki, et al. discovered low frequency electron temperature fluctuations with a long correlation length relative to the device radius, coupled with microscale fluctuations. These fluctuations were characterized by frequencies in the low kilohertz, amplitudes of $\leq 2\%$, and 1/1 or 2/1 mode

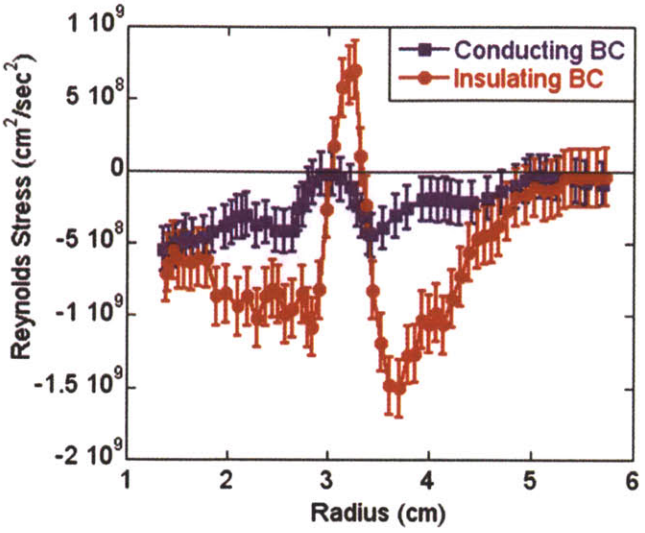

Figure 2-15: Radial profiles of Reynold's stress for conducting boundary conditions (blue) and insulating boundary conditions (red). (Thakur, et al. [10])

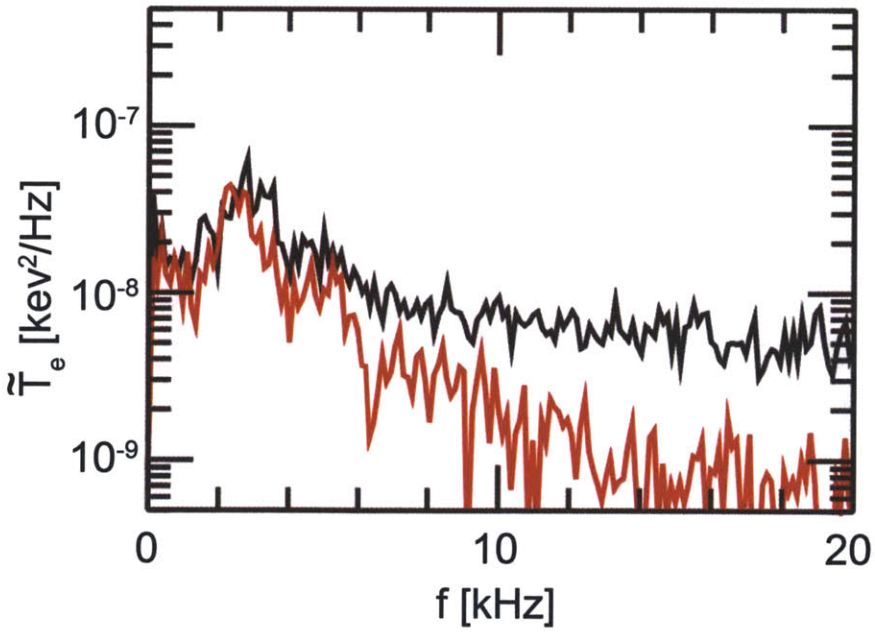

Figure 2-16: Fourier spectrum from ECE on LHD: Autopower spectrum (black) and cross-power spectrum (red); note the peak at 2.5 kHz, with a bandwidth of approximately 1 kHz (Inagaki, et al. [11])

numbers. Figure 2-16 clearly shows a peak in the autopower spectrum (black) and the cross-power spectrum (red) at 2.5 kHz, with a bandwidth of approximately 1

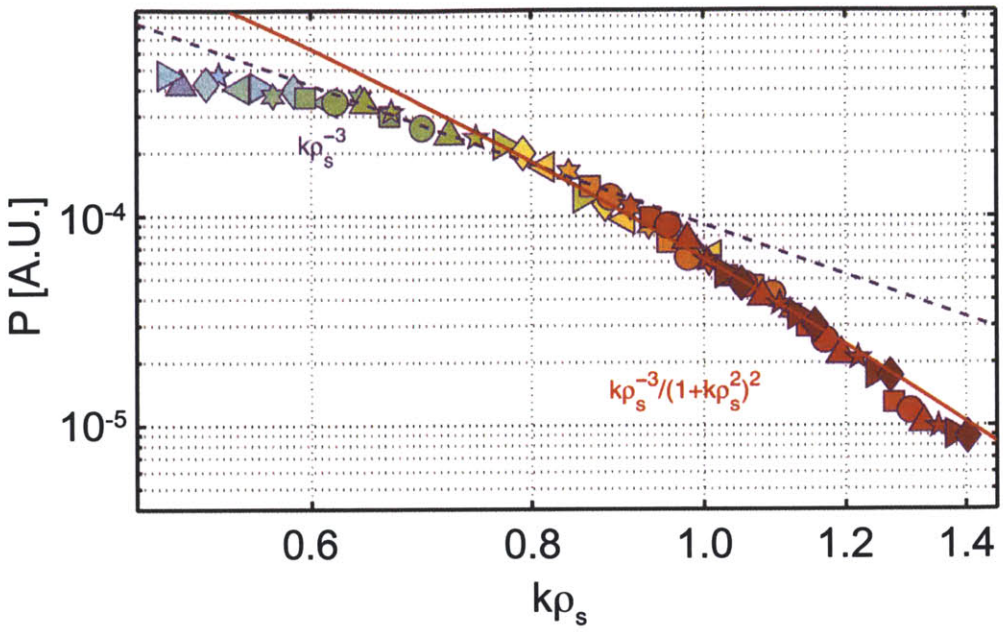

Figure 2-17: Experimental wavenumber spectrum of density fluctuations on Tore Supra, compared with power law $(k\rho_s)^{-3}$ (blue) and shell model $(k\rho_s)^{-3}/(1+(k\rho_s)^2)^2$ (red). (Vermare, et al. [12])

kHz. The characterization was accomplished using correlation techniques with reflectometry, probes, and electron cyclotron emission (ECE) measurements. This result contributes to the understanding of fundamental processes related to rapid change in transport between two distant, but connected, regions of inhomogeneous plasma. [11]

One relatively new technique for measuring turbulence has been applied on Tore Supra with good results. Vermare, et al. implemented a Doppler backscattering system on Tore Supra. [12] This system combines merits of both reflectometry and light scattering systems. The Doppler backscattering system detects the field scattered off density fluctuations near the cut-off layer. The system provides instant spatial Fourier analysis of the fluctuations in the plasma. In addition, a simple shell model for homogeneous, isotropic turbulence was developed, to compare with measurements for large $k\rho_s$, where ρ_s is the effective ion Larmor radius. The spectrum:

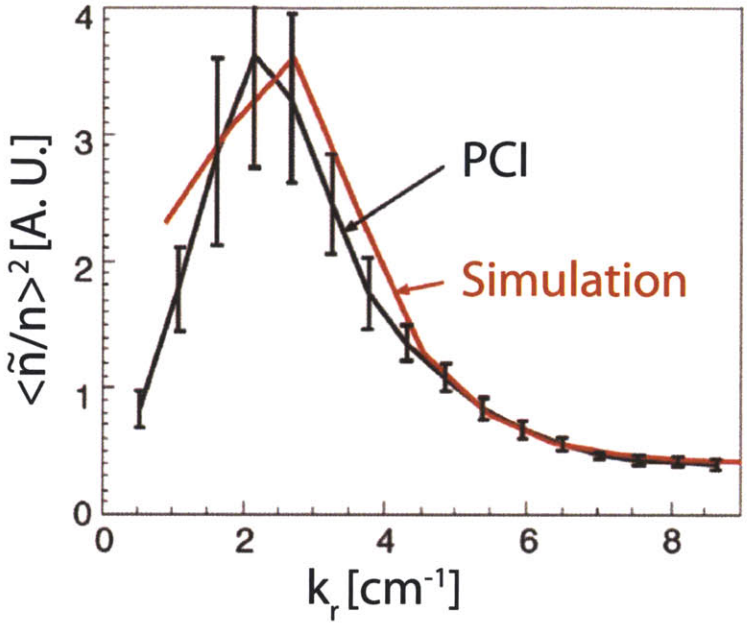

Figure 2-18: Density fluctuation vs radial wavenumber spectrum on Alcator C-Mod. PCI data are shown in black; gyrokinetic simulation results are shown in red. (Ernst, et al. [13])

$$|\phi_k|^2 \sim \frac{(k\rho_s)^{-3}}{(1+(k\rho_s)^2)^2}, \tag{2.52}$$

fits the data quite well for large $k\rho_s$ in Fig. 2-17. For the central wavenumbers in Fig. 2-17, the data obey a simple power law $(k\rho_s)^{-3}$, and for small wavenumber saturation occurs. [12]

Fine scale electron temperature gradient turbulence (ETG) has been observed on numerous tokamaks with very different topologies and plasma characteristics, including DIII-D, NSTX, and FT-2. [65] Each of these experiments showed a dramatic growth of ETG turbulence once the theoretical ETG mode threshold was exceeded. Additionally, strong rotation shear effectively suppresses this small-scale turbulence, contradictory with theory. [65] However, while the correlation of ETG turbulence and anomalous transport has been established, it has not been proven that the ETG mode is directly causing the enhanced transport, or is merely a parallel effect. [65]

On Alcator C-Mod, measurements of the trapped electron mode (TEM) insta-

bility have been made using the phase contrast imaging (PCI) diagnostic. The PCI measurements of density fluctuations were made in a region of the plasma where the primary linear instability was TEM. Good agreement was found between these data, shown in Fig. 2-18, and nonlinear gyrokinetic simulations of TEM fluctuations in the core of Alcator C-Mod. [13] [66]

2.2.2 Scrape-Off Layer Instabilities

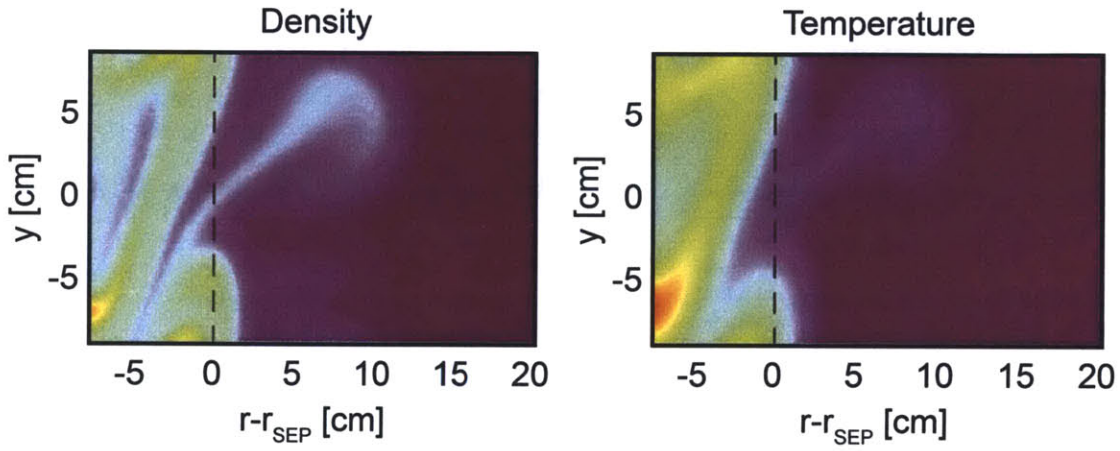

Figure 2-19: Simulated density and temperature of a plasma filament erupting through the separatrix during a simulation of a MAST plasma. (Militello, et al. [14])

The edge of a tokamak plasma is important to any conceivable tokamak fusion reactor design, because the Scrape-Off Layer (SOL) governs the exhaust of particles and energy. Therefore, it is extremely important to quantify the physical mechanisms responsible for transport in the edge. The edge region of a tokamak is a relatively cold ($\sim$ 50 eV), low density ($\sim 10^{17}$ m^{-3}), plasma with nonlinear fluctuations, open magnetic field lines, and non-adiabatic electrons. [14] Experimental observations on numerous tokamaks have revealed these edge plasmas to be very turbulent with large fluctuations and filament-like structures, called "blobs". [67]

Edge relative fluctuations in density, temperature, potential, and magnetic field typically increase in magnitude radially from the last closed flux surface (LCFS) into

the scrape-off layer (SOL). These broadband fluctuations generally occur between 10 kHz and 1 MHz and exhibit an autocorrelation time of $2 - 20\mu s$. [68] Additionally, the SOL turbulence has a relatively short (0.1-10 cm) spatial scale across the magnetic field, but quite long (1 m) parallel to B. [68] Interestingly, radial transport in the edge region is strongly poloidally asymetric. As a result most tokamaks exhibit a low field side pressure peak. [68]

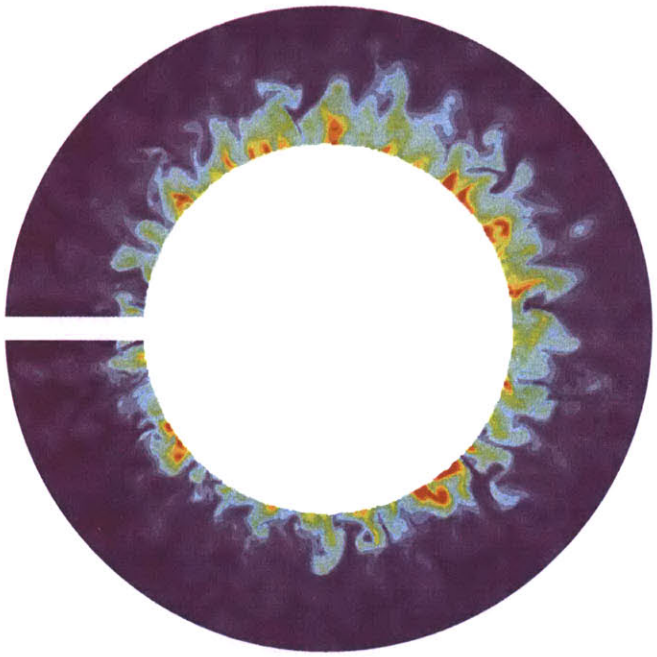

Figure 2-20: Poloidal cross section of tokamak scrape-off layer turbulent electron pressure p_e. (Ricci, et al. [15])

Recently, Militello, et al., [14] compared simulations using the Edge-Sol ELectrostatic (ESEL) code with experimental observations on the MAST spherical torus with good results. The ESEL code is a 2D drift–fluid equation model. They found that the simulations reproduce the filament bursts observed on MAST, but neglect small time scale fluctuations. The power spectrum of the burst events was seen to peak at around 10 kHz, giving a time scale of 100 μs. Figure 2-19 shows a simulation of a plasma filament erupting through the separatrix during a simulation of a MAST plasma. These structures are found to be constantly present when the turbulence has reached steady state. [14]

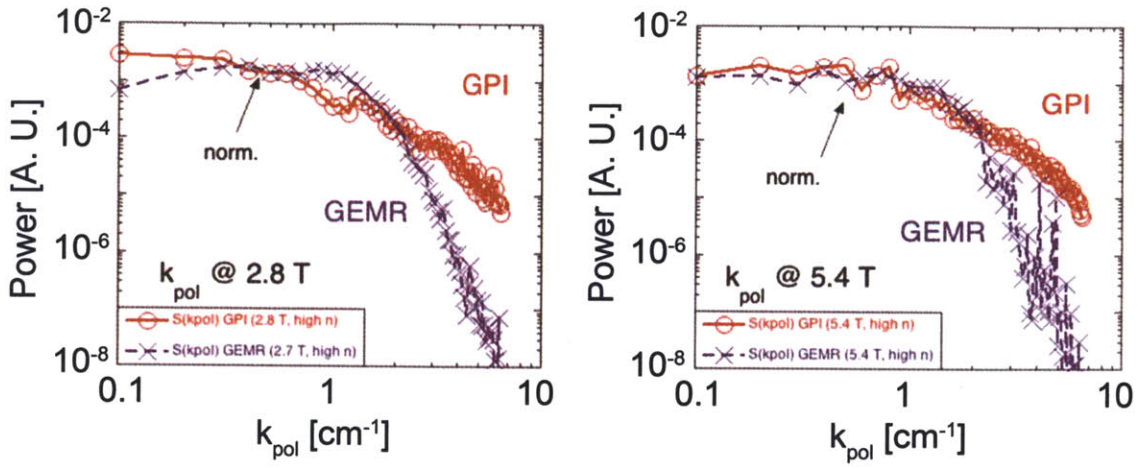

Figure 2-21: Comparison of Alcator C-Mod poloidal spectra for experimental (GPI) and computational (GEMR) results for $B_0 = 2.8$ T and $B_0 = 5.4$ T. (Zweben, et al. [16])

Another excellent simulation example of scrape-off layer turbulence is shown in Fig. 2-20 from Ricci, et al. [15] Here, filament, or radial blob structures are clearly visible in the fluctuating electron pressure. For these simulations, turbulence is driven primarily by resistive ballooning modes and drift waves. [15]

Fluctuations in the plasma potential in the SOL are difficult to quantify. Recently, Bisai, et al., conducted a series of SOL simulations, which showed that plasma turbulence changed when the ion energy equation was included. In simulations where ion temperature was included in the model, the floating temperature decreased by approximately 1/6, and additionally, the radial electric field was also reduced. The study found an angular velocity of 1.5×10^5 rad/s for plasma blobs. In addition, in regions with large ∇T_e, the blobs can establish charge separation radially. [69] Using Langmuir probes on ASDEX Upgrade, Nold, et al. found evidence that temperature fluctuations strongly influenced measurements of floating potential. This has important implications for $\mathbf{E} \times \mathbf{B}$ convection and turbulence in the edge of tokamak plasmas. [70]

Further evidence of fluctuation induced cross-field transport in the SOL is found on Alcator C-Mod. [71] [72] [73] [74] Alcator C-Mod provides access to scrape-off layer data for high density, high magnetic field plasma discharges. Gas puff imaging

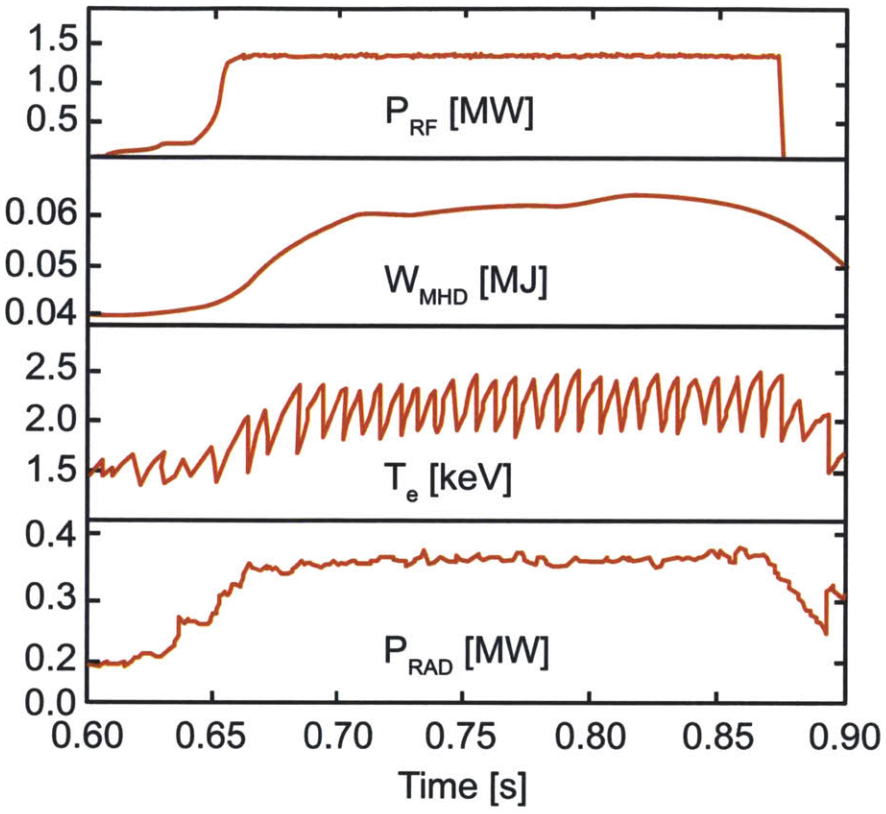

Figure 2-22: Effect of ICRF heating on plasma parameters for a typical low confinement mode discharge on Alcator C-Mod.

(GPI) is used to investigate poloidal flows and turbulent structures in the SOL. [73] Zweben, et al. [16], compared edge turbulence measurements made with GPI and simulation results from the GEMR code. This local turbulence code employs a 3D gyrofluid approximation and uses 2D toroidal geometry. [16]

Figure 2-21 shows good agreement between poloidal wavenumber spectra for the GPI measurements and the GEMR simulation results for both high (5.4 T) and low (2.8 T) magnetic fields. Here, the measurements and simulation results indicate wavenumber spectra $k_{\mathrm{pol}}\rho_{\mathrm{s}} \ll 1$, which corresponds to typical tokamak edge turbulence measurements.

One particularly interesting aspect of SOL/edge turbulence is the correlation of poloidal flows and $E \times B$ convection in the edge with the application of RF power. On Alcator C-Mod, Ion cyclotron range of frequencies (ICRF) heating is very effective

at transferring energy into the plasma through wave particle resonances. Fig. 2-22 shows the effect of ICRF on several plasma parameters during a typical discharge on Alcator C-Mod. When ICRF is turned on, the plasma stored energy W_{MHD}, central electron temperature T_{e0}, and radiated power P_{RAD}, increase significantly. [75]

One problem that is universally observed on tokamaks [76], including Alcator C-Mod [75], is an increase in impurities during ICRF operation. In ITER and in eventual reactors, enhanced impurity confinement establishes a very low tolerance for high-Z impurities [77]. High-Z impurities can cause significant radiation losses from the plasma, as well as dilution of the fuel. As a result, one of the primary challenges of ICRF heating is the reduction or elimination of impurities introduced into the plasma during ICRF operation, particularly for tokamaks with high-Z PFCs. One of the primary mechanisms thought to be responsible for increased impurity characteristics during ICRF heated plasma discharges is turbulence in the edge. Various mitigation strategies have been proposed, including a magnetic field-aligned antenna. [78] However, transport driven impurities continue to be a problem. Strong time-varying electric fields generate RF-enhanced sheaths, which create $E \times B$ convective cells, driving flows and turbulence in the edge.

As shown in Fig. 2-23 the poloidal flows in both the ion diamagnetic direction (IDD) and electron diamagnetic direction (EDD) change drastically. In addition, the velocity has several zero crossings in the region immediately outside the last closed flux surface (LCFS).

Before we transition to a discussion of turbulent transport in Hall thrusters, it is important to emphasize that tokamaks are not alone in observations of turbulent plasma structures. As mentioned previously, stellarators, linear devices and plasma sources also provide evidence for turbulent cross-field transport. [79] [80] [81]

Observations on the large plasma device (LAPD) reveal periodic density perturbations, which are consistent with interchange-like modes. [82] Here, "blobs" of higher than average density and "holes" of lower than average density fluctuate at the edge of the plasma. The intermittency of these structures is found to be very similar to that observed in tokamaks. [74] [72] [82] In addition, Antar, et al. found that the

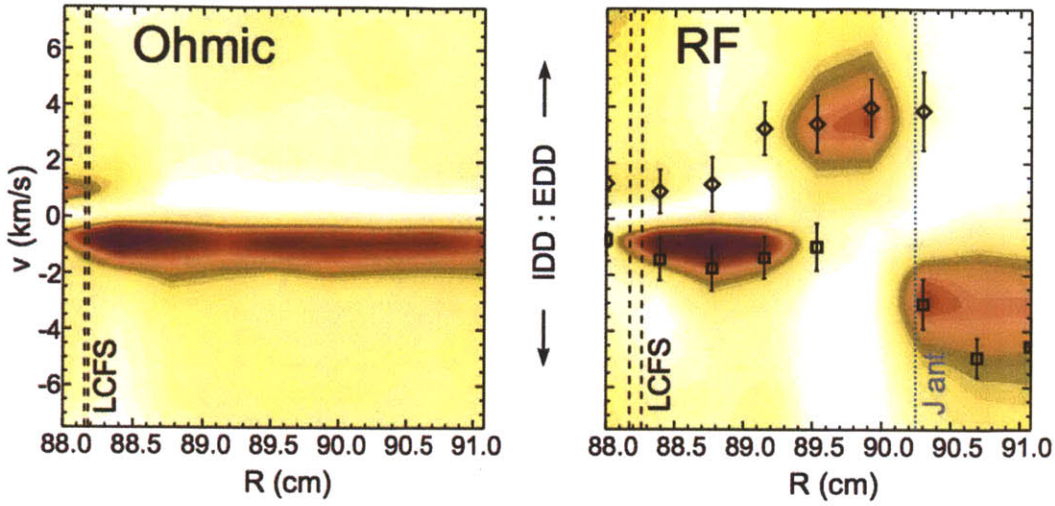

Figure 2-23: Plots of poloidal velocity distribution $D(R, v_\theta)$ from an ohmic SOL and from a SOL heated by an ICRF antenna on Alcator C-Mod. The blue dashed line represents the radius of the front face of the antenna. Diamonds represent velocities for $k_\theta > 0$, squares for $k_\theta < 0$. (Cziegler, et al. [17])

intermittency of these structures was periodic in nature. [83] In Fig. 2-24 2D simulation results of SOL turbulence reveal the filament like structure of radial extended convection cells, and their suppression by higher levels of radial electric field shear. Additionally, Holland, et al. found an azimuthally symmetric, radially sheared flow formed spontaneously in a cylindrical helicon plasma device. [84] Here, the authors found that the sheared flow was created from Reynolds stress from drift turbulence in the plasma.

As mentioned above, quadratic nonlinearities manifest through a three wave coupling, with two waves beating to drive a third, $\mathbf{k}_0 + \mathbf{k}_1 + \mathbf{k}_2 = 0$. One method to quantify the coherence among different modes is to look at the autobispectrum:

$$B_{k_0}(k_1, k_2) = \langle \phi_{k_0} \phi_{k_1} \phi_{k_2} \rangle, \tag{2.53}$$

and the squared bicoherence:

$$b^2_{k_0}(k_1, k_2) = \frac{|B_{k_0}(k_1, k_2)|^2}{|\langle \phi_{k_0} \rangle|^2 |\langle \phi_{k_1} \phi_{k_2} \rangle|^2}. \tag{2.54}$$

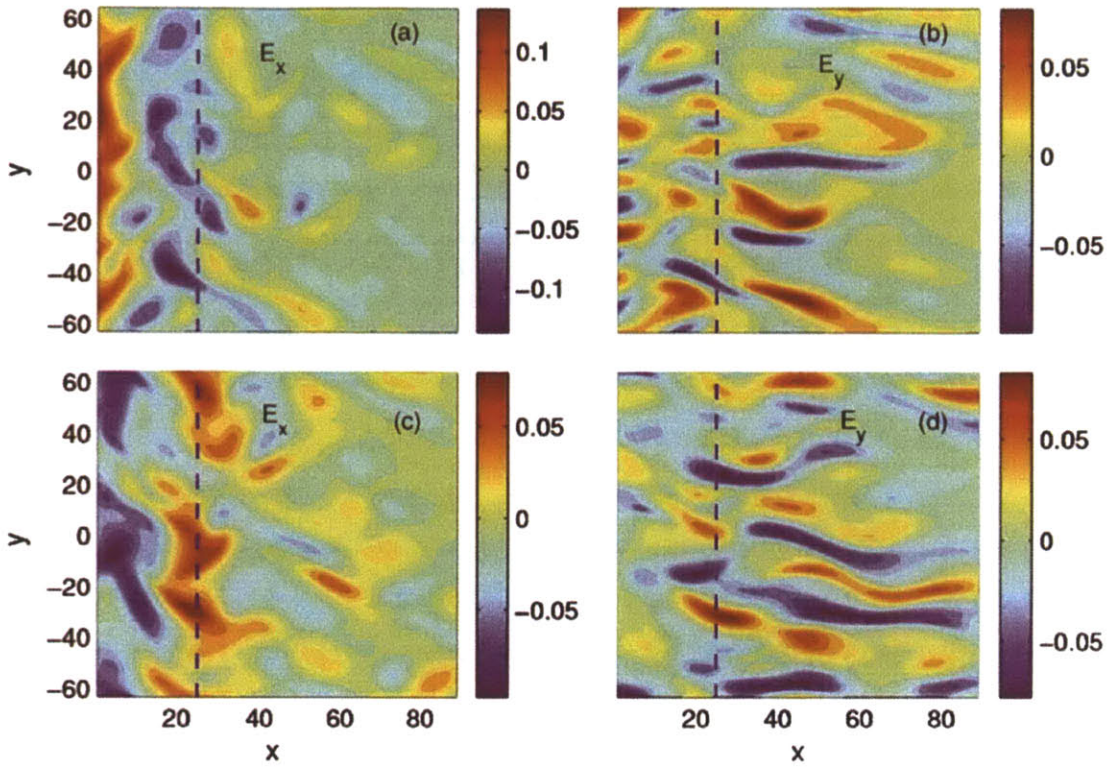

Figure 2-24: Plots of electric field components at one time point from 2D SOL simulations. Here E_x corresponds to the radial electric field and E_y corresponds to the poloidal electric field. Higher relative values of radial electric field shear are implemented in a) and b) than in c) and d). (Bisai, et al. [18])

On the controlled shear decorrelation experiment (CSDX), Burin, et al. [19] investigated the correlation of fluctuations in a magnetized plasma column. Figure 2-25 shows squared bicoherence (Eq. 2.54) of density fluctuations for six different magnetic field strengths. Note that at different field strengths, correlations between different frequency fluctuations appear and disappear.

There are numerous turbulent phenomena in tokamak plasmas, which involve both electrons and ions, and manifest through complicated nonlinear wave interactions. In the following chapter we will continue to explore the physics of plasma turbulence and the effects of externally applied electric fields on turbulent transport. More specifically, the fluctuations, instabilities and turbulent cross field transport in Hall thrusters will be investigated.

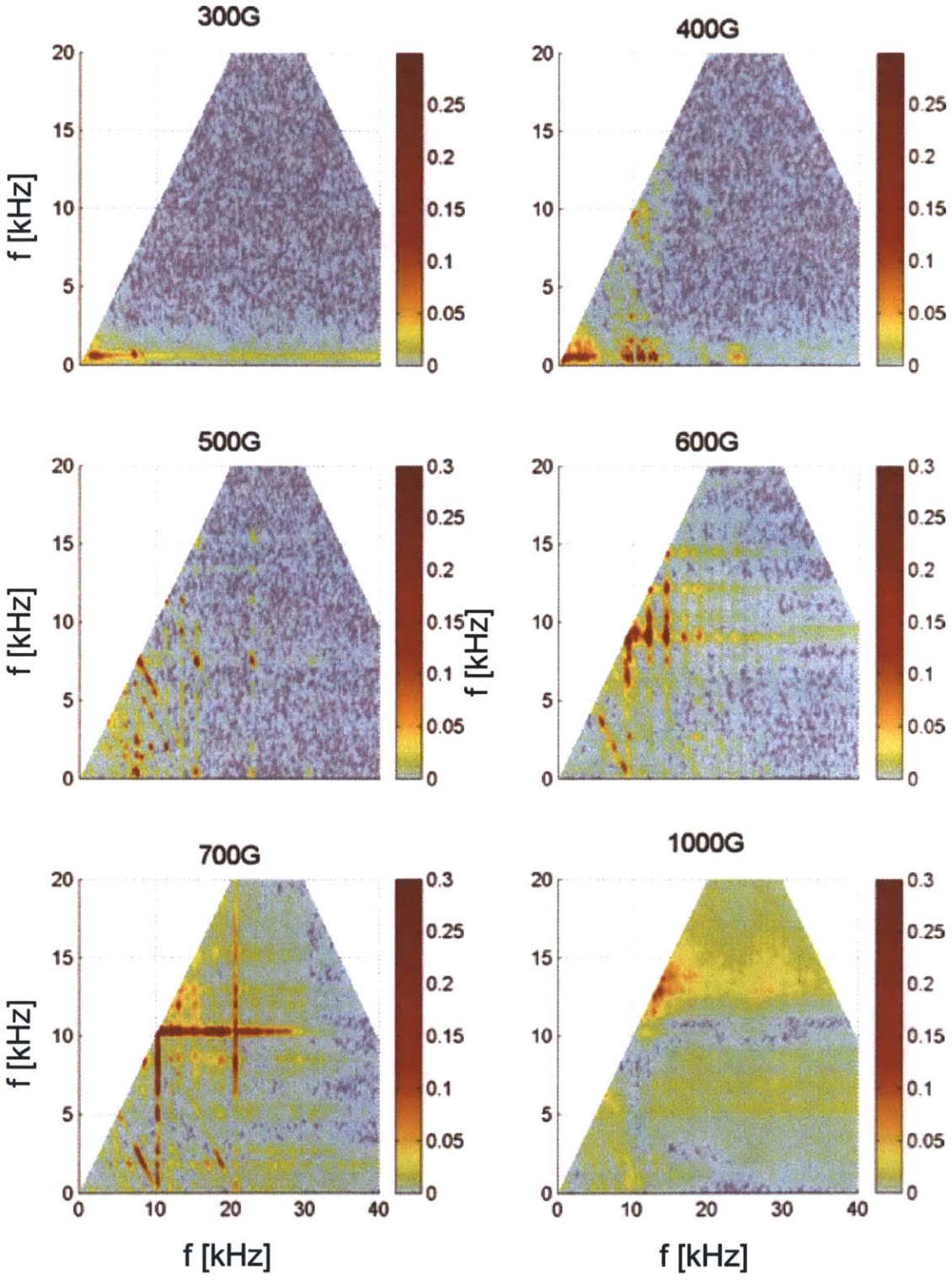

Figure 2-25: Plots of squared bicoherence (Eq. 2.54) of density fluctuations for six different magnetic field strengths. (Burin, et al. [19])

Chapter 3

Hall Thruster Fluctuations

3.1 Observed instabilities

Similar to edge turbulence in a tokamak, characterized by broadband density and temperature fluctuations with amplitude $\delta n/n \sim \delta T/T \approx 0.05 - 1.0$, Hall thruster oscillations occur at frequencies of several kHz to several MHz. Generally, Hall thruster instabilities are grouped into three primary frequency ranges: 1–50 kHz, 100–700 kHz, and 1–80 MHz. These frequency ranges are labeled region I–III in Fig. 3-1. The first range is generally connected to ionization in the discharge channel. This low frequency range contains two prominent and distinct instabilities referred to as the "breathing mode" and "rotating spoke" instability. At higher frequencies ($\sim$ MHz) this mode transitions into a separate branch often called a "streamer" instability. These instabilities, particularly the low frequency modes, are implicated as contributing to anomalous electron transport in Hall thrusters. The middle frequency range generally pertains to ion motion and transit time oscillations. These fluctuations are largely turbulent and are thought to be necessary for turbulence driven electron diffusion at larger magnetic field strengths. [20] Finally, the high-frequency range generally pertains to electron drift motion, where waves propagate in the plane normal to the radial magnetic field. This frequency range is also implicated in anomalous cross-field electron transport. [85]

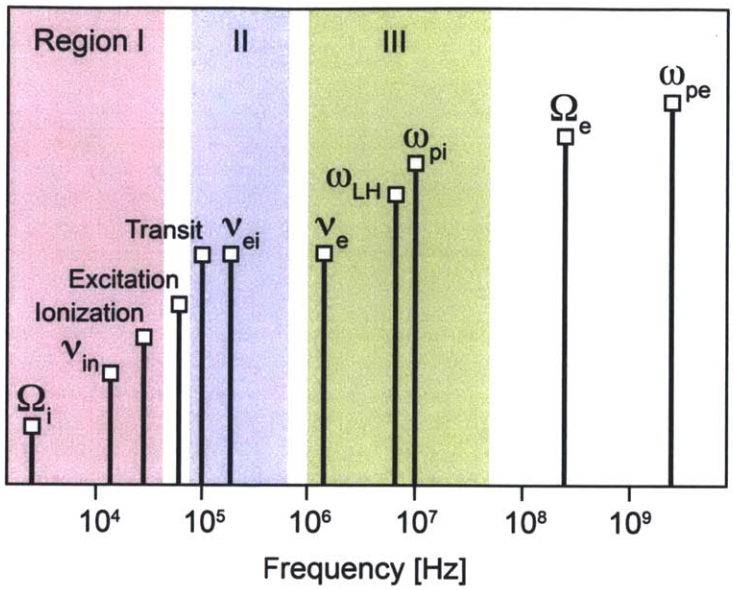

Figure 3-1: Frequency map for relevant Hall thruster collision, cyclotron, plasma, ionization, and transit time frequencies. Region I includes breathing and rotating spoke modes. Region II includes transit-time axial modes. Region III includes high frequency azimuthal modes. Adapted from [20]

3.1.1 Breathing mode

There are many different fluctuations present in Hall thruster plasmas. Many distinct length and time scales exist among these fluctuations. There are current density, temperature, and potential fluctuations, spanning a broad range of frequencies from several kilohertz to over a gigahertz. These oscillations have been shown to play a role in ionization, particle diffusion and acceleration processes. One ubiquitous type of fluctuation at the lower end of the frequency spectrum, in the range 10–30 kHz, has earned the name "breathing oscillations". Fluctuations corresponding to this frequency range are shown in the middle of Fig. 3-2, above. These oscillations are interesting for several reasons. One, they carry a large part of the power in the annular plasma. These breathing oscillations have been described as a type of predator–prey mechanism between neutrals and ions. [86] The oscillations are a function of a periodic depletion and replenishment of the neutrals near the thruster exit plane. This mechanism occurs due to the efficient ionization of the gas in this

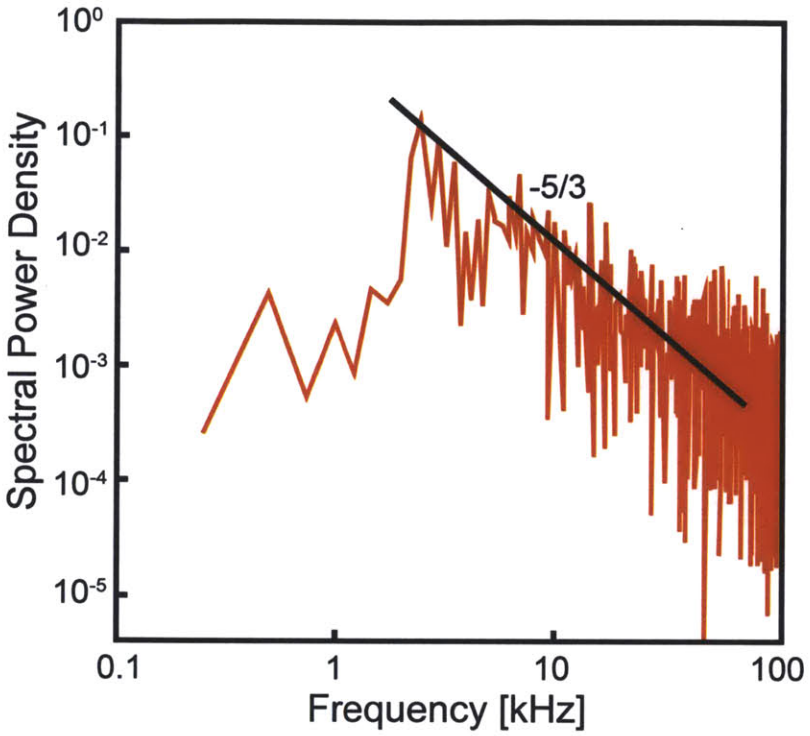

Figure 3-2: Demarco, et al., measured spectral power density in the discharge of a Hall thruster. Note the -5/3 power law dependence. [21]

region. The oscillation frequency of the mode is set by the amount of time it takes the neutral species to fill in the ionization region once the previous group has been ionized and accelerated. [20]

In a typical Hall thruster, neutral thermal speeds are of order $\sim$ 300 m/s. The ionization region being depleted is of order $\sim$ 2 cm, yielding an oscillation frequency of $\sim$ 15 kHz. This oscillation mode causes the discharge current to fluctuate, and causes fluctuations in density, temperature, ion energy and thruster ion beam divergence. These oscillations are thought to involve a temporal variation of the plasma potential in the acceleration channel, effectively causing the accelerating electric field to oscillate. The plasma is essentially collisionless within the acceleration layer. Recently, Mazouffre used laser induced florescence measurements of the time-varying ion velocity to quantify oscillations of this electric field.[87]

Numerical models have had reasonable success predicting the periodic structure

of these breathing modes. The origins of this low frequency oscillation have been attributed to the large magnetic field at the exit plane of the thruster. [88] The large radial magnetic field results in a low axial electron conductivity. This, in turn, produces an increase in the axial electric field in order to maintain continuity. Very close to the thruster exit there is a region of significant ionization where, as the ions created are rapidly accelerated away, the neutral density plummets. As this occurs, the neutral–ion transition moves away from the thruster exit toward a region with lower ionization. Finally, the neutral–ion transition begins to move back in the direction of the exit because the ionization rate is lower toward the back of the thruster. [88]

3.1.2 Low frequency azimuthal density fluctuations

Azimuthal density fluctuations in Hall thrusters were connected with anomalous electron transport as early as 1966 [22]. Janes and Lowder measured an azimuthal propagating structure in the electron density and observed that the fluctuation moved in the $E \times B$ direction with a velocity of approximately $E_x/5B_r$. These azimuthal fluctuations, known as rotating "spokes" have been observed on most Hall thruster experiments and have also been observed recently in cylindrical Hall thrusters (CHTs). These spokes have higher density than the surrounding plasma and undergo charge separation due to the azimuthal $E_x \times B_r$ drift of electrons. This charge separation produces an azimuthal electric field, E_θ, which contributes to an axial $E_\theta \times B_r$ drift of electrons. One instance of the rotating spoke mode on a CHT is shown in Fig. 3-5. Using fast framing cameras and electrostatic probes, Parker, et al., measured $\sim$ 20 kHz oscillations, revealing a rotation speed of $\sim$ 2 km/s, approximately 1/15 of the E_x/B_r velocity of 30 km/s. [89]

Notably, as the electron current from the cathode was increased, the rotating spoke oscillation was replaced by a higher frequency fluctuation. At this transition, the ratio of the discharge current to the beam current decreased, indicating a decrease in the cross-field electron transport. This supports the theory that the rotating spoke enhances the cross-field transport.

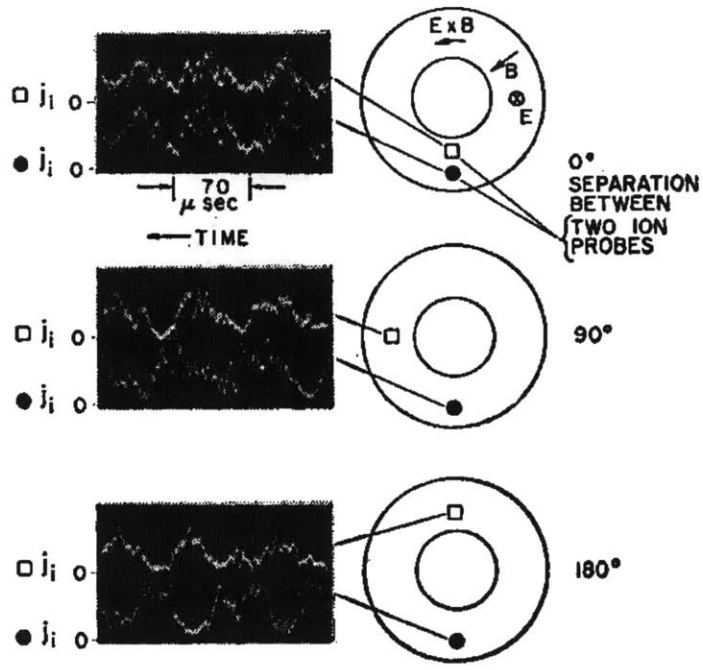

Figure 3-3: Janes and Lowder measurements of azimuthal density fluctuations in the annular region of a Hall thruster. Data were taken with two negatively biased Langmuir probes. The correlation of the phase angle of the measurements and the location of measurements suggests a single rotating density fluctuation. [22]

Ellison, et al., measured the cross-field current induced by the spoke directly for the first time using a special a segmented anode. [24] In the majority of Hall thruster experiments, discharge current oscillations are monitored. However, the anode structure in these devices is a continuous annular ring and thus can only provide information about longitudinal modes, such as the breathing mode described previously. In this work, the authors divided the anode into four quadrants so that the current through the spoke could be measured as a function of azimuthal position. The cross-field current can be determined by using a fast framing camera, synchronized with the anode quadrant current measurements and a set of electrostatic probes. Here, over half of the total current flows through the rotating spoke, which occupies only one-quarter of the area of the annular channel. The spoke current is shown to be equal to the axial electron current. [24]

Analysis of the rotating spoke instability is complicated by the fact that the breathing mode typically occurs in a similar frequency band: $\sim 10 - 20$ kHz. This

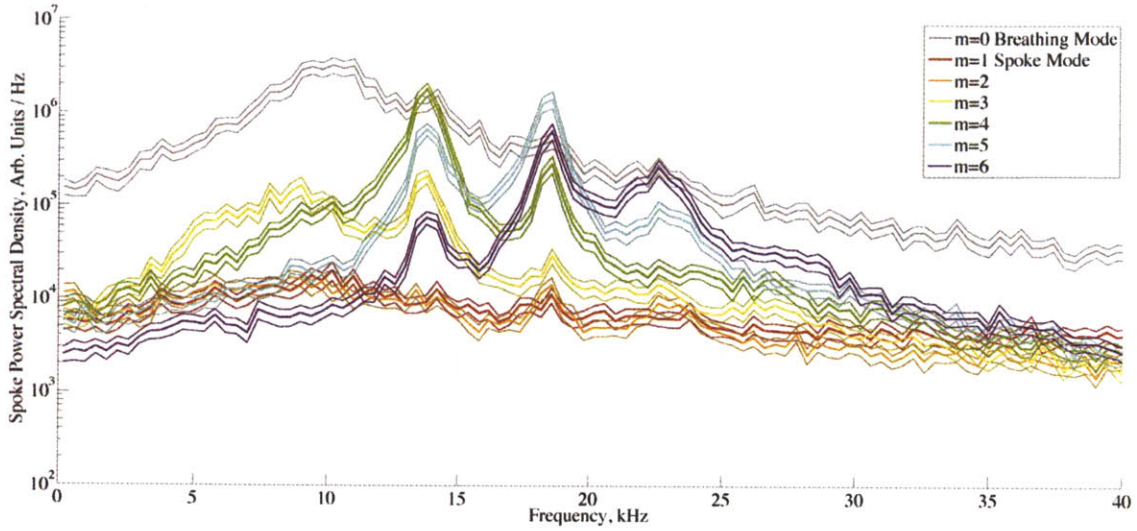

Figure 3-4: McDonald, et al., found multiple modes m=1 to m=6 for the rotating spoke instability. The breathing mode is also shown, peaked at approximately 10 kHz. [23]

can be seen in Fig. 3-4, where in addition to the breathing mode, six distinct rotating spoke modes are plotted with their respective harmonics. As mentioned previously, enhanced cathode current can suppress breathing mode oscillations. However, too much cathode current promotes a transition into a higher frequency mode, where the spoke instability is suppressed. Ellison found that, for the CHT, a 1.5 A cathode keeper current was sufficient to suppress the breathing mode and avoid high frequency oscillations so that the physics of the spoke oscillation could be studied. [24]

Figure 3-6 shows normalized measurements of density, temperature, potential and spoke current (the current flowing through the spoke region), as a function of the rotating spoke phase. Here, the density peaks almost simultaneously with the current at $\sim 3 \times 10^{18}$ m^{-3}. The temperature fluctuates between 2 eV and 7 eV and the potential fluctuates between 200 V and 230 V. [24] As indicated in the figure, both temperature and potential are shifted approximately 135° from the spoke phase. The potential is not completely out of phase with the spoke, and so can produce a net current to the anode. The phase of the potential gives rise to an azimuthal electric field:

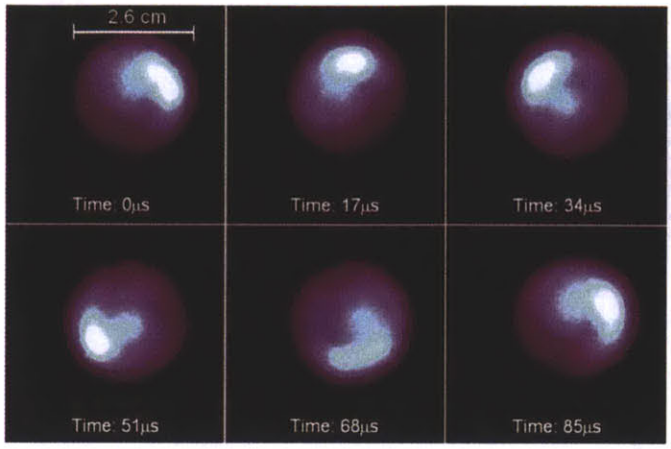

Figure 3-5: Ellison, et al., measured light (visible) emission from a cylindrical Hall thruster. Here the spoke rotates counter-clockwise, in the $E \times B$ direction at $\sim$ 20 kHz. [24]

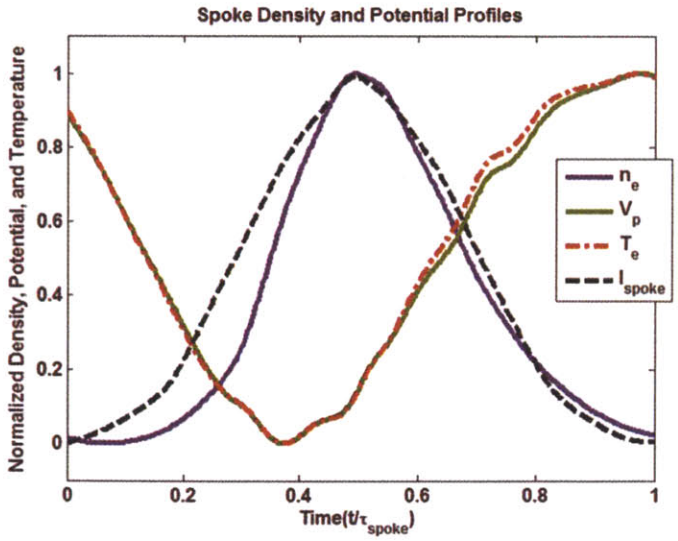

Figure 3-6: Ellison, et al., normalized density, temperature, potential and spoke current as a function of spoke phase. [24]

$$E_\theta = -\frac{dV_\mathrm{p}}{d\theta} = -\frac{dV_\mathrm{p}}{dt}\frac{dt}{d\theta} = -\frac{1}{v_\mathrm{spoke}}\frac{dV_\mathrm{p}}{dt}, \tag{3.1}$$

which combined with the radial magnetic field, leads to an axial drift of electrons toward the anode, given by $v_\mathrm{drift} = E_\theta / B_\mathrm{r}$. The net drift current, as the spoke passed across the segmented anode was estimated as:

$$I_\mathrm{drift} = e v_\mathrm{d} n_\mathrm{e} A_\mathrm{s}. \tag{3.2}$$

Here, the drift current peaks at 0.67 A, which is within the error bars for the amplitude of the spoke current, 0.48 A. The authors suggest that this implicates the macroscopic fluctuations of density, temperature and potential as the source of the spoke current, as opposed to micro-turbulence within the spoke. [24] However, microturbulence may play a role in the onset of the rotating spoke, as well as explaining discrepancies between the measured currents. One of these discrepancies is that the spoke current and the drift current are not in phase. In addition, there is a high frequency oscillation seen on both the electric field and on the drift current, which is not present on the spoke current. The origin of the rotating spoke is still not understood and there is no clear reason why an $m = 1$ mode should exist over others. Additionally, the slow rotation speed $\sim E/5B$ to $\sim E/10B$ is not understood. Some authors [22] have suggested that the slow speed is related to the critical ionization velocity, but this has not been confirmed. There is also the possibility that the fluctuation may be ionization related in terms of a type of azimuthal "breathing" mode. The idea here is that an ionization front propagates azimuthally in the thruster annulus and conducts electrons axially.

3.1.3 Mid-range axial transit time oscillations

Between 70 kHz and 500 kHz, numerous "transit time" oscillations are present in Hall thrusters. Fluctuations in this frequency range are primarily turbulent. However, they sometimes contain some deterministic space and time correlations. These oscillations are thought to be necessary for turbulence driven diffusion at large mag-

netic fields to account for anomalous transport beyond that predicted by classical theory. [20]

These turbulent fluctuations are called "transit time" oscillations because this frequency range roughly corresponds to the ion-channel residence time scale:

$$\omega \approx \frac{u_{\mathrm{i}}}{L}. \tag{3.3}$$

More specifically, Choueiri [20] gives the following definition for the frequency of this axial mode. Here, the axial coordinate is along $\hat{\mathrm{x}}$. We can define a characteristic gradient length of a parameter α as:

$$L_{\nabla\alpha} = \left|\frac{\alpha}{\partial\alpha/\partial x}\right| = \left|\frac{\partial \ln \alpha}{\partial x}\right|^{-1}. \tag{3.4}$$

The electron drift velocities in the $\hat{\mathrm{x}}$ and $\hat{\mathrm{y}}$ directions are given by:

$$u_{\mathrm{x}} = -D_{\mathrm{e}\perp}\frac{\partial\left(n_{\mathrm{e}}kT_{\mathrm{e}}\right)}{n_{\mathrm{e}}\partial x} - \mu_{\mathrm{e}\perp}E_{\mathrm{x}}, \tag{3.5}$$

and $u_{\mathrm{y}} = \beta u_{\mathrm{x}}$, $\beta = \omega_{\mathrm{ce}}/\nu_{\mathrm{e}}$, and the cross-field electron mobility and diffusion coefficients are given by:

$$\mu_{\mathrm{e}\perp} = \frac{|e|}{m_{\mathrm{e}}\nu_{\mathrm{e}}\left(1+\beta^2\right)}, \tag{3.6}$$

and

$$D_{\mathrm{e}\perp} = \frac{kT_{\mathrm{e}}}{m_{\mathrm{e}}\nu_{\mathrm{e}}\left(1+\beta^2\right)}. \tag{3.7}$$

The real component of the frequency is given by:

$$\omega \simeq k_{\mathrm{x}}u_{\mathrm{i}}\frac{b}{b+1}, \tag{3.8}$$

and the growth rate by: [90]

$$\gamma \simeq k_{\mathrm{x}}u_{\mathrm{i}}\frac{\sqrt{b}}{b+1}, \tag{3.9}$$

where, for $k_y^2 \ll k_x^2$, $b \equiv u_B/|u_y|$ and the magnetic drift velocity, u_B is given by:

$$u_B = \frac{u_i^2}{\omega_{ci} L_{\nabla B}}. \tag{3.10}$$

Here, $k_y^2 \ll k_x^2$ implies a near axial propagating wave.

Physically, these waves can be thought of as coupling the so-called "beam mode" $k_x u_i$ to plasma oscillations driven by inhomogeneity within the thruster channel. The behavior of these mid-range fluctuations was found to agree reasonably well with experimental data. [90] Linear theory of gradient driven sound waves predicts most of the characteristics of this class of axial fluctuations. These oscillations are electrostatic waves, which propagate axially in the thruster channel. The waves are also relatively broadband and have turbulent characteristics. This class of waves may play an important role in anomalous cross-field transport in Hall thrusters.[20]

3.1.4 High frequency azimuthal fluctuations

High frequency azimuthal waves are thought to be associated with anomalous electron transport. [85] These azimuthal waves induce axial electron fluctuations ($E_\theta \times B_r$) when the wave frequency is lower than the electron cyclotron frequency. Tomilin, et al., used a linear two-fluid model to look at the stability criterion for high frequency azimuthal waves in Hall thrusters. [85] Here, they found that the most unstable oscillations were purely azimuthal waves, which had relatively small wave numbers. They also found that the instability growth rate decreases when the plasma inhomogeneity decreases or when the wave number increases. [85]

As mentioned above, the inhomogeneous plasma (with gradients and fluctuations in density, temperature and potential) inside a Hall thruster is not in thermodynamic equilibrium. The equilibrium $E \times B$ electron drift functions as a source of numerous instabilities. Of the many different types of instabilities, the Lower hybrid instability and modified two-stream instability of Hall plasma with transverse currents are regarded as quite important. [25]

The Lower hybrid instability is characterized by a relatively short wavelength

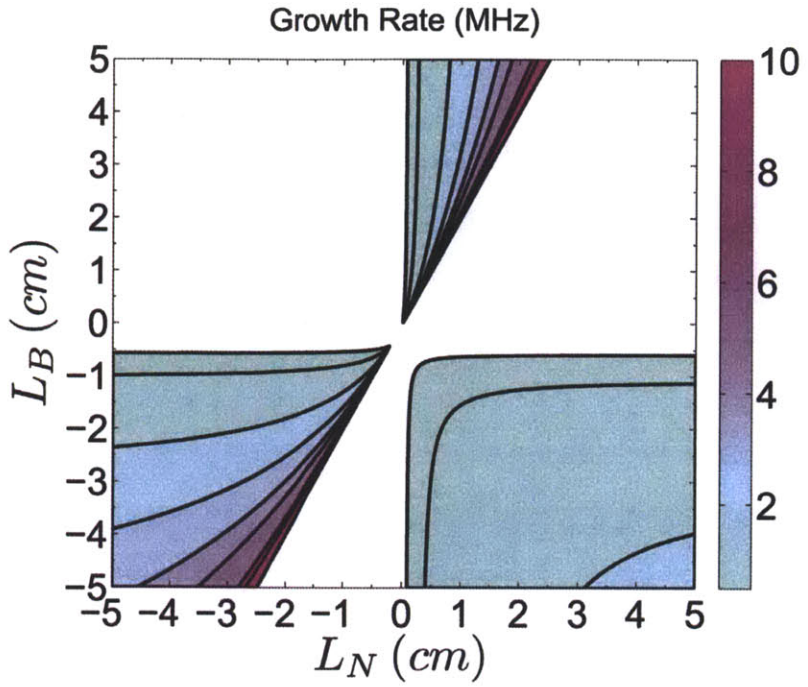

Figure 3-7: Frias, et al., contour plot of azimuthal instability growth rate as a function of the magnetic field and density gradient scale lengths. [25]

with $k_\perp \rho_e \simeq 1$. This is a variant of more general beam cyclotron instabilities with additional higher cyclotron harmonics. [91] In some cases, where transverse currents in the discharge region drive the nonlinear portion of the Lower hybrid mode, these fluctuations can saturate at small amplitudes because of ion trapping. The modified two stream instability is most unstable for $k_\perp \rho_e < 1$. This fluctuation must have a finite component of the wave parallel to the magnetic field. [25] In a study of high frequency azimuthal fluctuations in Hall thrusters, Frias, et al., mapped the growth rate as a function of the gradient scale lengths of the magnetic field and density (shown in Fig. 3-7). [25] Here, typical Hall thruster parameters were used and gradient scale lengths were chosen to be of order the thruster channel length ~ 2 cm. The instability growth rate is in the MHz range and increases as we move toward the marginal boundary at $L_B = 2L_N$. Here, the maximum value is of order 50 MHz and we see that the growth rate is smaller when the magnetic field scale length is negative.

3.2 Predictive models

Numerical tools are used extensively to attempt to simulate plasma turbulence. Unfortunately, to date excellent agreement with experiment is somewhat rare. Gyrokinetic, gyrofluid and fluid models are used with particle-in-cell (PIC), or finite difference implementation. Gyrokinetic codes have had some success modeling the core of tokamaks, but the ordering breaks down in the edge. Because future fusion reactors depend on good energy confinement and stable operation, explaining and ultimately mitigating anomalous transport is critical. As such, there has been a significant amount of work attempting to characterize the formation and convection of turbulent eddies in tokamak plasmas, thought to contribute significantly to the under prediction of cross-field transport. [92] For Hall thrusters, fully kinetic PIC codes and PIC-hybrid codes, where generally the electrons are modeled as a fluid, while the ions and neutrals are discretized and treated kinetically, have had some success. However, much work remains before the requisite predictive capability is realized.

3.2.1 Shear based models

Many different methods have been proposed to describe anomalous cross-field transport. One method, which is fairly widely used, involves implementing a type of Bohm model that includes fluctuations and scales inversely with the magnetic field amplitude. This is in contrast to the classical collision model that suggests a conservative $1/B^2$ dependence. [26] In most axial regions of the Hall thruster the fluctuation-based Bohm model agrees fairly well with experimental data.

However, near the exit plane of a Hall thruster, where the radial magnetic field is strongest, experimental results indicate that cross field electron mobility is almost classical. This is somewhat surprising because most of the plasma parameters have strong gradients near the exit region of the thruster. Generally, we expect fluctuation related transport to get worse in areas which contain strong gradients of density or temperature. One explanation that has been proposed to account for this discrepancy has to do with the azimuthal electron velocity, which has a strong axial gradient

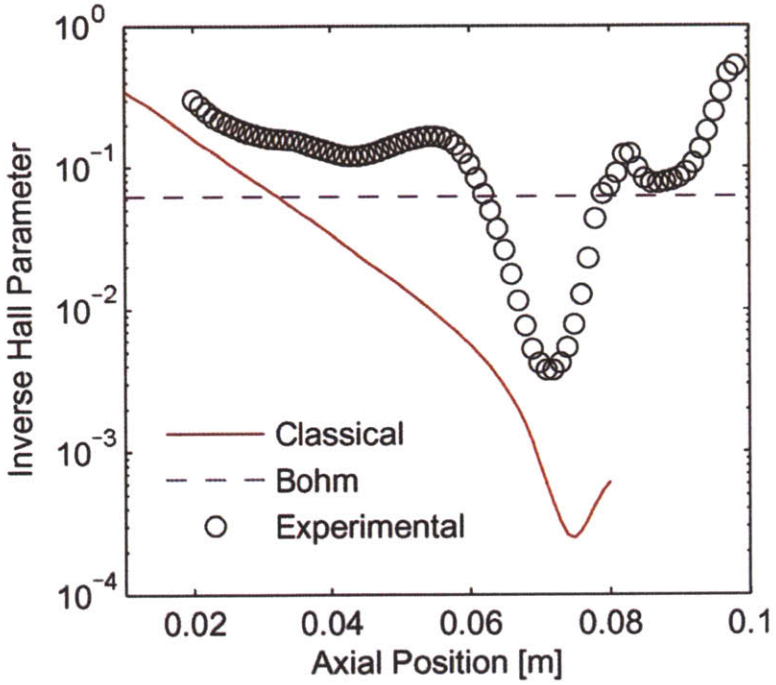

Figure 3-8: Experimental inverse Hall parameter compared with the classical inverse Hall parameter (using experimental collision frequencies) and the Bohm inverse Hall parameter at $V_D = 200$ V. [26]

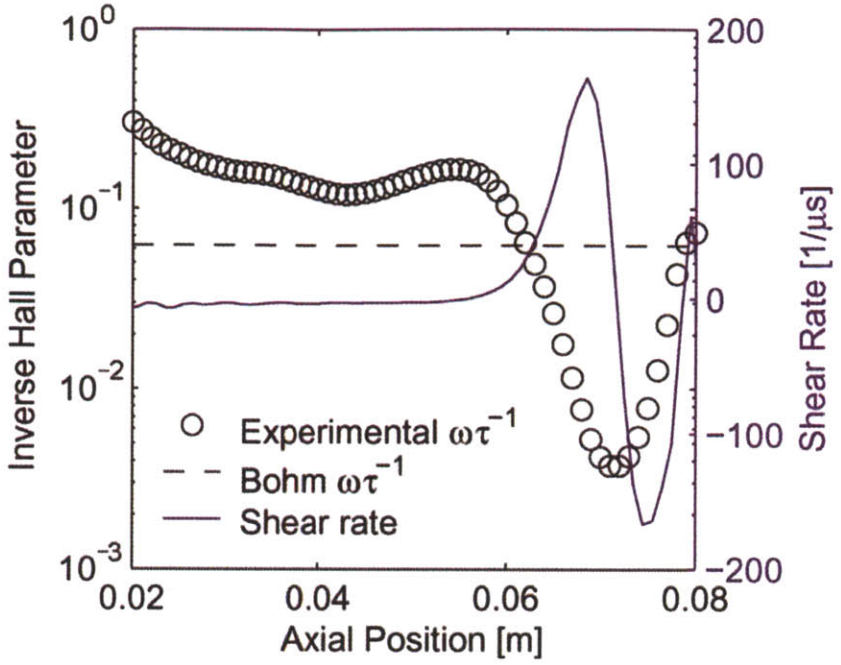

Figure 3-9: Experimental inverse Hall parameter and axial electron shear rate at $V_D = 200$ V. [26]

near the thruster exit. [26] This mechanism has been implicated within the fusion community. Both tokamaks and stellarators show improved confinement in regions where there is strong shear. The idea behind this explanation is essentially that turbulent eddies in the plasma are decorrelated as they are stretched in regions where the plasma flow is sheared. As a result, the anomalous transport is partially suppressed. [26]

As mentioned in the introduction, Hall thruster plasmas and tokamak plasmas are very different animals. In Hall thrusters, the sheared flow is all electrons. However, in tokamaks both the ion and electron flow is sheared. In Hall thrusters the eddy turn over time is slower than the rate at which some fluctuations move through the sheared region. Additionally, the sheared region in Hall thrusters tends to have a zero crossing. However, observations of suppressed transport in regions of strong shear have been made in many different experiments with greatly varying magnetic topologies. [26] So, it is clear that there is some common underlying physics at work.

For Hall thrusters, there are several advantages to be gained if cross field transport could be effectively curtailed through sheared flow. Reduced transport would produce a larger axial accelerating electric field; the ion beam or plume divergence and corresponding channel erosion could be reduced. In addition, the propellant utilization might be enhanced by establishing a robust transport barrier between the ionization region and the thruster exit. [26] Finally, the dissipative circulating current could also be reduced.

Scharfe, et al., implemented a 2D radial-axial hybrid simulation using an empirical model based on tokamak observations and linear analysis to quantify the effect of shear on transport in Hall thrusters. In this model the electrons are treated as a fluid, while the ions and neutrals are treated kinetically. [26] Figure 3-8 shows the experimental inverse Hall parameter compared with the classical inverse Hall parameter (using experimental collision frequencies) and the Bohm inverse Hall parameter at $V_{\mathrm{D}} = 200$ V. Looking at the figure, one can clearly see a region near the exit plane of the thruster where the measured transport becomes similar to the classical value. Figure 3-9 shows that this region of enhanced confinement near the thruster exit overlaps with a region of strong electron axial shear and increased $E \times B$ velocity. [26] This type of transport barrier has been observed in areas of tokamak plasma where there exists a region of strong shear. The tokamak community has studied the phenomenon of transport suppression through enhanced shear extensively in order to mitigate radial heat loss across closed flux surfaces from the hot core to the scrape off layer and walls. In addition to empirical evidence, analytical models also show that when either the amplitude of fluctuations are decreased or when the phase difference between fluctuations is modified, the cross-field transport is reduced.

The idea here is that when the electron fluid (or in a tokamak, the ion and electron fluids) is sheared via electric and magnetic field gradients, turbulent eddies in the plasma get distorted, stretched and decorrelated such that the fluctuation induced anomalous transport is reduced. Scharfe's model [26], which implements a local numerical transport barrier provides relatively good agreement with experimental observations. As Fig. 3-10 reveals, the simulation indicates a wider transport

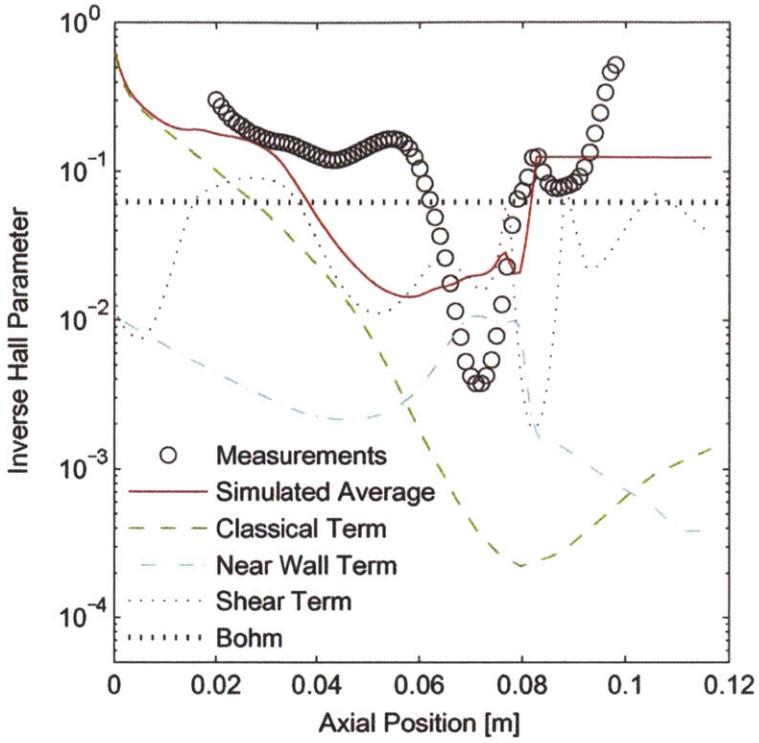

Figure 3-10: The simulated inverse Hall parameter is compared with the Bohm model and with the experimentally measured inverse Hall parameter. The simulated average is composed of the classical, near-wall, and shear terms. [26]

barrier than observed experimentally. However, the shear model generates profiles of plasma parameters that are very similar to simulations, which use experimental electron mobility. In all of the simulated cases run, the shear model performs more accurately at predicting measured plasma properties than a basic Bohm diffusion model, which does not contain an explicit cross-field transport barrier. [26]

In tokamaks there exist two relatively robust methods, which effectively mitigate local anomalous transport. The first involved regions in the plasma where a shear in the $E \times B$ velocity develops. The second involves a region where the magnetic field has negative shear (surrounding a local magnetic X-point). These regions of shear produce transport barriers, which reduce energy and particle transport within the plasma. Both internal transport barriers (ITB) and edge transport barriers have been observed and predicted.

The transition from low confinement (L-mode) to high confinement (H-mode) or

(I-mode) regimes within fusion plasmas is due to such a transport barrier in the edge of the plasma. Fox, et al., sought to exploit the jump in confinement in these devices within the domain of Hall thrusters, using the methodology developed by Waltz [92]. The fusion community discovered a strong correlation between ion temperature gradient turbulence (ITG) and cross-field transport. In cases where there is little shear in the $E \times B$ velocity, there is correspondingly little change in the anomalous diffusion rate. The turbulent eddy structures are well correlated and a cascade of energy down through smaller scales is possible. It was found that once the shear in the plasma reaches a critical threshold, the observed diffusion becomes purely collisional in the classically predicted sense. [92] The turbulent eddies become decorrelated and effectively "quench" the transport. This suggests the implementation of a quench, shear-based model to improve prediction of anomalous transport relative to some simple models. They implemented a linear progressive quench rule to correlate the transport to the $E \times B$ shear rate in the plasma, given by:

$$\gamma_{E\times B} = \frac{d}{dx}\frac{E_{\mathrm{x}}}{B_{\mathrm{r}}}. \tag{3.11}$$

However, the model does have several discrepancies relative to experimental data.

Observations and predictions of Hall thruster performance reveal significant fluctuation induced electron transport . These devices exhibit a plethora of different instabilities across a very large frequency range. At the lower end of the frequency spectrum we find ionization-related instabilities, such as the "breathing" mode and the azimuthal "rotating spoke" instability. In the middle range, we see important turbulence-related axial transit-time oscillations. In the higher frequency range we find high frequency azimuthal drifts, two-stream and Lower hybrid instabilities.

Significant experimental and numerical efforts have shed some light on the confusing nature of anomalous transport in tokamaks. Several methods developed within the tokamak community are being implemented in Hall thruster simulations. Although these two regimes of plasma physics are very different in important ways, phenomena like flow and magnetic shear seem to be robust mechanisms to ameliorate

anomalous transport in general.

Chapter 4

Comparisons of Turbulence in Tokamaks and Hall Thrusters

4.1 Two Disparate Plasma Regimes

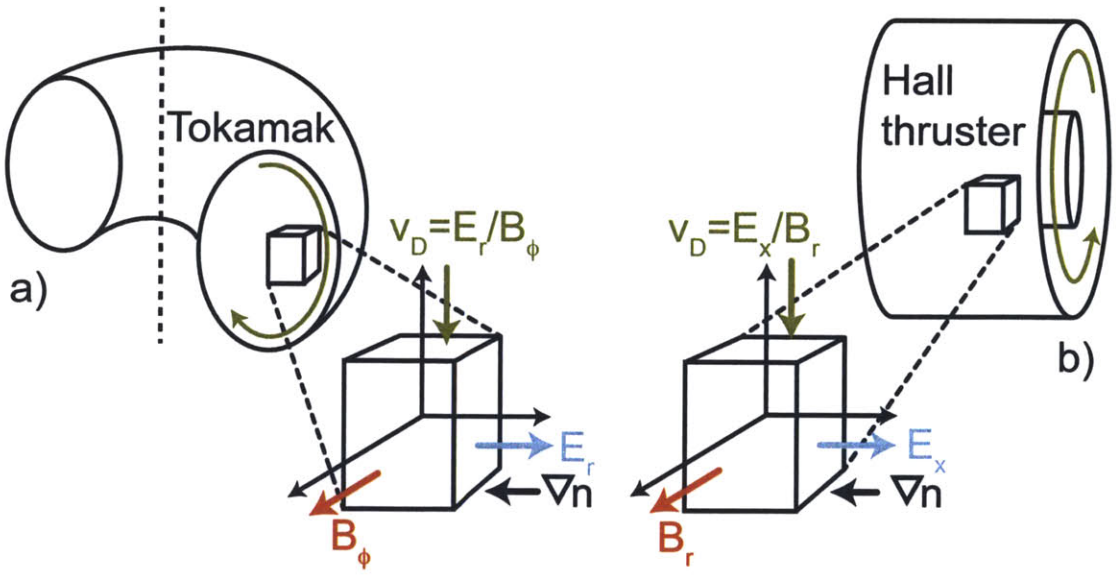

Figure 4-1: Comparison of tokamak a) and Hall thruster b) geometry. Here, a plasma element δV, is shown with the local coordinate system for each topology. Orientation is chosen such that E, B, V_{D} are aligned. This illustrates two of the primary $E \times B$ drifts on each device. On the tokamak $E_{\mathrm{r}} \times B_\phi$ is in the poloidal direction (shown); on the Hall thruster $E_{\mathrm{x}} \times B_{\mathrm{r}}$ is in the azimuthal direction (shown)

Before a comparison is made between fluctuation induced cross-field transport in tokamaks and Hall thrusters, it is important to characterize the basic geometry and plasma parameter space of the two regimes. In Fig. 4-1, a comparison of tokamak a) and Hall thruster b) geometry is shown for reference. Here, a cubic plasma element δV, is illustrated with the local coordinate system for each topology. The orientation is chosen such that E, B, V_{D} are aligned. This illustrates two of the primary $E \times B$ drifts on each device. On the tokamak $E_{\mathrm{r}} \times B_{\phi}$ is in the poloidal direction; on the Hall thruster $E_{\mathrm{x}} \times B_{\mathrm{r}}$ is in the azimuthal direction.

Tokamaks and Hall thrusters occupy very different physical regimes. The size scale of tokamaks is of order meters, while most Hall thrusters have a radius of several centimeters. Magnetic fields used in tokamaks are generally as large as possible, not only because magnetic confinement of electrons and ions is required, but because fusion power in a tokamak scales like $\sim B^4$. However, magnetic fields employed in Hall thrusters are necessarily small to prevent magnetic confinement of the ions used for thrust. Typical parameters for tokamaks and Hall thrusters are given in table 4.1. In addition to the size and magnetic field of these devices, there are numerous physical quantities that are very different.

The density and temperature in the tokamak core are orders of magnitude higher than those found in Hall thrusters ($n_{\mathrm{e}} \sim 10^{20}$ vs 10^{17} [m^{-3}], and $T_{\mathrm{e}} \sim 1000$ vs 20 [eV]). Characteristic frequencies associated with cyclotron motion and plasma oscillations are significantly higher in tokamaks than in Hall thrusters, due to higher magnetic field and density. However, collision frequencies are more comparable; this is because, although collisionality increases with density, collisionality decreases with increasing temperature. The electron–electron collision frequency, ν_{ee} and the electron–ion collision frequency, ν_{ei} are similar for both regimes. However, the total electron collision frequency, ν_{e} is more than an order of magnitude higher in a typical Hall thruster due to the added electron–neutral collisions from, ν_{en}. Characteristic velocities are larger in a typical tokamak compared with a typical Hall thruster; however the size scales are quite different in the two regimes and drift and wave phase velocities can be very similar. In addition, the edge/SOL region in a tokamak has very similar density and

temperature characteristics to those found in Hall thrusters ($n_e \sim 10^{17}$ and $T_e \sim 20$ [eV]). The Debye length is also similar in both regimes, owing to scaling with the square root ratio of temperature to density.

Table 4.1: Tokamak and Hall thruster parameters

	Tokamak	Hall thruster
Magnetic field, B [T]	5	0.02
Device scale length, L [m]	1	0.05
Electron density, CORE, n_e [m^{-3}]	10^{20}	10^{17}
Electron density, EDGE, n_e [m^{-3}]	10^{17}	10^{17}
Ion density, n_i [m^{-3}]	10^{20}	10^{17}
Neutral density, n_n [m^{-3}]	~ 0	10^{19}
Electron temperature, CORE, T_e [eV]	1000	20
Electron temperature, EDGE, T_e [eV]	20	20
Electron cyclotron frequency, Ω_e [Hz]	1.5×10^{11}	5×10^8
Ion cyclotron frequency, Ω_i [Hz]	4×10^7	2×10^3
Electron plasma frequency, ω_e [Hz]	9×10^{11}	5×10^9
Ion plasma frequency, ω_i [Hz]	1.5×10^9	1×10^7
Debye length, λ_D [μm]	25	45
Electron thermal velocity, $v_{th,e}$ [km/s]	2×10^4	2×10^3
Ion thermal velocity, $v_{th,i}$ [km/s]	3×10^2	2
Ion acoustic velocity, $v_{s,i}$ [km/s]	4×10^5	2.5
Alfven speed, v_A [km/s]	3×10^4	30
Electron Larmor radius, ρ_e [m]	2×10^{-5}	7×10^{-4}
Ion Larmor radius, ρ_i [m]	1×10^{-3}	1.5×10^{-1}
Electron confinement time, τ_{ee} [s]	5×10^{-6}	3.8×10^{-6}
Ion confinement time, τ_{ii} [s]	5×10^{-4}	3×10^{-4}
Electron - electron collision frequency, ν_{ee} [Hz]	1.3×10^5	2.5×10^5
Ion - ion collision frequency, ν_{ii} [Hz]	1.8×10^3	3×10^3
Electron - ion collision frequency, ν_{ei} [Hz]	1×10^5	2×10^5
Ion - electron collision frequency, ν_{ie} [Hz]	40	1
Electron - neutral collision frequency, ν_{en} [Hz]	~ 0	2×10^6
Electron total collision frequency, ν_e [Hz]	2×10^5	3×10^6
Lower Hybrid frequency, f_{LH} [Hz]	4×10^9	4×10^6
Hall parameter, β_{Hall}	4×10^6	800
Electron mean free path, $\lambda_{mfp,e}$ [m]	130	8
Density gradient scale length, $L_{\nabla n}$ [m]	0.1	0.02
Temperature gradient scale length, $L_{\nabla T}$ [m]	0.1	0.05
Magnetic field gradient scale length, $L_{\nabla B}$ [m]	0.01	0.01

4.1.1 High Field, High Density, Large Scale

In chapters two and three, detailed experimental data along with simulation results were used to quantify the nature of fluctuation induced cross-field transport in tokamaks and Hall thrusters. Numerous phenomena were described for each regime of plasma experiment. For magnetic confinement tokamak fusion devices, observations suggest drift wave microturbulence as the dominant transport mechanism. Drift waves in tokamaks drive fluctuations that manifest as microturbulence in the plasma and lead to anomalously high cross-field transport. [42, 43, 44] Empirical scaling laws, described in chapter two have been developed to try to quantify the anomalously short confinement time.

Tokamak plasmas confinement modes can bifurcate into low and high confinement regimes, which correlate to sheared flows within the pedestal and edge region of the plasma. These sheared flows are coupled to drift wave turbulence and gradients in density, temperature and potential. Although the higher confinement regimes, such as H-mode and I-mode improve confinement, the losses of energy, momentum and particles are still higher than theory based only on collisions predicts.

The fluctuations are very broadband and extend over a wide range of frequencies. The numerous fluctuations and instabilities interact nonlinearly to produce very broadband spectra. The relative density fluctuations $\tilde{n}/n$ are largest near the edge of the tokamak, where large density gradients exist. The perpendicular wavenumber of these fluctuations is much larger than the parallel wavenumber, $k_\perp \gg k_\parallel$. In addition, the turbulent fluctuations are generally found to drift in the electron diamagnetic drift (EDD) direction at low densities and to drift in the ion diamagnetic drift (IDD) direction at high densities.

Four prominent tokamak instabilities described in chapter two are: the electron drift mode, the Electron Temperature Gradient (ETG) mode, the Ion Temperature Gradient (ITG) mode, and the Trapped Electron Mode (TEM). As mentioned previously, these instabilities can be separated into modes, which result from either trapped or passing particles in tokamaks.

4.1.2 Low Field, Low Density, Small Scale

Similar to tokamak plasmas, Hall thruster plasma parameters fluctuate across a wide frequency band with very broadband characteristics. Numerous instabilities and modes have been characterized in Hall thrusters. At the low end of the spectrum (kHz), two distinct unstable modes are the "breathing mode" and "rotating spoke", described in the previous chapter. While the breathing mode is linked to relatively simple ionization dynamics involving a predator-prey mechanism, the azimuthally rotating spoke has not been explained satisfactorily. [22] Experiments have shown that up to half of the total current in Hall thrusters flows through the rotating spoke. [24]

Between 50 kHz and 500 kHz transit–time oscillations are observed in most Hall thrusters. These fluctuations are turbulent and broadband in nature. In addition, high frequency azimuthal fluctuations are also ubiquitous in Hall thrusters. As mentioned in chapter three, azimuthal drift waves are thought to drive microturbulence in this regime. These waves can also be coupled to both the lower hybrid instability and the two stream instability.

In Hall thrusters, like tokamaks, regions of sheared flow are found to suppress turbulent transport. [26] In Hall thrusters, the effect of sheared azimuthal electron velocity is so strong that near the exit plane of Hall thrusters, the axial electron transport is reduced. This is significant because this region is also where $B_\mathrm{r}, \nabla n$ and $\nabla \phi$ are high.

4.1.3 Waves and instabilities

Drift waves are found in all magnetized plasmas, and provide a fundamental mechanism for cross-field transport of particles, momentum, and energy. Drift waves are the primary mechanism in tokamaks for driving turbulence by tapping into free energy within gradients within the plasma. [48] [49] Hall thrusters also exhibit drift wave phenomena driving some of the observed cross-field transport of electron as described in chapter three.

For a homogeneous plasma, drift waves are damped by electron flow along the

magnetic field. However, in inhomogeneous plasmas, $E \times B$ convection converts some of the cross-field pressure gradient $\nabla_{p\perp}$, into a parallel pressure gradient $\nabla_{p\|}$, which can grow the instability. [51] Here, local plasma parameter gradients ∇Q provide one free energy source for drift waves. The saturation level, occurs at:

$$\frac{\tilde{Q}}{Q} \sim \frac{1}{\langle k_\perp \rangle L_Q}, \tag{4.1}$$

where $\langle k_\perp \rangle$ is an average perpendicular wavenumber and L_Q is the gradient scale length, given by:

$$L_Q = \frac{1}{\left| \frac{d \ln Q}{dx} \right|}. \tag{4.2}$$

Density gradients, temperature gradients and other inhomogeneous plasma properties can drive drift waves. For small plasma β we can assume purely electrostatic modes:

$$\beta = \frac{2\mu_0 \langle p \rangle}{B^2} \ll 1. \tag{4.3}$$

This low beta limit, typical for Alcator C-Mod plasmas and Hall thruster plasmas, allows magnetic fluctuations to be ignored, yielding electrostatic modes.

Instabilities, fluctuations and waves are found in all partially of fully magnetized plasmas. Turbulence in these plasmas generally manifests through a nonlinear interaction among numerous individual waves. A linear description of the changing momentum of a plasma allows the convective derivative $v \nabla v$, to be ignored. To describe the nonlinear dynamics, this term must be included and provides a mechanism for nonlinear wave interactions to produce a turbulent spectrum of fluctuations.

In tokamaks and Hall thrusters, fluctuation induced cross-field transport driven by $\mathbf{E} \times \mathbf{B}$ drifts can be produced by a quadratic nonlinearity arising via three wave coupling. [52] Examples of broadband fluctuations and waves are given in the next section. For this quadratic nonlinearity to occur, a wave $\mathbf{k}_0$ is driven by two other waves $\mathbf{k}_1$, and $\mathbf{k}_2$, which beat together. Both momentum and energy are conserved, such that $\mathbf{k}_0 + \mathbf{k}_1 + \mathbf{k}_2 = 0$ and $\omega_0 + \omega_1 + \omega_2 = 0$. In typical magnetized plasma turbulence in tokamaks and Hall thrusters a true three way coupling manifests among

all the waves present, resulting in numerous degrees of freedom in the system.

Although, the nonlinear three wave interactions are independently fairly coherent, the large number of three wave interactions produces a very incoherent spectrum. The interactions between numerous fluctuations at a given spatial location become uncorrelated outside the correlation time. [52] This correlation time is shorter than the time to respond to the changing background, but longer than the individual eddy turnover time. Thus, these interactions behave independently of an initial state and slowly saturate. The evolving plasma state is considered saturated when the waves individually fluctuate, but collectively maintain a constant level of free energy. [52]

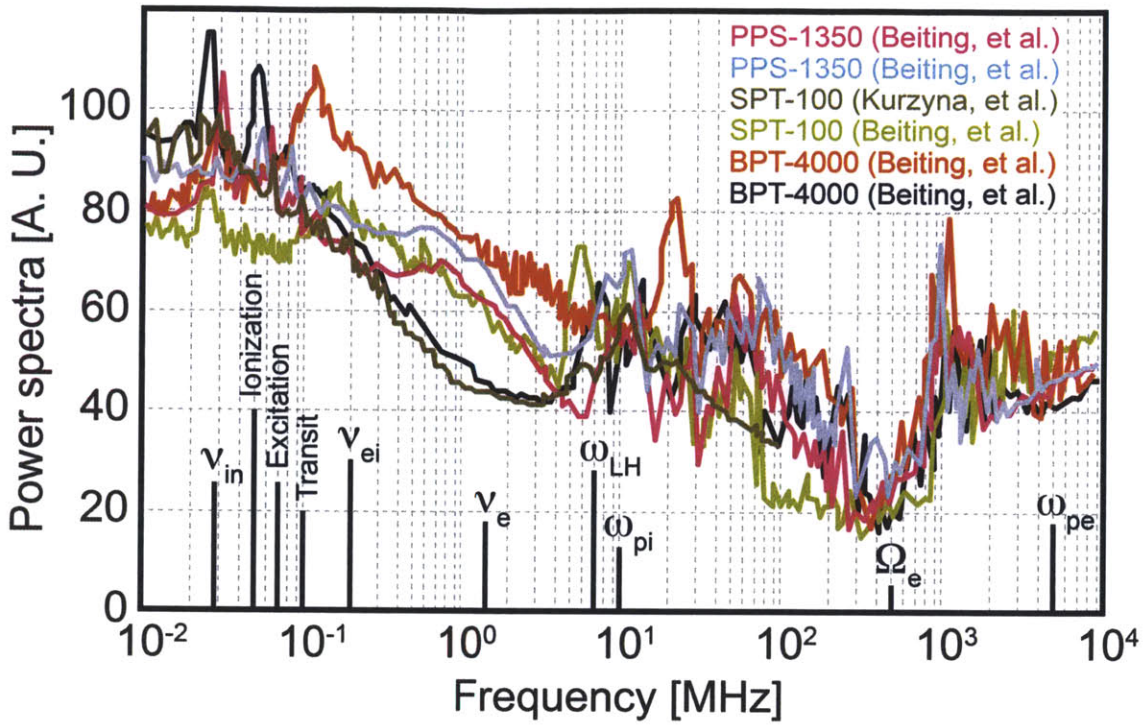

Figure 4-2: Power spectra of fluctuations from 3 different Hall thrusters. The black and red traces are data from a BPT–4000 Hall thruster from Beiting, et al. [27] [28]. The magenta and cyan traces are data from a PPS-1350 Hall thruster from Beiting, et. al. [29] The green traces are data from an SPT-100 Hall thruster from Kurzyna, et al. (dark green) [30] and from Beiting, et al. (light green). [31] Various characteristic frequencies are indicated below the data on the graph.

4.2 Experimental Comparisons

One of the most intuitive ways to analyze fluctuations in plasmas is to compare wave spectra. This can be done simply looking at the power spectrum of a given fluctuating quantity as a function of frequency or wavenumber. Often, the wavenumber spectra are normalized, for instance by the Larmor radius (either ρ_i or ρ_e), to compare different plasmas.

A poignant example of plasma fluctuations is given in Fig. 4-2. Here, power spectra of fluctuations from 3 different Hall thrusters across six decades of frequency (10 kHz to 10 GHz) are shown. The black and red traces are data from a BPT-4000 Hall thruster from Beiting, et al. [27] [28]. The magenta and cyan traces are data from a PPS-1350 Hall thruster from Beiting, et. al. [29] The green traces are data from an

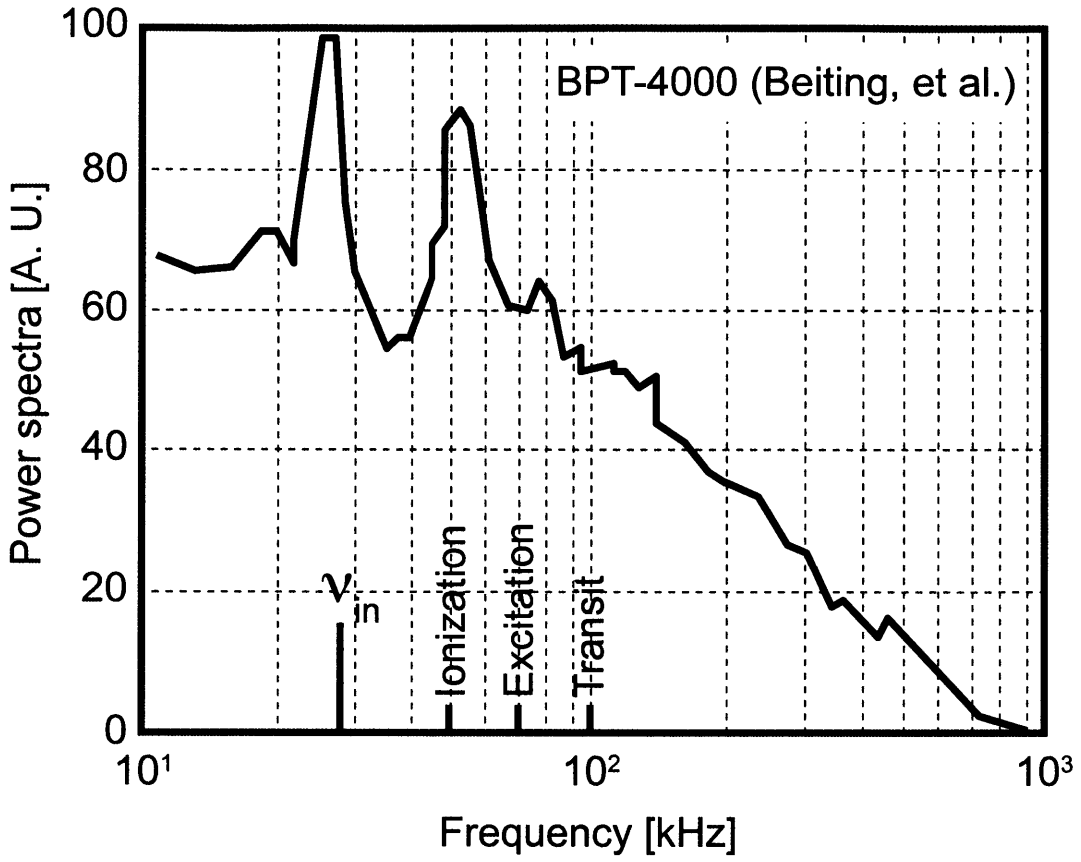

Figure 4-3: Power spectra of fluctuations for the BPT–4000 Hall thruster from Beiting, et al. [28] Two distinct peaks are visible at the frequencies of the ion–neutral collision frequency and ionization frequency. In addition, the excitation and transit–time frequencies are shown along with much smaller perturbations in the spectrum.

SPT–100 Hall thruster from Kurzyna, et al. (dark green) [30] and from Beiting, et al. (light green). [31] Various characteristic frequencies are indicated below the data on the graph. Note, that at the low end of the frequency spectrum, the highest relative power is seen; the peaks here correspond to various ionization processes and related instabilities. In the middle of the plot, centered around 10 MHz, and in the vicinity of the lower hybrid and ion plasma frequencies, another grouping of high relative power peaks is present. Finally, a high frequency group of peaks is present between 1–2 GHz.

To illustrate the correlation of spectral peaks with known plasma physics phenomena, investigation of a single Hall thruster power spectrum is useful. Figure 4-3 shows

power spectra of fluctuations for the BPT–4000 Hall thruster from Beiting, et al. [28] Two distinct peaks are visible at the frequencies of the ion–neutral collision frequency and ionization frequency. In addition, the excitation and transit–time frequencies are shown along with much smaller perturbations in the spectrum.

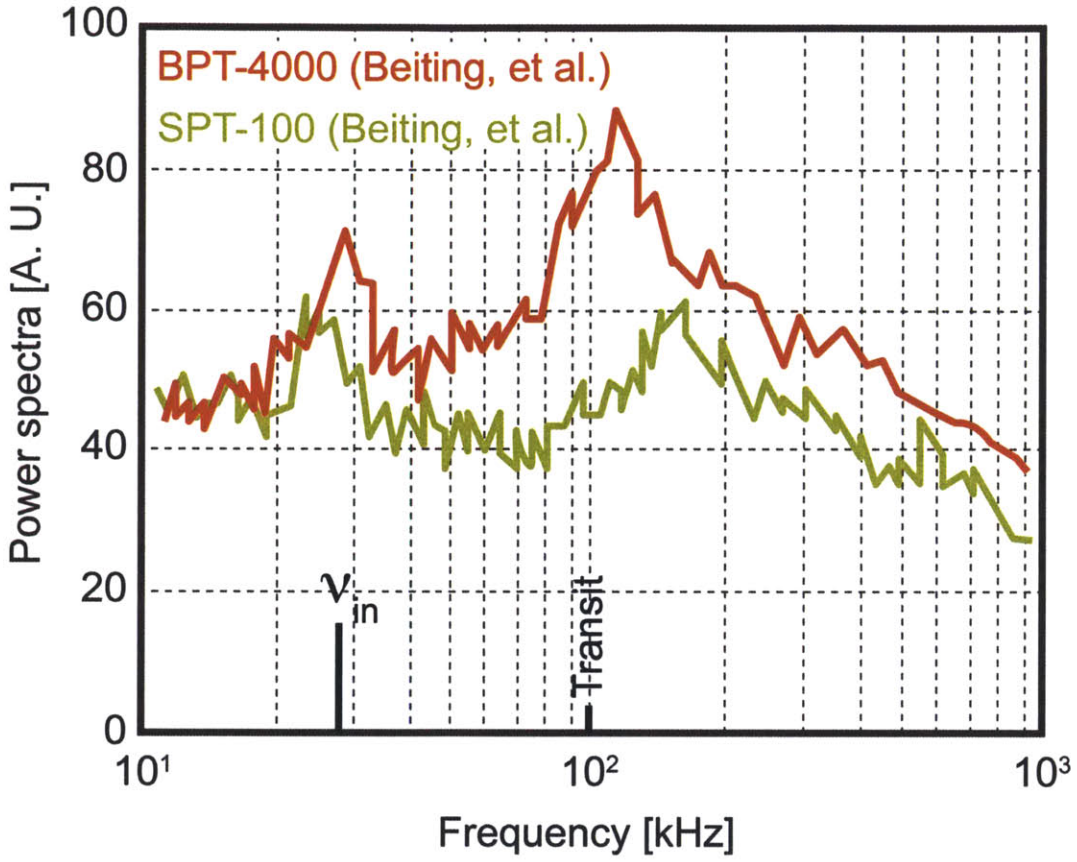

Figure 4-4: Power spectra of fluctuations for the BPT–4000 Hall thruster from Beiting, et al. [27] compared with the fluctuations from an SPT–100 Hall thruster from a separate study by Beiting, et al. [31] Here, two distinct peaks are visible at the frequencies of the ion–neutral collision frequency and near the transit–time frequency.

Another example, shown in Fig. 4-4 is given to illustrate the transit–time oscillations present in many Hall thrusters. Here, power spectra of fluctuations for the BPT–4000 Hall thruster from Beiting, et al. [27] compared with the fluctuations from an SPT–100 Hall thruster from a separate study by Beiting, et al. [31] Here, two distinct peaks are visible at the frequencies of the ion–neutral collision frequency and near the transit–time frequency.

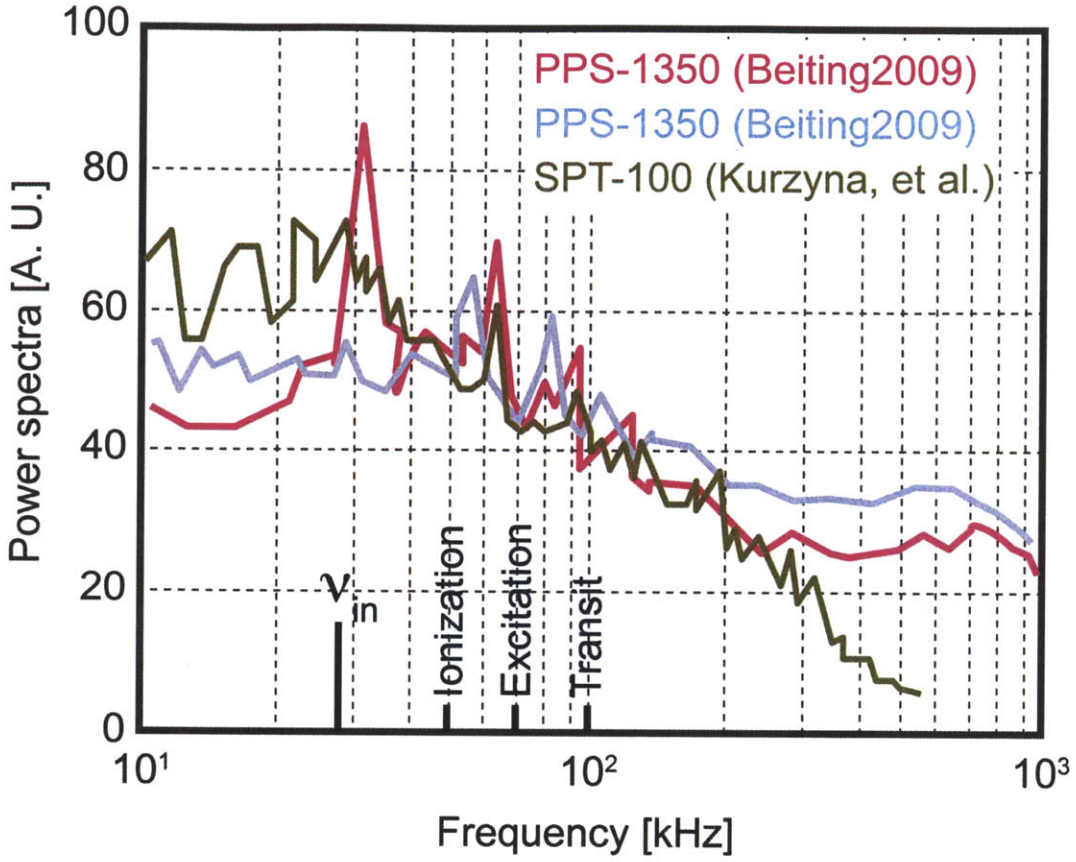

Figure 4-5: Power spectra of fluctuations for the PPS–1350 Hall thruster from Beiting, et al. [29] compared with the fluctuations from an SPT–100 Hall thruster from a separate study by Kurzyna, et al. [30] Again, some distinct peaks are present at frequencies where ionization phenomena occur. In addition, note the shape below $\sim$ 50 MHz, which falls off as roughly $f^{-5/3}$ up to $\sim$ 200 MHz; the SPT–100 continues to follow that trend, while the PPS–1350 traces flatten out as the frequency approaches 1 MHz.

Figure 4-5 shows power spectra of fluctuations for the PPS–1350 Hall thruster from Beiting, et al. [29] compared with the fluctuations from an SPT–100 Hall thruster from a separate study by Beiting, et al. [30] Again, some distinct peaks are present at frequencies where ionization phenomena occur in the Hall thruster data. In addition, note the shape below $\sim$ 50 MHz, which falls off as roughly $f^{-5/3}$ up to $\sim$ 200 MHz; the SPT–100 continues to follow that trend, while the PPS–1350 traces flatten out as the frequency approaches 1 MHz.

Figure 4-6 shows power spectra of fluctuations for the CHS Heliotron from Fuji-

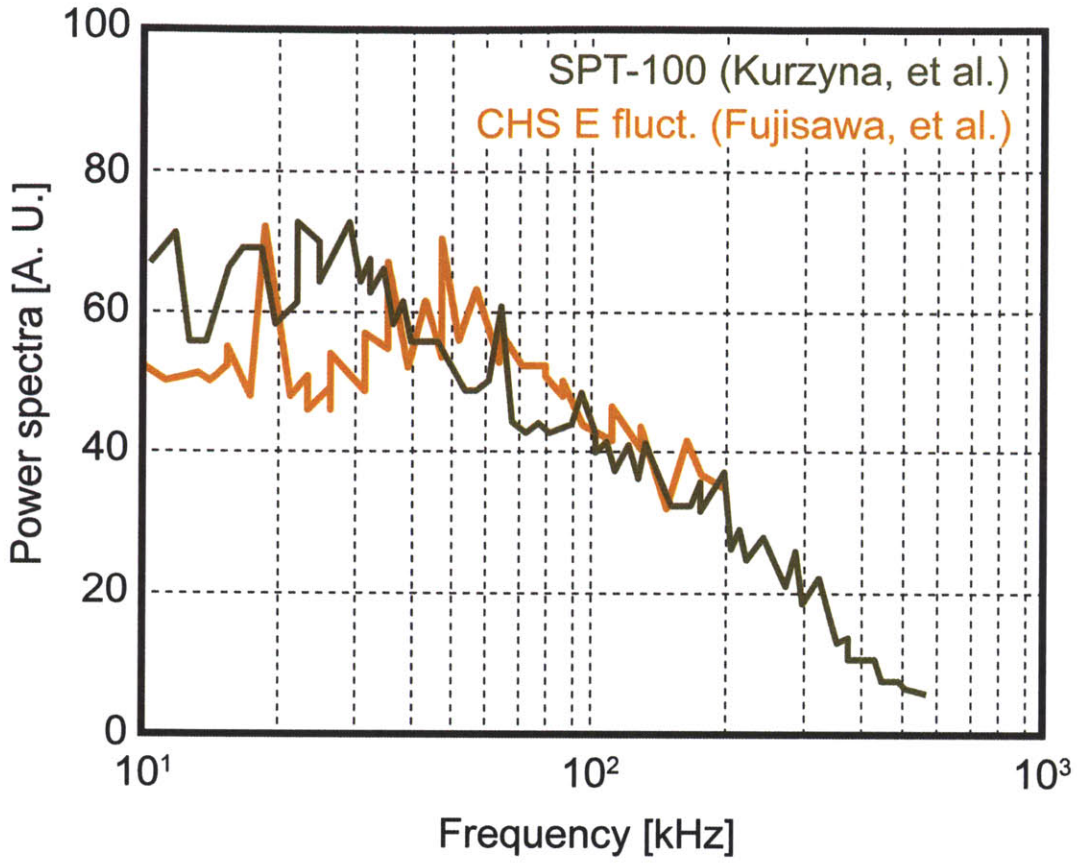

Figure 4-6: Power spectra of fluctuations for the CHS Heliotron from Fujisawa, et al. [5] compared with the fluctuations from an SPT–100 Hall thruster from Kurzyna, et al. [30] Here the comparison is made between a toroidal magnetic confinement heliotron fusion experiment and a Hall thruster. Again, some distinct peaks are present at frequencies where ionization phenomena occur. In addition, note that the shape of both power spectra falls off as roughly $f^{-5/3}$ below $\sim$ 50 MHz.

sawa, et al. [5] compared with the fluctuations from an SPT–100 Hall thruster from Kurzyna, et al. [30] Here the comparison is made between a toroidal magnetic confinement heliotron fusion experiment and a Hall thruster. Again, some distinct peaks are present at frequencies where ionization phenomena occur. In addition, note that the shape of both power spectra falls off as roughly $f^{-5/3}$ below $\sim$ 50 MHz.

Figure 4-7 provides a compelling example of the ubiquitous nature of low frequency plasma turbulence. Here, power spectra of fluctuations for two H-mode plasmas on Alcator C-Mod, Cziegler, et al. [32] (cyan) and Zweben, et al. [16] (purple);

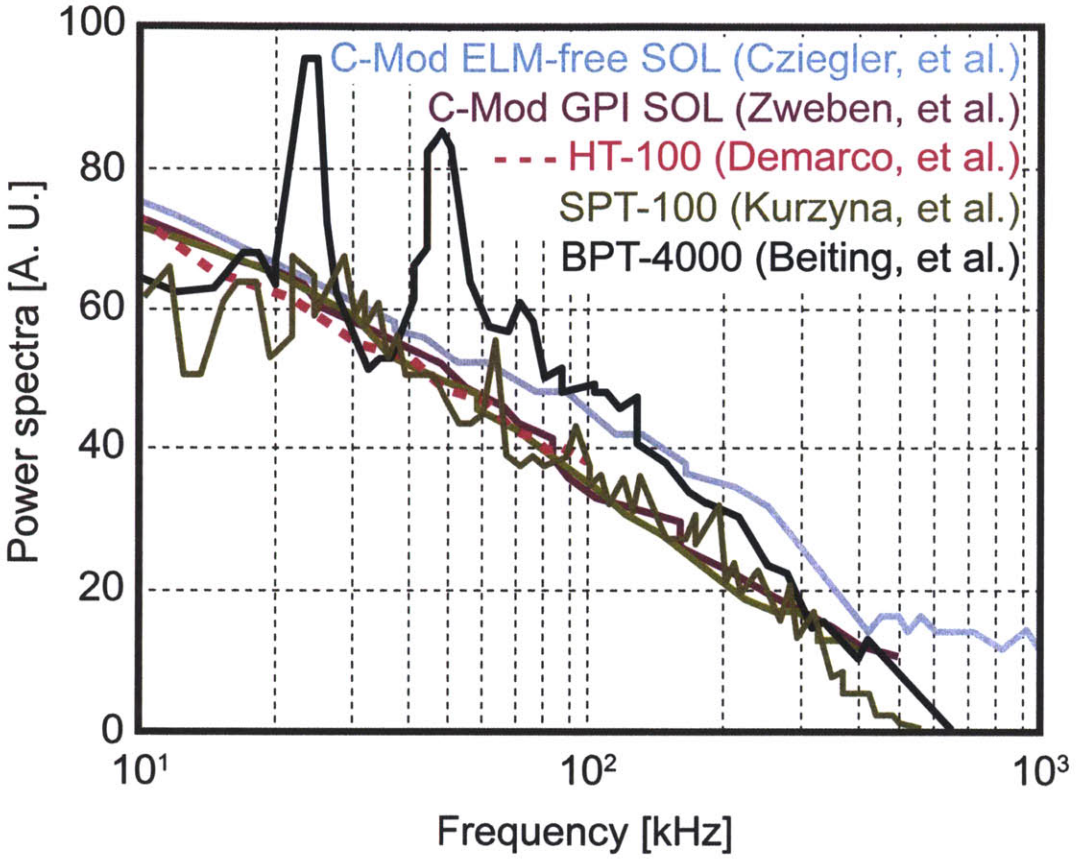

Figure 4-7: Power spectra of fluctuations for two H-mode plasmas on Alcator C-Mod, Cziegler, et al. [32] (cyan) and Zweben, et al. [16] (purple); fluctuations from an HT–100, Demarco, et al. [21] (magenta); fluctuations from an SPT–100, Kurzyna, et al. [30] (green); and fluctuations from a BPT–4000, Beiting, et, al. [28] (black) are plotted. This is an excellent comparison between fluctuations from a tokamak experiment and a Hall thruster. Two distinct peaks are present, as seen previously, from the BPT–4000. However, the rest of the data are extremely similar. Again, note that the shape of both power spectra falls off as roughly $f^{-5/3}$, and that the data are quite broadband in nature.

fluctuations from an HT–100, Demarco, et al. [21] (magenta); fluctuations from an SPT–100, Kurzyna, et al. [30] (green); and fluctuations from a BPT–4000, Beiting, et, al. [28] (black) are plotted. This is an excellent comparison between fluctuations from a tokamak experiment and a Hall thruster. Two distinct peaks are present, as seen previously, from the BPT–4000. However, the rest of the data are extremely similar. Again, note that the shape of both power spectra falls off as roughly $f^{-5/3}$, and that the data are quite broadband in nature.

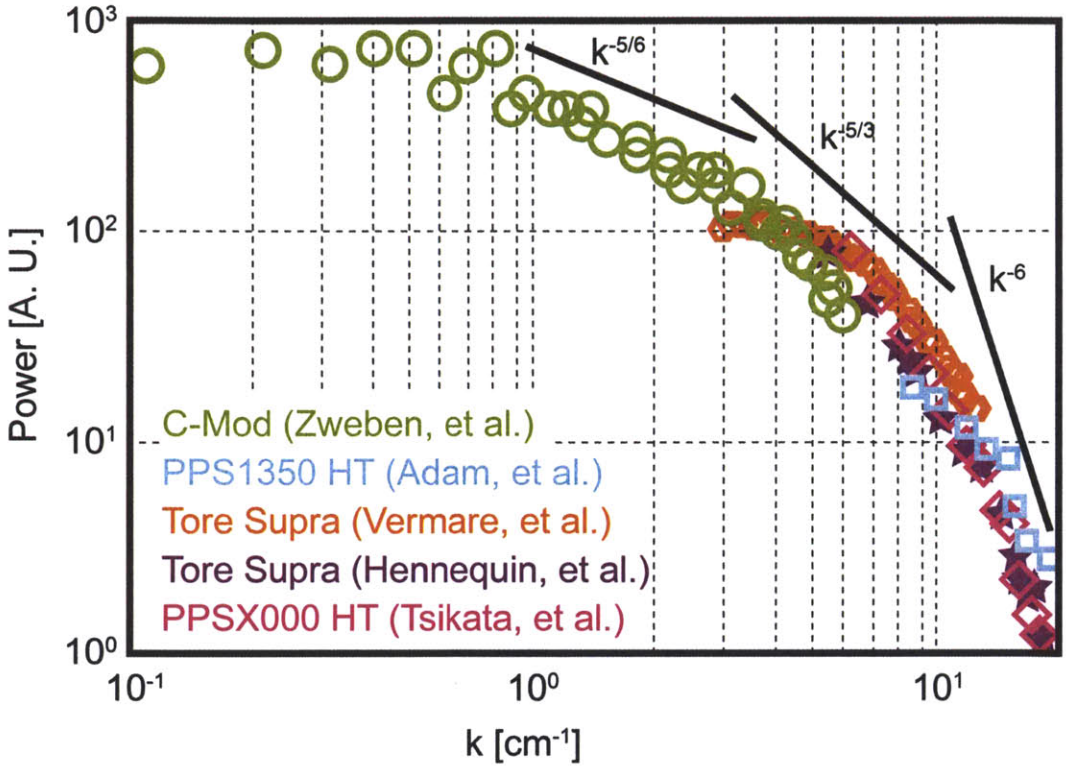

Figure 4-8: Wavenumber spectra of fluctuations from two different tokamaks and two different Hall thrusters. Small wavenumber space is covered by the gas puff imaging (GPI) diagnostic on Alcator C-Mod, from Zweben, et al. [16] (green); data from Tore Supra are shown from Vermare, et al. [12] (orange) and from Hennequin, et al. [9] (navy); data from the PPS–1350 are shown from Adam, et al. [33] (cyan); data from the PPSX000 are shown from Tsikata, et al. [34] (magenta). Remarkably, all of the spectra overlap extremely well above $k \sim 3$ [cm^{-1}]. In addition, the high wavenumber data combined with the GPI data from C-Mod, illustrate the ubiquitous energy cascade found in both plasmas and neutral fluids.

As mentioned previously, the wave number spectrum reveals much about the phys-

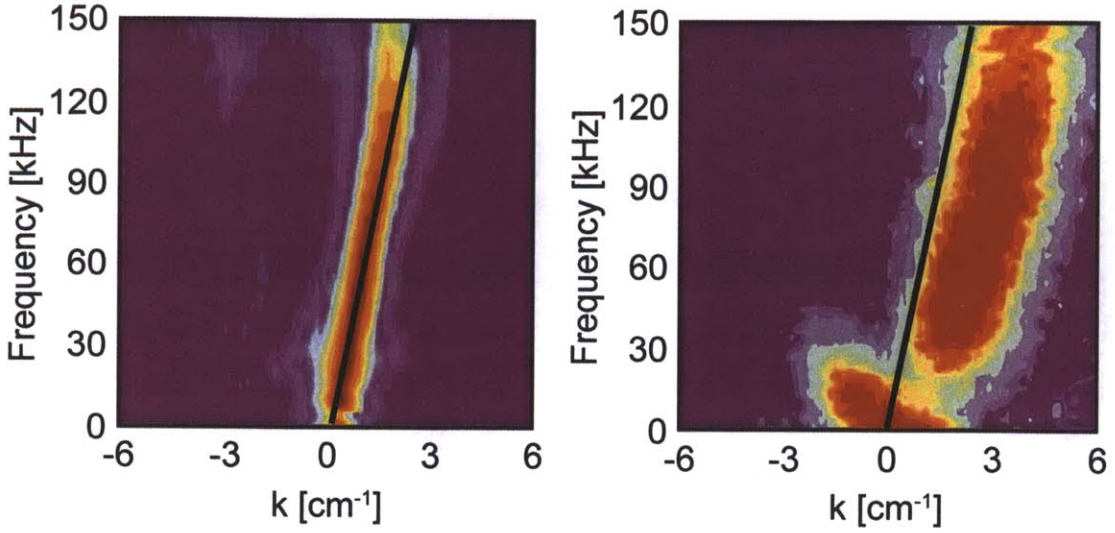

Figure 4-9: Dispersion relations $S(k|f)$ for an SPT–100 plasma from Lazurenko, et al. [35] a), and an Alcator C-Mod L-Mode plasma from Cziegler, et al. [32] b). The tokamak spectra averages a lower frequency for a given wavenumber (black line represents same constant f(k) for both plots). However, also note that both spectra are in the electron diamagnetic drift direction (EDD); trivial for the Hall thruster, but on the tokamak drifts are observed in both directions. This is especially true in the edge, where poloidal velocities can have multiple zero crossings as a function of minor radius.

ical nature of turbulence. Kolmogorov first described a turbulence theory, which manifests as a cascade of energy from some initial "stirring" scale, through an inertial range of turbulence, into a dissipative sink at small scales. [56] The inertial range corresponds to an intermediate set of states where the turbulence has neither a source or sink for energy. This inertial range, along with dissipation scales can be seen in Fig. 4-8. The energy cascade is clearly visible as power decreases with increasing wavenumber. Here, wavenumber spectra of fluctuations from two different tokamaks and two different Hall thrusters are shown. Small wavenumber space is covered by the gas puff imaging (GPI) diagnostic on Alcator C-Mod, from Zweben, et al. [16] (green) and roughly follows a $k^{-5/6}$ scaling; data from Tore Supra are shown from Vermare, et al. [12] (orange) and from Hennequin, et al. [9] (navy); data from the PPS–1350 are shown from Adam, et al. [33] (cyan); data from the PPSX000 are shown from Tsikata, et al. [34] (magenta). Remarkably, all of the spectra, from both

tokamaks and Hall thrusters, overlap extremely well above $k \sim 3$ [cm^{-1}]. In addition, the high wavenumber data combined with the GPI data from C-Mod, illustrate the ubiquitous energy cascade found in both plasmas and neutral fluids. Typically, there is a break in the slope of the cascade at $k_\perp \rho_i \sim 1$. Above we have a power law for $k_\perp \rho_i \gg 1$ and below a different scaling for $k_\perp \rho_i \ll 1$. [8] For small k the data roughly follow a $k^{-5/6}$ scaling, while at large k the data follow a scaling of roughly k^{-6}, as observed by Hennequin, et al. [9]

Figure 4-9 shows a comparison of tokamak and Hall thruster fluctuation dispersion relations. A dispersion relation $S(k|f)$ for an SPT–100 plasma from Lazurenko, et al. [35] is shown in Fig. 4-9a, and an Alcator C-Mod L-Mode plasma from Cziegler, et al. [32] is shown in Fig. 4-9b. The tokamak spectrum averages a lower frequency for a given wavenumber (black line represents same constant f(k) for both plots). Color indicates power, with maximum power shown in red. However, also note that both spectra are in the electron diamagnetic drift direction (EDD); trivial for the Hall thruster, but on the tokamak drifts are observed in both directions. This is especially true in the edge, where poloidal velocities can have multiple zero crossings as a function of minor radius.

4.3 Discussion

In this chapter, multiple power and wavenumber spectra were compared from both tokamak and Hall thruster plasmas. Both edge and core tokamak data were presented, along with data from several different Hall thrusters. In spite of very different plasma parameters, including magnetic topology and strength, density, temperature, spatial scale, collision frequencies, presence of neutrals, Hall parameter, and background electric field, similarities were observed between the fluctuations in both regimes. In some cases, fluctuations at distinct frequencies attributed to specific plasma processes were observed; in Hall thrusters, several instabilities are driven by ionization processes. In other cases, a broadband incoherent spectrum of turbulence was shown. Notably, the correlation in k spectra suggests local gradients dominating the free energy driven

turbulence, supporting a gyro-Bohm transport scaling over pure Bohm mechanism in both Hall thrusters and tokamaks.

Chapter 5

Conclusions and Future Work

5.1 Overview

As we have seen, different types of instabilities, including low-frequency electrostatic drift waves, can cause fluctuations and enhanced transport in tokamaks and Hall thrusters. These drift wave driven fluctuations manifest as microturbulence in the plasma and lead to anomalously high cross-field transport. This microturbulence is universally observed in magnetized plasmas. Traditionally, there has been no simple theoretical model of underlying physics to account for anomalous electron transport.

Observations and predictions of Hall thruster performance reveal significant fluctuation induced electron transport. These devices exhibit a plethora of different instabilities across a very large frequency range. At the lower end of the frequency spectrum we find ionization-related instabilities, such as the "breathing" mode and the azimuthal "rotating spoke" instability. In the middle range, we see important turbulence-related axial transit-time oscillations. In the higher frequency range we find high frequency azimuthal drifts, two-stream and Lower hybrid instabilities.

Significant experimental and numerical efforts have shed some light on the confusing nature of anomalous transport in tokamaks. Several methods developed within the tokamak community are being implemented in Hall thruster simulations. Although these two regimes of plasma physics are very different in important ways, plasma velocity shear and $E \times B$ drifts seem to be robust mechanisms to ameliorate

anomalous transport in general.

As numerical models become more sophisticated, and plasma diagnostics become more sensitive, we move closer to understanding the underlying physics of anomalous cross-field transport. This fluctuation driven transport is ubiquitous in magnetized plasmas, and key aspects of this turbulence are similar in both tokamaks, astrophysical plasmas and Hall thrusters. The spectrum is broadband, exhibits nonlinear wave coupling, and grows numerous unstable modes. In addition, the presence of drift wave structure is observed in both tokamaks and Hall thrusters. Finally, a cascade of energy from driving scales to dissipation scales is also observed in most magnetized plasmas.

5.2 Future Work

Moving forward, it is clear that a path to understanding turbulent fluctuations within Hall thrusters has begun. However, many details of the underlying physics are still missing. Perhaps an enhanced collective effort between techniques and expertise developed within the fusion community and the Hall thruster community can ultimately solve this complex problem of cross-field transport.

One area, which should be addressed, is to better quantify the free energy sources, which drive turbulent fluctuation in tokamaks and Hall thrusters. Separation of the physical mechanisms, which operate on ions and electrons would be a good start. In addition, investigation of different observed tokamak modes (ITG, ETG, TEM, etc.) in different regions (core, edge/SOL, etc.) along with investigation of Hall thruster modes could lead to insight into fundamental physics processes.

Another area worth exploring is the physics mechanism behind sheared zonal flows in tokamak edge plasmas, as it pertains to azimuthal drift shear in Hall thruster electron flows. Tokamak observations support a mutually interacting physics regime between Zonal flows and turbulence. A similar mechanism could exist within Hall thruster plasmas, where microturbulence could feed back into sheared flows near the exit plane region in these devices.

Finally, one very important question that needs to be answered is whether turbulent correlation lengths are determined by local plasma gradients or global system size. The spectra shown in the previous chapter are quite similar, except for the peaks in the Hall thruster data from ionization processes. This similarity, combined with the huge difference in device scales, suggests that gradients can play a stronger role than global system size, indicating a general gyro–Bohm scaling mechanism. However, more studied are needed to verify this hypothesis. To answer these questions, a combination of numerical simulation and experimental data is required.

Bibliography

[1] P. C. Liewer. Measurements of microturbulence in tokamaks and comparisons with theories of turbulence and anomalous transport. *Nuclear Fusion*, 25(5):543, 1985.

[2] J. Wesson. *Tokamaks*. Oxford University Press, 1996.

[3] D. Dickinson, C. M. Roach, S. Saarelma, R. Scannell, A. Kirk, and H. R. Wilson. Microtearing modes at the top of the pedestal. *Plasma Physics and Controlled Fusion*, 55(7):074006, 2013.

[4] H. Doerk, F. Jenko, T. Gorler, D. Told, M. J. Pueschel, and D. R. Hatch. Gyrokinetic prediction of microtearing turbulence in standard tokamaks. *Physics of Plasmas*, 19(5):055907, 2012.

[5] A. Fujisawa. A review of zonal flow experiments. *Nuclear Fusion*, 49(1):013001, 2009.

[6] P. H. Diamond, S.I. Itoh, K. Itoh, and T. S. Hahm. Zonal flows in plasma a review. *Plasma Physics and Controlled Fusion*, 47(5):R35, 2005.

[7] E. Kawamori. Experimental verification of entropy cascade in two-dimensional electrostatic turbulence in magnetized plasma. *Phys. Rev. Lett.*, 110:095001, Feb 2013.

[8] M. Barnes, F. I. Parra, and A. A. Schekochihin. Critically balanced ion temperature gradient turbulence in fusion plasmas. *Phys. Rev. Lett.*, 107:115003, Sep 2011.

[9] P. Hennequin, R. Sabot, C. Honore, G. T. Hoang, X. Garbet, A. Truc, C. Fenzi, and A. Quemeneur. Scaling laws of density fluctuations at high-k on Tore Supra. *Plasma Physics and Controlled Fusion*, 46(12B):B121, 2004.

[10] S. C. Thakur, M. Xu, P. Manz, N. Fedorczak, C. Holland, and G. R. Tynan. Suppression of drift wave turbulence and zonal flow formation by changing axial boundary conditions in a cylindrical magnetized plasma device. *Physics of Plasmas*, 20(1):012304, 2013.

[11] S. Inagaki, T. Tokuzawa, K. Itoh, K. Ida, S.-I. Itoh, N. Tamura, S. Sakakibara, N. Kasuya, A. Fujisawa, S. Kubo, T. Shimozuma, T. Ido, S. Nishimura, H. Arakawa, T. Kobayashi, K. Tanaka, Y. Nagayama, K. Kawahata, S. Sudo, H. Yamada, and A. Komori. Observation of long-distance radial correlation in toroidal plasma turbulence. *Phys. Rev. Lett.*, 107:115001, Sep 2011.

[12] L. Vermare, O. D. Gurcan, P. Hennequin, C. Honore, X. Garbet, J. C. Giacalone, R. Sabot, and F. Clairet. Wavenumber spectrum of micro-turbulence in tokamak plasmas. *Comptes Rendus Physique*, 12(2):115 – 122, 2011.

[13] G. R. Tynan, A. Fujisawa, and G. McKee. A review of experimental drift turbulence studies. *Plasma Physics and Controlled Fusion*, 51(11):113001, 2009.

[14] F. Militello, P. Tamain, W. Fundamenski, A. Kirk, V. Naulin, A. H. Nielsen, and the MAST team. Experimental and numerical characterization of the turbulence in the Scrape-Off Layer of MAST. *Plasma Physics and Controlled Fusion*, 55(2):025005, 2013.

[15] P. Ricci and B. N. Rogers. Plasma turbulence in the Scrape-Off Layer of tokamak devices. *Physics of Plasmas*, 20(1):010702, 2013.

[16] S. J. Zweben, B. D. Scott, J. L. Terry, B. LaBombard, J. W. Hughes, and D. P. Stotler. Comparison of Scrape-Off Layer turbulence in Alcator C-Mod with three dimensional gyrofluid computations. *Physics of Plasmas*, 16(8):082505, 2009.

[17] I. Cziegler, J. L. Terry, S. J. Wukitch, M. L. Garrett, C. Lau, and Y. Lin. Ion-cyclotron range of frequencies in the scrape-off-layer: fine structure radial electric fields. *Plasma Physics and Controlled Fusion*, 54(10):105019, 2012.

[18] N. Bisai, A. Das, S. Deshpande, R. Jha, P. Kaw, A. Sen, and R. Singh. Edge and Scrape-Off Layer tokamak plasma turbulence simulation using two-field fluid model. *Physics of Plasmas*, 12(7):072520, 2005.

[19] M. J. Burin, G. R. Tynan, G. Y. Antar, N. A. Crocker, and C. Holland. On the transition to drift turbulence in a magnetized plasma column. *Physics of Plasmas*, 12(5):052320, 2005.

[20] E. Y. Choueiri. Plasma oscillations in Hall thrusters. *Physics of Plasmas*, 8(4):1411–1426, 2001.

[21] E. A. De Marco and M. Andrenucci. *Turbulence Measurements in a 100 W Hall Thruster.* American Institute of Aeronautics and Astronautics, 2008.

[22] G. S. Janes and R. S. Lowder. Anomalous electron diffusion and ion acceleration in a low-density plasma. *Physics of Fluids*, 9(6):1115–1123, 1966.

[23] M. McDonald, C. Bellant, B. St. Pierre, and A. Gallimore. *Measurement of Cross-Field ElectronCurrent in a Hall Thruster Due to Rotating Spoke Instabilities.* American Institute of Aeronautics and Astronautics, 2011.

[24] C. L. Ellison, Y. Raitses, and N. J. Fisch. Cross-field electron transport induced by a rotating spoke in a cylindrical Hall thruster. *Physics of Plasmas*, 19(1):013503, 2012.

[25] W. Frias, A. I. Smolyakov, I. D. Kaganovich, and Y. Raitses. Long wavelength gradient drift instability in Hall plasma devices. i. fluid theory. *Physics of Plasmas*, 19(7):072112, 2012.

[26] M. K. Scharfe, C. A. Thomas, D. B. Scharfe, N. Gascon, M. A. Cappelli, and E. Fernandez. Shear-based model for electron transport in hybrid Hall thruster simulations. *Plasma Science, IEEE Transactions on*, 36(5):2058–2068, 2008.

[27] E. J. Beiting and J. E. Pollard. Electromagnetic emissions to 60 GHz from a BPT-4000 EDM Hall thruster. In *28th International Electric Propulsion Conference*. ERPS, 2003.

[28] E. J. Beiting, M. L. Garrett, and J. E. Pollard. *Spectral and Temporal Characteristics of Electromagnetic Emissions from the BPT-4000 Hall Thruster*. American Institute of Aeronautics and Astronautics, 2006.

[29] E. J. Beiting, X. L. Eapen, and J. E. Pollard. Electromagnetic emissions from PPS-1350 Hall thruster. In *31st International Electric Propulsion Conference*. ERPS, 2009.

[30] J. Kurzyna, S. Mazouffre, A. Lazurenko, L. Albarede, G. Bonhomme, K. Makowski, M. Dudeck, and Z. Peradzynski. Spectral analysis of Hall-effect thruster plasma oscillations based on the empirical mode decomposition. *Physics of Plasmas*, 12(12):123506, 2005.

[31] E. J. Beiting, M. L. Garrett, and J. E. Pollard. Spectral characteristics of radiated emission from SPT-100 Hall thrusters. In *29th International Electric Propulsion Conference*. ERPS, 2005.

[32] I. Cziegler. *Turbulence and Transport Phenomena in Edge and Scrape-Of-Layer Plasmas*. PhD thesis, MASSACHUSETTS INSTITUTE OF TECHNOLOGY, 2011.

[33] J. C. Adam, J. P. Boeuf, N. Dubuit, M. Dudeck, L. Garrigues, D. Gresillon, A. Heron, G. J. M. Hagelaar, V. Kulaev, N. Lemoine, S. Mazouffre, J. Perez Luna, V. Pisarev, and S. Tsikata. Physics, simulation and diagnostics of Hall effect thrusters. *Plasma Physics and Controlled Fusion*, 50(12):124041, 2008.

[34] S. Tsikata, C. Honore, N. Lemoine, and D. M. Gresillon. Three-dimensional structure of electron density fluctuations in the Hall thruster plasma: E x B mode. *Physics of Plasmas*, 17(11):112110, 2010.

[35] A. Lazurenko, G. Coduti, S. Mazouffre, and G. Bonhomme. Dispersion relation of high-frequency plasma oscillations in Hall thrusters. *Physics of Plasmas*, 15(3):034502, 2008.

[36] J. P. Freidberg. *Plasma Physics and Fusion Energy.* Cambridge University Press, 2007.

[37] V. P. Smirnov. Tokamak foundation in USSR/russia 1950–1990. *Nuclear Fusion*, 50(1):014003, 2010.

[38] I. H. Hutchinson, R. Boivin, F. Bombarda, P. Bonoli, S. Fairfax, C. Fiore, J. Goetz, S. Golovato, R. Granetz, M. Greenwald, S. Horne, A. Hubbard, J. Irby, B. LaBombard, B. Lipschultz, E. Marmar, G. McCracken, M. Porkolab, J. Rice, J. Snipes, Y. Takase, J. Terry, S. Wolfe, C. Christensen, D. Garnier, M. Graf, T. Hsu, T. Luke, M. May, A. Niemczewski, G. Tinios, J. Schachter, and J. Urbahn. First results from Alcator C-Mod. *Physics of Plasmas*, 1(5):1511–1518, 1994.

[39] S. N. Golovato, W. Beck, P. Bonoli, M. Fridberg, M. Porkolab, and Y. Takase. Antennas for ICRF heating in the Alcator C-Mod tokamak. In *Fusion Engineering, 1993., 15th IEEE/NPSS Symposium on*, volume 2, pages 1069 –1072 vol.2, oct 1993.

[40] S. J. Wukitch, B. LaBombard, Y. Lin, B. Lipschultz, E. Marmar, M. L. Reinke, and D. G. Whyte. ICRF specific impurity sources and plasma sheaths in Alcator C-Mod. *Journal of Nuclear Materials*, 390-391:951 – 954, 2009. Proceedings of the 18th International Conference on Plasma-Surface Interactions in Controlled Fusion Device.

[41] D. M. Goebel and I. Katz. *Fundamentals of Electric Propulsion.* Wiley, 2008.

[42] A. J. Wootton, B. A. Carreras, H. Matsumoto, K. McGuire, W. A. Peebles, Ch. P. Ritz, P. W. Terry, and S. J. Zweben. Fluctuations and anomalous transport in tokamaks. *Physics of Fluids B: Plasma Physics*, 2(12):2879–2903, 1990.

[43] J. W. Conner and H. R. Wilson. Survey of theories of anomalous transport. *Plasma Physics and Controlled Fusion*, 36(5):719, 1994.

[44] B.A. Carreras. Progress in anomalous transport research in toroidal magnetic confinement devices. *Plasma Science, IEEE Transactions on*, 25(6):1281–1321, 1997.

[45] E. Mazzucato. Small-scale density fluctuations in the adiabatic toroidal compressor. *Phys. Rev. Lett.*, 36:792–794, Apr 1976.

[46] M. Greenwald, J.L. Terry, S.M. Wolfe, S. Ejima, M.G. Bell, S.M. Kaye, and G.H. Neilson. A new look at density limits in tokamaks. *Nuclear Fusion*, 28(12):2199, 1988.

[47] R. J. Goldston. Physics of the steady-state advanced tokamak. *Physics of Plasmas*, 3(5):1794–1802, 1996.

[48] W. Horton. Drift waves and transport. *Rev. Mod. Phys.*, 71:735–778, Apr 1999.

[49] W. Horton, J. H. Kim, E. Asp, T. Hoang, T. H. Watanabe, and H. Sugama. Drift wave turbulence. *AIP Conference Proceedings*, 1013(1):1–19, 2008.

[50] F. F. Chen. *Introduction to Plasma Physics and Controlled Fusion.* Springer Science, 2006.

[51] R. Dendy. *Plasma Physics: an Introductory Course.* Cambridge University Press, 1993.

[52] B. D. Scott. Introduction to turbulence in magnetised plasmas. *AIP Conference Proceedings*, 1013(1):20–45, 2008.

[53] J. Anderson, H. Nordman, R. Singh, and P. Kaw. Electron geodesic acoustic modes in electron temperature gradient mode turbulence. *Physics of Plasmas*, 19(8):082305, 2012.

[54] J. C. Adam, W. M. Tang, and P. H. Rutherford. Destabilization of the trapped-electron mode by magnetic curvature drift resonances. *Physics of Fluids*, 19(4):561–566, 1976.

[55] A. Fujisawa, K. Itoh, H. Iguchi, K. Matsuoka, S. Okamura, A. Shimizu, T. Minami, Y. Yoshimura, K. Nagaoka, C. Takahashi, M. Kojima, H. Nakano, S. Ohsima, S. Nishimura, M. Isobe, C. Suzuki, T Akiyama, K. Ida, K. Toi, S.-I. Itoh, and P. H. Diamond. Identification of zonal flows in a toroidal plasma. *Phys. Rev. Lett.*, 93:165002, Oct 2004.

[56] A. N. Kolmogorov. Dissipation of energy in locally isotropic turbulence. In *Dokl. Akad. Nauk SSSR*, volume 32, pages 16–18, 1941.

[57] G. G. Howes. Inertial range turbulence in kinetic plasmas. 2007.

[58] S. D. Bale, P. J. Kellogg, F. S. Mozer, T. S. Horbury, and H. Reme. Measurement of the electric fluctuation spectrum of magnetohydrodynamic turbulence. *Phys. Rev. Lett.*, 94:215002, Jun 2005.

[59] R. H. Kraichnan. Inertial ranges in two-dimensional turbulence. *Physics of Fluids*, 10(7):1417–1423, 1967.

[60] D. Fyfe and D. Montgomery. Possible inverse cascade behavior for drift-wave turbulence. *Physics of Fluids*, 22(2):246–248, 1979.

[61] A. Hasegawa and K. Mima. Pseudo-three-dimensional turbulence in magnetized nonuniform plasma. *Physics of Fluids*, 21(1):87–92, 1978.

[62] A. A. Schekochihin, S. C. Cowley, W. Dorland, G. W. Hammett, G. G. Howes, G. G. Plunk, E. Quataert, and T. Tatsuno. Gyrokinetic turbulence: a nonlinear route to dissipation through phase space. *Plasma Physics and Controlled Fusion*, 50(12):124024, 2008.

[63] D. R. Hatch, P. W. Terry, F. Jenko, F. Merz, M. J. Pueschel, W. M. Nevins, and E. Wang. Role of subdominant stable modes in plasma microturbulence. *Physics of Plasmas*, 18(5):055706, 2011.

[64] P. W. Terry, A. F. Almagri, G. Fiksel, C. B. Forest, D. R. Hatch, F. Jenko, M. D. Nornberg, S. C. Prager, K. Rahbarnia, Y. Ren, and J. S. Sarff. Dissipation range turbulent cascades in plasmas. *Physics of Plasmas*, 19(5):055906, 2012.

[65] A. D. Gurchenko and E. Z. Gusakov. Evolution of ETG mode scale turbulence and anomalous electron transport in dynamic tokamak experiments. *Plasma Physics and Controlled Fusion*, 52(12):124035, 2010.

[66] D. R. Ernst, P. T. Bonoli, P. J. Catto, W. Dorland, C. L. Fiore, R. S. Granetz, M. Greenwald, A. E. Hubbard, M. Porkolab, M. H. Redi, J. E. Rice, K. Zhurovich, and Alcator C-Mod Group. Role of trapped electron mode turbulence in internal transport barrier control in the alcator c-mod tokamak. *Physics of Plasmas*, 11(5):2637–2648, 2004.

[67] S. I. Krasheninnikov, D. A. D'Ippolito, and J. R. Myra. Recent theoretical progress in understanding coherent structures in edge and SOL turbulence. *Journal of Plasma Physics*, 74(05):679–717, 2008.

[68] J. A. Boedo. Edge turbulence and SOL transport in tokamaks. *Journal of Nuclear Materials*, 390391(0):29 – 37, 2009. Proceedings of the 18th International Conference on Plasma-Surface Interactions in Controlled Fusion Device.

[69] N. Bisai, R. Singh, and P. K. Kaw. Scrape-Off Layer tokamak plasma turbulence. *Physics of Plasmas*, 19(5):052509, 2012.

[70] B. Nold, T. T. Ribeiro, M. Ramisch, Z. Huang, H. W. Muller, B. D. Scott, U. Stroth, and the ASDEX Upgrade Team. Influence of temperature fluctuations on plasma turbulence investigations with Langmuir probes. *New Journal of Physics*, 14(6):063022, 2012.

[71] S. J. Zweben, D. P. Stotler, J. L. Terry, B. LaBombard, M. Greenwald, M. Muterspaugh, C. S. Pitcher Alcator C-Mod Group, K. Hallatschek, R. J. Maqueda, B. Rogers, J. L. Lowrance, V. J. Mastrocola, and G. F. Renda. Edge turbulence imaging in the Alcator C-Mod tokamak. *Physics of Plasmas*, 9(5):1981–1989, 2002.

[72] S. J. Zweben, R. J. Maqueda, D. P. Stotler, A. Keesee, J. Boedo, C. E. Bush, S. M. Kaye, B. LeBlanc, J. L. Lowrance, V. J. Mastrocola, R. Maingi, N. Nishino, G. Renda, D. W. Swain, J. B. Wilgen, and the NSTX Team. High-speed imaging of edge turbulence in NSTX. *Nuclear Fusion*, 44(1):134, 2004.

[73] S. J. Zweben, J. A. Boedo, O. Grulke, C. Hidalgo, B. LaBombard, R. J. Maqueda, P. Scarin, and J. L. Terry. Edge turbulence measurements in toroidal fusion devices. *Plasma Physics and Controlled Fusion*, 49(7):S1, 2007.

[74] J. L. Terry, S. J. Zweben, K. Hallatschek, B. LaBombard, R. J. Maqueda, B. Bai, C. J. Boswell, M. Greenwald, D. Kopon, W. M. Nevins, C. S. Pitcher, B. N. Rogers, D. P. Stotler, and X. Q. Xu. Observations of the turbulence in the Scrape-Off-Layer of Alcator C-Mod and comparisons with simulation. *Physics of Plasmas*, 10(5):1739–1747, 2003.

[75] S. J. Wukitch, Y. Lin, B. Lipschultz, A. Parisot, M. Reinke, P. T. Bonoli, M. Porkolab, I. H. Hutchinson, and E. Marmar Alcator C-Mod Team. ICRF performance with metallic plasma facing components in Alcator C-Mod. *AIP Conference Proceedings*, 933(1):75–82, 2007.

[76] J. R. Myra, D. A. D'Ippolito, and M. J. Gerver. Faraday screen sheaths and impurity production during ion cyclotron heating. *Nuclear Fusion*, 30(5):845, 1990.

[77] ITER Physics Basis Editors, ITER Physics Expert Group Chairs, Co-Chairs, ITER Joint Central Team, and Physics Integration Unit. Chapter1: Overview and summary. *Nuclear Fusion*, 39(12):2137, 1999.

[78] M. L. Garrett and S. J. Wukitch. Mitigation of radio frequency sheaths through magnetic field-aligned ICRF antenna design. *Fusion Engineering and Design*, 87(9):1570–1575, 2012.

[79] T. Windisch, O. Grulke, and T. Klinger. Radial propagation of structures in drift wave turbulence. *Physics of Plasmas*, 13(12):122303, 2006.

[80] J. S. Chiu and A. K. Sen. Experimental determination of attractor dimension of E x B turbulence. *Physics of Plasmas*, 7(11):4492–4498, 2000.

[81] G. J. M. Hagelaar and N. Oudini. Plasma transport across magnetic field lines in low-temperature plasma sources. *Plasma Physics and Controlled Fusion*, 53(12):124032, 2011.

[82] T. A. Carter. Intermittent turbulence and turbulent structures in a linear magnetized plasma. *Physics of Plasmas*, 13(1):010701, 2006.

[83] G. Y. Antar. On the origin of "intermittency" in the Scrape-Off Layer of linear magnetic confinement devices. *Physics of Plasmas*, 10(9):3629–3634, 2003.

[84] C. Holland, J. H. Yu, A. James, D. Nishijima, M. Shimada, N. Taheri, and G. R. Tynan. Observation of turbulent-driven shear flow in a cylindrical laboratory plasma device. *Phys. Rev. Lett.*, 96:195002, May 2006.

[85] D. Tomilin. Gradient instabilities of electromagnetic waves in Hall thruster plasma. *Physics of Plasmas*, 20(4):042103, 2013.

[86] J. M. Fife, M. Martinez-Sanchez, and J. Szabo. A numerical study of low-frequency discharge oscillations in Hall thrusters. *AIAA paper*, 3052:1997, 1997.

[87] S. Mazouffre. Laser-induced fluorescence diagnostics of the cross-field discharge of Hall thrusters. *Plasma Sources Science and Technology*, 22(1):013001, 2013.

[88] D. Liu, R. E. Huffman, R. D. Branam, and W. A. Hargus. Ultrahigh-speed imaging of Hall thruster discharge oscillations with krypton propellant. *Plasma Science, IEEE Transactions on*, 39(11):2926–2927, 2011.

[89] J. B. Parker, Y. Raitses, and N. J. Fisch. Transition in electron transport in a cylindrical Hall thruster. *Applied Physics Letters*, 97(9):091501, 2010.

[90] Y. Esipchuck and G. Tilinin. *Sov. Phys. Tech. Phys.*, 21(417), 1976.

[91] J. D. Huba and C. S. Wu. Effects of a magnetic field gradient on the lower hydrid drift instability. *Physics of Fluids*, 19(7):988–994, 1976.

[92] J. M. Fox. *Advances in Fully-Kinetic PIC Simulations of a Near- Vacuum Hall Thruster and Other Plasma Systems.* PhD thesis, MASSACHUSETTS INSTITUTE OF TECHNOLOGY, 2007.